IRG1-itaconate axis regulates lung tumorigenesis via pentose phosphate pathway metabolism

Inauguraldissertation
zur Erlangung des Grades eines Doktors der Medizin (Zahnmedizin oder Humanbiologie)
des Fachbereichs Medizin
der Justus-Liebig-Universität Gießen

vorgelegt von Siavash Mansouri
aus Ghaesmshahr, Iran

Gießen (2024)

Aus dem Fachbereich Medizin

Institute for Lung Health (ILH)

Lung Microenvironmental Niche in Cancerogenesis

Justus-Liebig-Universität Gießen

Gutachter: Prof. Dr. Rajkumar Savai

Gutachter: PD. Dr. Pardo-Saganta, Ana

Tag der Disputation: 13.05.2024

Contents

1 Introduction

1.1 Lung cancer

1.1.1 Epidemiology

Despite significant advances in cancer diagnosis and treatment over the last century, cancer remains the second most common cause of death (Siegel, Miller et al. 2019). Of all cancers, lung cancer is currently the second most widespread cancer worldwide. In 2023, the estimated new cases of lung cancer accounted for approximately 12% in men and 13% in women, placing it in the second position, following prostate cancer (29%) in men and breast cancer (31%) in women (Siegel, Miller et al. 2023).

Cancer mortality rates increased throughout most of the 20th century, primarily due to a significant increase in lung cancer deaths in men, which was due to the widespread tobacco epidemic. Lung cancer had the highest proportion of cases attributable to smoking. Around 81% of lung cancer deaths are directly attributable to cigarette smoking, with a further number caused by cigarette smoking directly, with an additional number caused by second-hand smoke (Siegel, Miller et al. 2023). Accordingly, lung cancer has the unfortunate distinction of being the most common cause of cancer-related deaths worldwide, largely due to the fact that a large proportion of lung cancer patients are diagnosed at an advanced stage of the disease (Jemal, Bray et al. 2011, Siegel, Naishadham et al. 2013). Over the last three decades, however, we have seen a significant decline in lung cancer incidence at a steady pace since 2006–2007 by 2.6% annually in men and by 1.1% annually in women (Siegel, Miller et al. 2023). In the same line, the decreased in lung cancer mortality gained momentum, increasing from 3.1% between 2005 and 2014 to 5.3% between 2014 and 2020 in men, and from 1.8% to 4.3% in women. Overall, the lung cancer death rate experienced a significant reduction of 58% in men from 1990 to 2020 and a 36% decrease in women from 2002 to 2020 (Siegel, Miller et al. 2023).These declines in incidence and mortality for lung cancer can be attributed to three main factors: (i) a decline in smoking rates, which were highly epidemic in the 20th century, (ii) promising advances in early detection and (iii) the introduction of new therapeutic approaches (Siegel, Miller et al. 2021).

1.1.2 Classification and pathogenesis of lung cancer

Lung cancer is a highly diverse disease that can develop in various locations within the lung's airway tree, each containing distinct cellular populations (Sarode, Mansouri et al. 2020) (Crystal, Randell et al. 2008). Similar to other epithelial malignancies, most of lung cancer types emerge through a series of pathological changes, involving the

accumulation of genetic abnormalities that transform normal epithelial cells into preneoplastic and eventually neoplastic tissues (Cho and Vogelstein 1992) (Vogelstein and Kinzler 1993). These premalignant changes may differ depending on the specific lung cell types and compartments. In the proximal airways of the lung, the spectrum of neoplastic transformations in basal and secretory mucosal cells is described from hyperplasia, squamous metaplasia and various degrees of dysplasia to in situ carcinomas and invasive squamous cell carcinomas. In the distal airways, diffuse idiopathic pulmonary neuroendocrine cell hyperplasia (DIPNECH) is considered a precursor lesion for neuroendocrine carcinoids of the lung that resembles a tumor. Another recognized premalignant lesion in the lung is atypical adenomatous hyperplasia (AAH), which primarily originates from type 2 pneumocytes and/or Clara cells. AAH precedes the development of non-mucinous bronchiole alveolar carcinoma (BAC).

Lung neoplasms can be divided into two main types based on histological features: small cell lung carcinoma (SCLC) and non-small cell lung carcinoma (NSCLC). Small cell lung carcinoma accounts for 15% of all lung cancer cases and is known as a neuroendocrine tumor. Clinically, it is known for its highly invasive nature, early metastasis and the particularly poor patient prognosis (Travis 2012). NSCLC, on the other hand, accounts for the remaining 85% of lung cancer cases and can be further subdivided into different types, including lung adenocarcinoma (LUAD), lung squamous cell carcinoma (LUSC) and large cell carcinoma. LUAD is the most common form of NSCLC and arises primarily from type II alveolar pneumocytes located in the periphery of the lung. In contrast, LUSC arises in the bronchial tree, in the central regions of the lung, and originates from various types of squamous epithelial cells lining the epithelial airways. Large cell carcinoma, on the other hand, often arises in the central regions of the lung and bears no resemblance to squamous and glandular maturation (Zappa and Mousa 2016).

The sequential lung neoplastic transformation is usually coincident with cigarette smoke as the main risk factor for majority of lung cancer cases (Brambilla and Gazdar 2009) (Islami, Goding Sauer et al. 2018). Cigarette smoke contains various carcinogen compounds which can lead to DNA adduct formation as carcinogen metabolites with potential covalent binding to DNA (Geacintov, Cosman et al. 1997). If DNA repair machinery cannot detect and repair the DNA adduct residues, they may interfere with DNA transcription and replication which consequently lead to genetic mutations (Hwa Yun, Guo et al. 2020). Indeed, cigarette smoke can induce genetic mutations in oncogene kirsten rat sarcoma *(KRAS)* resulting in constitutively activation of KRAS. Active KRAS facilitates the signal transduction of growth factors and governs cell proliferation (Kawano, Takeshima et al. 1996) (Ferrer, Zugazagoitia et al. 2018). *KRAS*-

mutant lung cancer patients have generally been associated with poorer overall survival (Mascaux, Iannino et al. 2005). Furthermore, cigarette smoke can induce mutations in tumor suppressor p53 (*TP53)* leading to a reduction in functional TP53 as a key responsible for DNA damage repair, cell cycle arrest or induction of apoptosis. (Denissenko, Pao et al. 1996, Skoulidis and Heymach 2019). Therefore, the accumulation of genetic and epigenetic mutations followed by cigarette smoke can be considered as the main reason why approximately 85% of NSCLC cases and 98% of SCLC cases are attributed to the effects of cigarette smoke (Brambilla and Gazdar 2009). However, around 25% of all lung cancer cases are not associated to cigarette smoke (Sun, Schiller et al. 2007) and can occur in individuals (mostly women) who have never smoked (LoPiccolo, Gusev et al. 2024). In the same line, less than 20% of smoker only develop lung cancer (Hecht 1999). These evidences suggest other risk factors including environmental conditions, hormonal differences especially between men and women, viral factors and most importantly genetic background also are related to lung cancer risk (Sun, Schiller et al. 2007). In this regard and compared with *KRAS*, epidermal growth factor receptor (*EGFR*) is the most frequent mutated oncogenes in non-smokers patients with lung cancer (Zhang, Yuan et al. 2016) (LoPiccolo, Gusev et al. 2024). EGFR is the part of receptor tyrosine kinases (RTKs) family that regulate cell signaling via extracellular growth factors and have significant roles in the epithelial tissues maintenance and growth (Liu, Wang et al. 2017). Another genetic deregulation in non-smoker lung cancer patients is a gene fusion event involving echinoderm microtubule-associated protein-like 4 (EML4) and the gene which leads to the activation of a potent ALK fusion protein as a significant player in the development of lung cancer (Inamura, Takeuchi et al. 2008).

1.2 Lung cancer treatment

Uncontrolled growth is the main criterion for identifying a tissue mass as a tumor, including lung tumors. Therefore, removal of the tumor mass and/or interruption of its growth rate are the main goals of lung cancer therapy. The choice of the best strategy for lung cancer patients depends on the stage of the cancer and takes into account factors such as the patient's general health and lung function. Traditional treatments include surgery, radiation therapy and chemotherapy, which aim to remove the tumor mass and target the cancer cells as the main component of tumors with strong proliferative features (Thirusangu and Vigneshwaran 2020). However, newer approaches include targeted therapies based on the genetic mutational landscape of cancer cells and immunotherapies based on the immune response of lung tumor components. Increasingly, some of these modalities are being used together in the

treatment of lung cancer. However, in the following chapter, each treatment option is discussed individually.

1.2.1 Surgery

Although surgical resection is one of the oldest cancer treatment methods, it is considered the primary and most reliable treatment option for localized early-stage lung tumors, provided that the cancer can be completely resected and the patient can tolerate the surgical procedure with long-term survival (Lemjabbar-Alaoui, Hassan et al. 2015). In lung tumor surgery, the removal of the lung tumor is usually accompanied by resection of the adjacent lymph nodes and healthy lung tissue. Patients may undergo other treatment options after lung cancer surgery to reduce the likelihood of tumor recurrence, which is common due to the presence of hidden nodal metastases (Lemjabbar-Alaoui, Hassan et al. 2015).

1.2.2 Radiotherapy

In radiotherapy, radiation with low and high linear energy transfer is used to cause cell death, particularly in proliferative cells, directly through ionization-induced DNA damage or indirectly through the production of free radicals (Kirthi Koushik, Harish et al. 2013). For medically inoperable patients, radiotherapy is often one of the recommended treatments for all lung cancer stages and patient performance categories. Conventional radiotherapy usually uses two-dimensional beams and treatment planning is based on diagnostic X-ray images. Stereotactic body radiotherapy (SBRT) is a newly developed technique that offers high-dose irradiation of the tumor while sparing healthy tissue. SBRT uses image guidance and precise radiation delivery for effective treatment of lung (Parashar, Arora et al. 2013).

1.2.3 Chemotherapy

Chemotherapies are primarily aimed at attacking and eliminating rapidly dividing cancer cells. Unfortunately, they are unable to distinguish normal cells from cancer cells, which can also lead to cell toxicity in normal, proliferating cells such as bone marrow. Disruption of the cell cycle is reported to be the main mechanism of the cytotoxic effect of chemotherapeutic agents. They induce cell death by apoptosis by acting directly on DNA or proteins important for cell division. Chemotherapeutic agents can be divided into different classes, including anti-metabolites, antibiotics and toxoids, which act optimally in certain cell cycle phases, while alkylating agents are relatively phase-specific (Amjad, Chidharla et al. 2023). Regardless of the tumor stage, chemotherapy is the preferred treatment option for lung cancer patients who are not candidates for lung surgery due to respiratory or general health reasons. Therefore, over 80% of newly diagnosed lung

cancer patients undergo chemotherapy, either as a stand-alone treatment or in combination with radiotherapy. Among all chemotherapeutic agents, alkylating agents, especially platinum-based chemotherapy including cisplatin and carboplatin, are considered the first line of treatment for lung cancer patients with advanced NSCLC (Rossi and Di Maio 2016).

1.2.4 Targeted therapy

Targeted therapy is mainly developed based on the unique genetic abnormalities in cancer cells. Unlike conventional chemotherapies, which can attack both cancer and normal cells, targeted therapy aims to disrupt the genetic mutations that drive the proliferation and growth of cancer cells while minimizing damage to normal cells (Chirieac and Dacic 2010). Given the diverse mutational landscape of a given lung tumor, targeted therapy can be considered one of the first steps in precision medicine. Targeted therapy agents can be classified as small molecule inhibitors or monoclonal receptor antibodies. The breakthrough in targeted therapy is related to the remarkable clinical response to the first generation EGFR tyrosine kinase inhibitor, gefitinib, in lung cancer patients with activating EGFR mutations (Paez, Janne et al. 2004) (Lynch, Bell et al. 2004). Subsequently, targeted inhibition of ALK with crizotinib has been shown to be effective in lung cancer patients with ALK rearrangements. This treatment has resulted in tumor shrinkage or stable disease in the majority of patients, with an overall response rate of 57% (Kwak, Bang et al. 2010). The greater efficacy of targeted therapy compared to platinum-based chemotherapy in lung cancer patients with EGFR mutations and ALK rearrangements led to the approval of various small molecule inhibitors that specifically target mutated oncoproteins, including BRAF (target: dabrafenib, tramatinib), MET (target: capmatinib, tepotinib) and ROS1 (target: crizotinib, lorlatenib) (Skoulidis and Heymach 2019).

1.2.5 Immunotherapy

Although immunotherapy is the most novel therapeutic approach to lung cancer, its concept dates back more than a century, when it was reported that malignant sarcoma could be treated by repeated inoculations with erysipelas skin infections containing *Streptococcus erysipelas* (Coley 1991). It is now clear that cancer cells can evade the anti-tumor immune response. The importance of immune cells in cancer defense is underscored by studies showing that immunodeficient mice are more susceptible to tumors than their wild-type counterparts. In addition, cancer cells from immunodeficient mice exhibit higher immunogenicity (Koebel, Vermi et al. 2007). In addition, there are documented cases in which kidney transplant recipients with immunosuppression who have received organs from donors with undetected (occult) cancer have developed

secondary tumors (MacKie, Reid et al. 2003). These results underline the crucial role of the immune system in protecting against cancer and point to its therapeutic potential.

The importance of immune-based therapies in lung cancer has recently been highlighted by the significant anti-tumor effect of immune checkpoint inhibitors (ICI). Immune checkpoints are receptors expressed by various immune cells that act as gatekeepers of the immune response by dynamically regulating immune homeostasis under physiologic and pathologic conditions (Pardoll 2012). In the tumor context, cancer cells modulate the expression of immune checkpoints on immune cells particularly T cells to evade the anti-tumor immune response (He and Xu 2020). One of the most successful ICI therapies targets the interaction between programmed death ligand 1 (PD-L1, which is present in elevated levels on cancer cells) and programmed cell death protein 1 (PD-1, which is present or elevated on T cells as an immunoinhibitory checkpoint) in lung (Iwai, Hamanishi et al. 2017). Another immune checkpoint receptor is cytotoxic T lymphocyte-associated protein 4 (CTLA-4), which is mainly expressed in activated T cells and regulatory T cells (Tregs) and has an inhibitory function in T cell activation by preventing interleukin (IL)-2 production and T cell proliferation and causing cell cycle arrest (Babamohamadi, Mohammadi et al. 2024).

1.2.6 Challenges and Limitations in Lung Cancer Therapy

In around 20 to 25 % of patients with an initial diagnosis of NSCLC, the tumors can be surgically removed. However, despite curative surgery, in 30 to 55 % of cases the tumor recurs, which can be fatal outcomes (Liang and Wakelee 2013) (Taylor, Nagji et al. 2012). Neoadjuvant chemotherapy is used for patients in stages that require adjuvant chemotherapy. However, the addition of neoadjuvant chemotherapy to surgical treatment results in only a modest difference of 5 to 6 percentage points in recurrence-free 5-year survival and overall survival. In addition, only a fraction of patients achieve a pathologic complete response (Hellmann, Chaft et al. 2014). While PD-1/PD-L1 immunotherapies have shown hopeful results in lung cancer patients, only a select group of patients respond to these therapies, suggesting that there should be unknown features not only in lung cancer cells, but also and especially in the interaction between immune cells and other components within lung tumors that can be exploited to improve current therapies or develop new therapeutic approaches (Robert 2020). Therefore, in the next chapter I will focus on the interaction between lung cancer and other cellular components in tumor tissue.

1.3 Lung tumor microenvironment

In the last two decades, however, it has become clear that a tumor is not just made up of cancer cells. Rather, a tumor represents a complex and heterogeneous environment consisting not only of cancer cells, but also of different cell types, including immune cells, stromal cells, endothelial cells and neurons, all embedded in a unique extracellular matrix with heterogeneous oxygen, pH and nutrient availability, meaning that a tumor is a dynamic environment. Subsequent research has confirmed that these non-cancerous cell types are not passive bystanders in the tumor, but play a critical role in cancer development, progression and metastasis. This finding gave rise to the concept of the tumor microenvironment (TME), which emphasizes the involvement of non-genetically modified cells and their interactions with cancer cells in tumor development and progression (Baghban, Roshangar et al. 2020). This paradigm shift has also been reflected in the new and updated cancer hallmarks by adding two more hallmarks, including immune avoidance of destruction and tumor-promoting inflammation, which are related to the immune components of a given tumor mass (Hanahan and Weinberg 2011). Indeed, TME is a double-edged sword in tumor development, as it can either promote or inhibit tumor progression. The cellular profile and spatio-temporal architecture of the TME determine its function and influence whether it promotes or inhibits tumor growth (Zheng, Turkowski et al. 2017). In addition to cancer cells, lung TME is mainly composed of, myeloid-derived suppressor cells (MDSCs), cancer-associated fibroblast (CAF), T cell population including CD4 and CD8 subpopulation, , dendritic cells (DCs), tumor-associated neutrophils (TANs) and tumor-associated macrophages (TAMs) (Duan, Zhang et al. 2020). In the next part, each lung TME component will be explained.

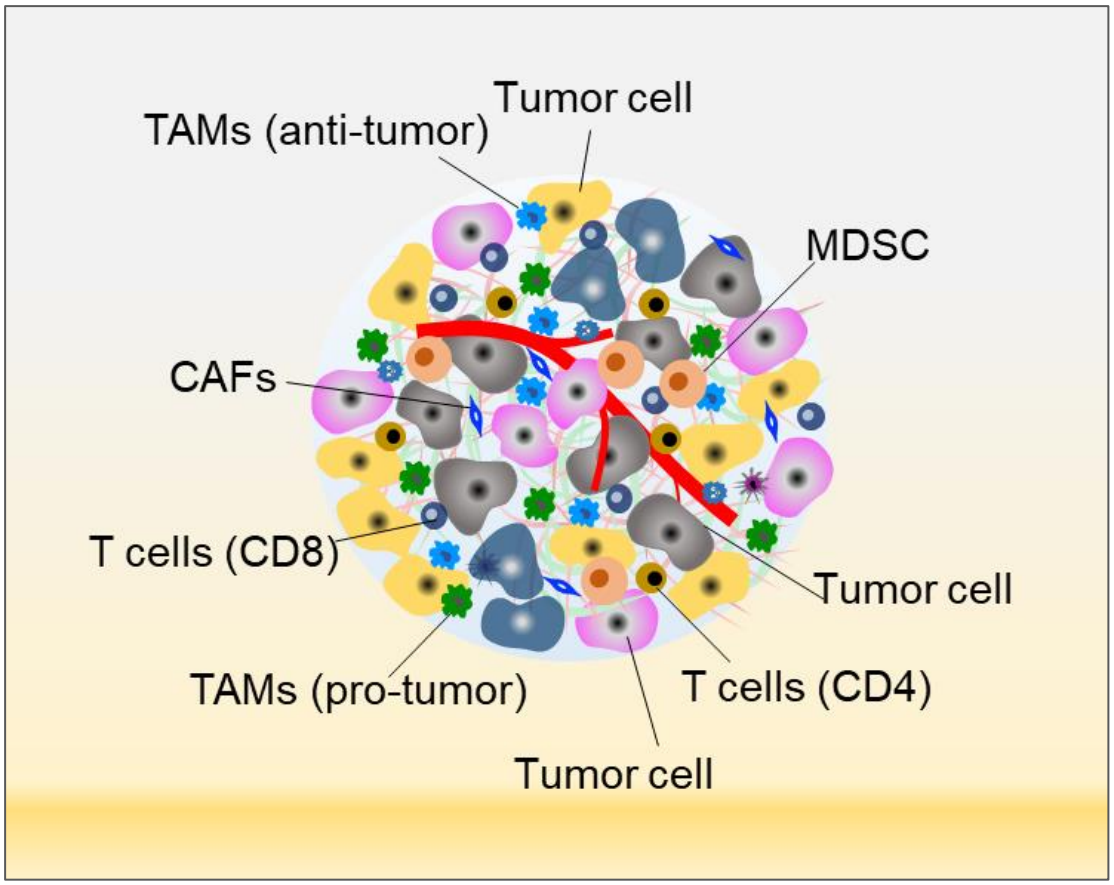

Figure 1-1. The complexity of TME. The TME is a diverse and complex environment that includes different cancer cell types, stromal cells, resident immune cells and recruited immune cells. These different cell types not only interact within their own group, but also interact with other cell types in the TME. In addition, cancer cells surrounded by TME components may be genetically distinct in a tumor, as shown here by different colors. CAFs; cancer-associated fibroblasts. MDSCs; myeloid-derived suppressor cell. TAMs; tumor-associated macrophages.

1.3.1 Cancer-associated fibroblasts

Fibroblasts, typically responsible for synthesizing and resorbing the extracellular matrix (ECM), transform into CAFs during tumorigenesis. CAFs exhibit hyperproliferative behavior, leading to increased ECM synthesis and deposition (Kalluri 2016). Beyond ECM modulation, CAFs also secrete cytokines, chemokines, and metabolites that regulate cancer cell functions, angiogenesis, metastasis, and the immune profile of the TME. For instance, CAFs secrete IL-6, stimulating signaling pathways in cancer cells and promoting invasion and migration (Wang, Cao et al. 2017). They also influence angiogenesis by producing proangiogenic factors, affecting cancer cell migration and metastasis (Fukumura, Xavier et al. 1998). CAFs play a crucial role in shaping the immune status of the TME. They can hinder T cell invasion by upregulating PD-L2 and FAS ligand (FASL) in T cells, inducing antigen-specific T cell death and functional impairment. CAFs recruit TAMs through secretions like stromal-derived growth factor

(SDF)1/ CXC motif chemokine ligand (CXCL)12 and hyaluronan further influencing the immune environment (Lakins, Ghorani et al. 2018) (Gunaydin 2021). Clinically, CAFs are associated with poor prognosis and recurrence in patients with early stage lung adenocarcinoma (Ito, Ishii et al. 2012).

1.3.2 Myeloid-Derived Suppressor Cells

MDSCs are a diverse group of myeloid cells that contribute to an immunosuppressive environment in TME during lung cancer progression (Kumar, Patel et al. 2016). MDSCs can hinder the functions of $CD8^+$ T cells by increasing the production of reactive oxygen species (ROS). They also express higher levels of adhesion molecules, contributing to ROS-mediated immunosuppression (Kusmartsev, Nefedova et al. 2004). Metabolically, tumor MDSCs exhibit increased fatty acid uptake and oxidation, as well as enhanced mitochondrial activity. Blocking fatty acid oxidation can reverse their immunosuppressive effects by reducing cytokine levels necessary for MDSC differentiation (Hossain, Al-Khami et al. 2015). Regarding amino acid metabolism, MDSCs affects T cell function, proliferation, and apoptosis through L-arginine depletion and peroxynitrite production in TME (Rodriguez and Ochoa 2008). Additionally, under hypoxic conditions in the tumor site, MDSCs upregulate PD-L1 via hypoxia-inducible factor 1α (HIF-1α), which can be blocked to reprogram MDSC-mediated T cell suppression and reduce the production of immunosuppressive cytokines including IL-10 and IL-6 (Noman, Desantis et al. 2014).

1.3.3 Tumor-associated neutrophils

Neutrophils, making up around 70% of circulating leukocytes, are the most abundant granulocyte cells in the bloodstream. They play a pivotal role in the immune system's rapid response to tissue damage or infections by swiftly migrating to the affected site. In the context of cancer, neutrophils also have a significant presence in TME, where they perform distinct roles at different stages of tumor development (Uribe-Querol and Rosales 2015). During the initiation of tumors, neutrophils are recruited to susceptible sites through the CXC chemokine receptors (CXCR) 2 and its ligands. Studies in mice lacking CXCR2 have shown reduced tumor formation due to decreased neutrophil infiltration (Jamieson, Clarke et al. 2012). Within the tumor site, TANs can directly promote the transformation of normal cells into cancer cells by producing ROS, reactive nitrogen species (RNS), proteases and prostaglandin E2 (PGE2) (Coffelt, Wellenstein et al. 2016) (Feng, Renshaw et al. 2012). In the early stages of tumor development, TANs produce matrix metalloproteinase 9 (MMP9), a proangiogenic protease by which enhances the tumor progression and metastasis by promoting angiogenesis (Deryugina, Zajac et al. 2014). However, it's worth noting that TANs can also exhibit anti-tumor functions. In the early stages of lung tumors, certain TAN subsets stimulate T cell

proliferation and interferon (IFN)γ production while producing pro-inflammatory cytokines and IL-1 receptor antagonists (Eruslanov, Bhojnagarwala et al. 2014). This suggests that the TME in the early stages of lung tumors recruits a specialized subset of immune cells including TANs with anti-tumor capabilities.

1.3.4 Dendritic Cells

DCs, as expert antigen-presenting cells (APCs), play a central role in shaping the anti-tumor immune response within TME. They achieve this by identifying, capturing, and presenting tumor antigens to T cells and by releasing inflammatory cytokines that can influence other TME components, promoting an anti-tumor environment. Cancer cells may trigger the expression of the co-inhibitory molecule B7-H3 on the surface of DCs, hindering their ability to activate T cells within lung tumors (Schneider, Hoffmann et al. 2011). Additionally, DC-secreted tumor growth factor (TGF)-β can drives the differentiation of $CD4^+$ T cells into immunosuppressive phenotype (Dumitriu, Dunbar et al. 2009). Recognizing the substantial impact of DCs on the TME's immune profile, the intrapulmonary administration of C-C motif chemokine ligand (CCL) 21-gene modified DCs, capable of secreting CCL21 into the lung TME, initiated potent anti-tumor immune responses. This approach recruited resident DCs, T cells, and natural killer (NK) cells to the tumor site, resulting in reduced tumor burden and a favorable shift in the TME's immune profile (Yang, Batra et al. 2006). Clinical trials also showed the patients who received the vaccine displayed an increase in $CD8^+$ T cell infiltration into the tumor, as well as higher levels of tumor PD-L1 expression. These findings suggest that a DC-targeted approach can be effectively combined with PD-1/PD-L1 checkpoint inhibitors, particularly in lung cancer patients who exhibit low PD-L1 expression levels in their tumors and a deficiency in $CD8^+$ T cell populations (Lee, Lee et al. 2017).

1.3.5 T cells

T cells play a crucial role in recognizing cancer-related antigens on tumor cells, initiating anti-tumor immune responses. However, as mentioned earlier, cancer cells can manipulate the lung TME to suppress T cell anti-tumor functions and even promote pro-tumor T cell activities. T cells can be broadly categorized into two groups based on their roles in the TME, anti-tumor T cells including $CD8^+$ cytotoxic T cells and $CD4^+$ T helper 1 (Th1) cells. These cells become activated and produce granzyme B, IFNγ, IL-2 and tumor necrosis factor (TNF)α, which contribute to their anti-tumor functions. Studies show that tumors highly infiltrated with $CD8^+$ and Th1 cells are associated with improved clinical outcomes in various cancer types (Nishimura, Iwakabe et al. 1999). Pro-tumor T cells are derived from the $CD4^+$ lineage, are further divided into Th2 and Tregs cells. Th2 cells indirectly promote angiogenesis and metastasis by activating TAMs in a manner

that supports an immunosuppressive and proangiogenic environment (Shalapour and Karin 2015) (Fridman, Pages et al. 2012). Tregs, on the other hand, induce immunosuppression in the TME through the expression of co-inhibitory molecules like CTLA-4 and lymphocyte-activation protein 3. They also release molecules like PGE2 and TGF-β, further contributing to immunosuppression. In lung cancer, removing Treg cells in mouse models has been found to slow tumor growth and boost the activity of infiltrating $CD8^+$ T cells (Ganesan, Johansson et al. 2013).

1.4 Tumor associated macrophages

1.4.1 Tumor associated macrophages origin

TAMs are among the most abundant immune cells in the TME of various cancers, including lung cancer (Sorin, Rezanejad et al. 2023). TAMs mainly arise from monocytic precursors that originate in the bone marrow. As the cancer progresses, it often triggers signals and factors that attract these monocytic progenitors to the tumor site. After recruitment, these progenitors undergo differentiation and maturation into TAMs and adopt various functional phenotypes that can either promote or inhibit tumor growth and progression (Mantovani, Marchesi et al. 2017). However, in the early stages of lung tumor development, it has recently been shown that tissue-derived macrophages (TRMs) are the major source of TAMs supporting lung tumor growth in mice lacking massive infiltration of monocyte-derived TAMs (Singhal, Stadanlick et al. 2019, Casanova-Acebes, Dalla et al. 2021). The change in phenotype of TAMs during the development, progression and metastasis of lung tumors is not yet well defined and requires further investigation. In addition, there is no comprehensive picture of the origin of TAMs during lung tumorigenesis, whether the origin of TAMs changes in late lung tumor stages or not.

1.4.2 Tumor associated macrophages activation and phenotype

TAMs are plastic cells that exhibit a range of phenotypes and functions that are influenced by various TME signals emanating from cancer cells, T cells, fibroblasts and other macrophages (Mϕ). TAMs can be considered to have a dual nature, with anti-tumor Mϕ having an immunostimulatory and pro-inflammatory character, while their pro-tumor counterparts exhibit anti-inflammatory and angiogenic behavior and suppress the anti-tumor activity of other immune cells (Jayasingam, Citartan et al. 2019, Zheng, Weigert et al. 2020). In lung cancer patients, a dominant presence of anti-tumor TAMs and a limited presence of pro-tumor TAMs often indicate better survival rates (Jackute, Zemaitis et al. 2018). Close proximity of pro-tumor TAMs to lung cancer cells promotes tumor cell survival and leads to unfavorable outcomes in lung cancer patients (Zheng, Weigert et al. 2020). Pro-tumor TAMs have long been considered to be alternatively

activated Mϕ (M2-like) that arise from an adaptive immune response triggered by cytokines from Th 2 cells such as IL-4, IL-5 and IL-13. M2-like Mϕ are characterized by the expression of scavenging and mannose receptors such as CD206, the secretion of growth factors with low expression of IL-12 and high expression of IL-10 (Mantovani, Sozzani et al. 2002). In view of these properties, M2-like Mϕ have the ability to phagocytose and eliminate parasites and are also involved in tissue remodeling, wound healing and tumor progression.

In contrast, anti-tumor TAMs have been recognized as classically activated Mϕ (M1-like) generated by bacterial components such as lipopolysaccharide (LPS) and the Th1 cytokine IFNγ (Xue, Schmidt et al. 2014). These Mϕ exhibit a strongly pro-inflammatory phenotype characterized by a distinct transcriptional profile such as signal transducer and activator of transcription (STAT) 1 and interferon regulatory factor 3 (IRF3). M1-like Mϕ maintain the strong antibacterial phenotype through the production and secretion of Th1 cell–attracting chemokines, CXCL9 and CXCL10, and pro-inflammatory mediators such as TNFα, IL-1β, IL-12 along with the generation of reactive oxygen and nitrogen species (Biswas and Mantovani 2010). Although using the M1-like/M2-like classification for the TAMs population could expand our knowledge of Mϕ, the system has some limitations. First, if we only use LPS/IFNγ for M1-like polarization and IL4/IL13 for M2-like Mϕ polarization, we tend to lose the specificity of the source and context of these stimuli. Consequently, we cannot draw precise conclusions about which cell types or environmental factors are responsible for the polarization of these two Mϕ types under both physiological and pathological conditions. As mentioned above, Mϕ are highly adaptable immune cells that can change their functions and phenotypes in response to environmental stimuli. However, if we use the M1-like/M2-like classification system, we limit this adaptability, as these two extreme phenotypes do not allow bidirectional transitions. The tissue microenvironment is recognized as a dynamic and diverse milieu in which both M1-like and M2-like stimuli can coexist. Consequently, different Mϕ populations can simultaneously inhabit a given tissue.

The complexity and adaptability of the TAMs population recently became clearer through the use of single-cell RNA sequencing (scRNA-seq) and mass cytometry by time-of-flight (CyTOF), which revealed different TAMs cluster types with distinct transcriptomic and proteomic features in human and mouse lung tumors. In human lung tumors, scRNA-seq revealed 14 transcriptional states of cells classified as monocytes and Mϕ (Zilionis, Engblom et al. 2019). Among all clusters, there were three distinct clusters with monocyte gene signatures, nine with Mϕ, one with monocyte and dendritic cell phenotype, and one Mϕ cluster defined by cell cycle gene expression. Application of the

M1-like/M2-like classification to 14 Mϕ states revealed 4 clusters with an M2-like phenotype, while no Mϕ clusters were associated with an M1-like phenotype, suggesting that the M1-like phenotype is present as an anti-tumor Mϕ in the early stage of lung tumor development (Zilionis, Engblom et al. 2019). As expected, some sub-clusters in the Mϕ populations had a specific gene expression profile associated with poor patient survival (Zilionis, Engblom et al. 2019). Overall, the M1-like/M2-like classification system provides a simplified platform for deciphering the functions of TAMs *in vitro* and *ex vivo*. However, this system does not fully reflect the complexity of phenotypes and plasticity of TAMs *in vivo*.

1.4.3 Therapeutic potential of TAMs

Recent studies underline the therapeutic potential of TAMs in lung cancer and show that it is possible to transform pro-tumor TAMs into anti-tumor TAMs via transcriptional and epigenetic modifications through the inhibition of beta-catenin transcription factor and histone deacetylase 2, respectively. The reprogramming of TAMs towards anti-tumor phenotype by those strategies led to a significant reduction of lung tumor growth and metastasis in preclinical models (Georgoudaki, Prokopec et al. 2016, Sarode, Zheng et al. 2020, Xiao, Guo et al. 2020, Zheng, Sarode et al. 2023). In particular, there is evidence that TAMs may interfere with the efficacy of immune checkpoint therapies. Consequently, targeting TAMs could increase the efficacy of ICI-based treatments (Cassetta and Kitamura 2018). Consequently, recognition of the unique properties of both anti-tumor and pro-tumor TAMs may lead to innovative treatments that optimize the anti-tumor response in the TME and decipher the shifts in TAM phenotypes during lung tumor growth and spread.

1.4.4 Metabolic state of TAMs

Cellular metabolism is one of the most important cellular pathways closely linked to the immune functions of TAMs. Several metabolic pathways including glycolysis, tricarboxylic acid (TCA) cycle and fatty acid oxidation (FAO) not only provide sufficient energy supply for Mϕ survival and differentiation, but also produce various biosynthetic intermediates necessary for Mϕ functions, including promotion of angiogenesis and tumor cell invasion, and suppression of antitumor immunity (Geeraerts, Fernandez-Garcia et al. 2021). Although different metabolic pathways lead to the production of unique metabolites, they are closely linked because they require the same fuel, especially glucose as the cell's main energy source, and because the products of one pathway serve as important synthetic precursors for others (Zhang, Wang et al. 2021). For example, fatty acid synthesis can be considered as a convergence point between different metabolic pathways, as its process depends on the availability of intermediates,

especially acetyl-CoA, the common product of the glycolytic pathway and TCA cycle metabolism (Koundouros and Poulogiannis 2020).

Metabolic differences emphasize the distinction between M1-like and M2-like Mϕ. M1-like/anti-tumor Mϕ are highly dependent on glycolysis and exhibit impaired TCA cycles with increased production of ROS and unique metabolite itaconic acid (itaconate). In contrast, M2-like/pro-tumor Mϕ operate with a complete TCA cycle linked to oxidative phosphorylation and fatty acid oxidation (Russell, Huang et al. 2019). These metabolic features not only have cell-autonomous immune functions in Mϕ, but also initiate metabolic interactions that affect cancer cells and other elements of the TME (Zheng, Mansouri et al. 2020). However, it is important to note that TAMs may exhibit dynamic metabolic profiles in response to oxygen and nutrient availability within the tumor TME. Therefore, the binary classification into M1-like and M2-like Mϕ cannot be universally applied to TAMs, as they are able to adapt their metabolic characteristics to the specific conditions within the TME. Indeed, the metabolic profile of TAMs during tumorigenesis and progression remains unclear. Moreover, it is unclear whether the metabolic profile of TAMs is associated with pro- or anti-tumor functions, especially in the context of lung cancer. In the next parts, the most important metabolic pathways in TAMs and Mϕ will be introduced.

1.4.4.1 Amino acid metabolism

The amino acid metabolism of TAMs serves as a collaborator with cancer cells in suppressing the immune response of T cells. The first reference to this concept emerged four decades ago when it was demonstrated that Mϕ can inhibit lymphocyte function by degrading arginine in cell culture media (Kung, Brooks et al. 1977). Mϕ metabolize arginine in two different ways, either by nitric oxide (NO) synthase or by arginase (ARG). NO synthase converts arginine to NO and L-citrulline with pro-inflammatory properties and ARG hydrolyzes arginine to ornithine and urea with anti-inflammatory (Chang, Liao et al. 2001). Interestingly, a high ARG content in TAMs leads to a depletion of extracellular L-arginine, a vital amino acid. As a result, this depletion leads to loss of the ζ-chain of CD3 in antigen-stimulated T cells, which impairs the function of T cells and makes them less effective in their immune response (Rodriguez, Quiceno et al. 2004). In addition, the availability of arginine is a decisive factor for higher survivability, mitochondrial function and antitumor activity in activated T cells (Geiger, Rieckmann et al. 2016). Therefore, the lack of arginine by TAMs not only suppresses the antitumor activity of T cells, but also reprograms the metabolism of T cells to glycolysis as their primary metabolic pathway (Figure 2). Protein- or amino acid-restricted TAMs exhibit an antitumor phenotype leading to reduced TAM infiltration, inhibited tumor growth and

improved responsiveness to immunotherapies in various animal tumor models (Orillion, Damayanti et al. 2018). Consequently, amino acid metabolism in TAMs significantly influences their phenotypic polarization. In this context, it has been shown that genetic modification and pharmacological inhibition of glutamine synthase (GS), as one of the major enzymes of glutamine metabolism in TAMs, leads to a distinct phenotype characterized by increased expression of major histocompatibility complex class II (MHCII) and decreased expression of CD206, a pro-tumor Mϕ marker (Palmieri, Menga et al. 2017). Importantly, TAMs lacking GS lead to an increase in intratumoral cytotoxic $CD8^+$ T cells and improved vascular integrity, resulting in anti-tumor TME phenotype. Accordingly, knocking out GS in Mϕ has been found to reduce metastasis rates in the murine lung tumor model (Palmieri, Menga et al. 2017). Overall, GS-mediated glutamine production promotes a pro-tumor phenotype in TAMs, underscoring the importance of glutamine metabolism as the most abundant amino acid in humans with important immunological functions (Cruzat, Macedo Rogero et al. 2018) (Figure 2). However, the intricate interplay between glutamine and glutamate in TAMs and cancer cells should be further investigated, as TAM-associated glutamine could serve as a resource to replenish the TCA cycle in cancer cells (Mazzone, Menga et al. 2018).

1.4.4.2 Fatty acid metabolism

Fatty acids are essential components for the formation and maintenance of cell membranes. They ensure the stability and flexibility of cell membranes, which not only support cellular integrity by separating them from the extracellular environment, but also directly influence the ability of cells to interact with their environment. In addition, fatty acids serve as a valuable energy source for cells, primarily via FAO to generate adenosine triphosphate (ATP) as an energy currency for various cellular activities. Beyond their structural and energy-related functions, fatty acids can act as messengers that facilitate communication between cells and coordinate responses to external stimuli (Koundouros and Poulogiannis 2020). Interestingly, TAMs have been shown to exhibit higher lipid accumulation due to increased lipid uptake from the extracellular environment. The accumulated lipids were consumed by FAO not only to support mitochondrial functions but also to induce the signature of pro-tumor genes through stimulation of STAT6 (Su, Wang et al. 2020)**.** In addition to the cell-autonomous function of the fatty acid, the TAMs use the fatty acids as a means of communication to directly influence cancer cells and other TME components. In this context, it was found that the extracellular vesicles of TAMs (TAM-EVs) contain an immunostimulatory molecular pattern similar to that of anti-tumor Mϕ. These TAM-EVs are enriched with components of lipid metabolism, in particular arachidonic acid metabolism. The proteomic signature

of TAM-EVs shows an upregulation of key enzymes such as cyclooxygenase 1, thromboxane A synthase-1 and specific cytochrome P450 epoxygenases (Cianciaruso, Beltraminelli et al. 2019). Interestingly, TAMs use these TAM-EVs to remodel the arachidonic acid degradation pathway in cancer cells. This switch leads to the production of thromboxane B2 (TXB2) and a reduction of prostaglandins in the tumor microenvironment (Cianciaruso, Beltraminelli et al. 2019) (Figure 2). This discovery highlights the intricate intercellular interactions that fine-tune lipid metabolism in the TME, where lipid metabolites have innate immune properties and can influence the metabolic profiles of different cell types.

1.4.4.3 Glucose metabolism

Glucose metabolism plays a vital role in providing energy and intermediate metabolites to Mϕ. Glucose serves as the primary source for ATP production through two interconnected metabolic pathways: glycolysis in cytoplasm and oxidative phosphorylation (OXPHOS), including the TCA cycle in mitochondria. Glycolysis is a nearly ubiquitous process that converts glucose into pyruvate. In the presence of oxygen, pyruvate is undergone complete oxidation in mitochondria resulting in the production of ATP, carbon dioxide and water. In conditions of oxygen deficiency, pyruvate is converted mainly to lactic acid (Kelly and O'Neill 2015). TAMs show a higher uptake of 18F-fluorodeoxyglucose (FDG), a glucose analog, compared to cancer cells and other immune cells within the TME (Reinfeld, Madden et al. 2021). This increase is reflected in increased extracellular acid rate as indicator of glycolysis and increased oxygen consumption rate, resulting in TAMs having higher glucose metabolic activity compared to cancer cells and T cell populations (Reinfeld, Madden et al. 2021) (Figure 2).

The dependence of TAMs on glycolysis is associated with the recruitment of TAMs and tumor development. Glycolysis plays a crucial role in the migration of TAMs from oxygen-rich blood vessels to hypoxic areas in the TME. Inhibition of Mϕ glycolysis with dichloroacetic acid significantly impairs TAM migration, even in a lung tumor xenograft model in which Mϕ migration to implanted matrigel is greatly reduced by this inhibition (Semba, Takeda et al. 2016). The energy-consuming process of cell migration is supported by glycolysis, which produces ATP, which is required for cytoskeletal remodeling. This is confirmed by the co-localization of pyruvate kinase muscle2, a key enzyme of glycolysis for ATP production, with F-actin in filopodia and lamellipodia of Mϕ, structures that are critical for Mϕ migration (Pantaloni, Le Clainche et al. 2001). While the specific TAM phenotype during cancer cell initiation remains unclear, the glycolytic phenotype appears to be a fundamental feature of TAMs in the early stages of tumorigenesis.

After the TAMs have colonized and the tumor has established itself, the TME transforms into a Th2-type environment. Here, the TAMs undergo polarization and maintain their highly glycolytic phenotype under the influence of various factors, including IL-4 and colony stimulating factor 1 receptor (CSF1R), where the availability of oxygen and nutrients is under limitation (Lin, Gouon-Evans et al. 2002, Gocheva, Wang et al. 2010). In the hypoxic TME range, TAMs also show an increased rate of glycolysis with a proangiogenic phenotype through the production of growth factors such as vascular endothelial growth factor (VEGF) and platelet-derived growth factor (PDGF) (Henze and Mazzone 2016). From a mechanistic point of view, mammalian target of rapamycin (mTOR) has been shown to play the key role in the glycolytic and proangiogenic properties of TAMs. Accordingly, the application of the mTOR inhibitor rapamycin not only reduces the size of TAMs, but also attenuates glucose uptake by TAMs (Reinfeld, Madden et al. 2021). However, deletion of REDD1 (regulated in development and DNA damage responses 1) as an mTOR inhibitor in hypoxic TAMs further enhances the rate of glycolysis. Interestingly, this shift leads to a reduction in metastatic burden by creating competition for glucose between TAMs and endothelial cells, which subsequently results in normal vascularization (Wenes, Shang et al. 2016). This precise fine-tuning of the high rate of glycolysis in TAMs not only support the pro-metastatic capacity of TAMs, but also maintain an optimal glucose concentration in the perivascular space. This in turn leads to hyperactivation of endothelial cells and disrupts the organization of the tumor vasculature. In summary, the glycolytic phenotype observed in TAMs can be considered an intrinsic feature that confers pro-tumor functions to TAMs. This glycolytic phenotype promotes a metabolic partnership with cancer cells and other TME components, thus contributing to the creation of a pro-invasive TME.

However, in compared to glycolysis, there is not much information about TCA cycle and mitochondria metabolism in TAMs. One possible explanation can be, as mentioned earlier, glycolysis is prominent glucose metabolism in TAMs and consequently TCA cycle is non-functional in TAMs. Given the pro-tumor functional of glycolysis, it can be plausible that glucose metabolism in mitochondria render the anti-tumor phenotype to TAMs mainly in early stages of lung tumors when TAMs have anti-tumor phenotype (Singhal, Stadanlick et al. 2019).

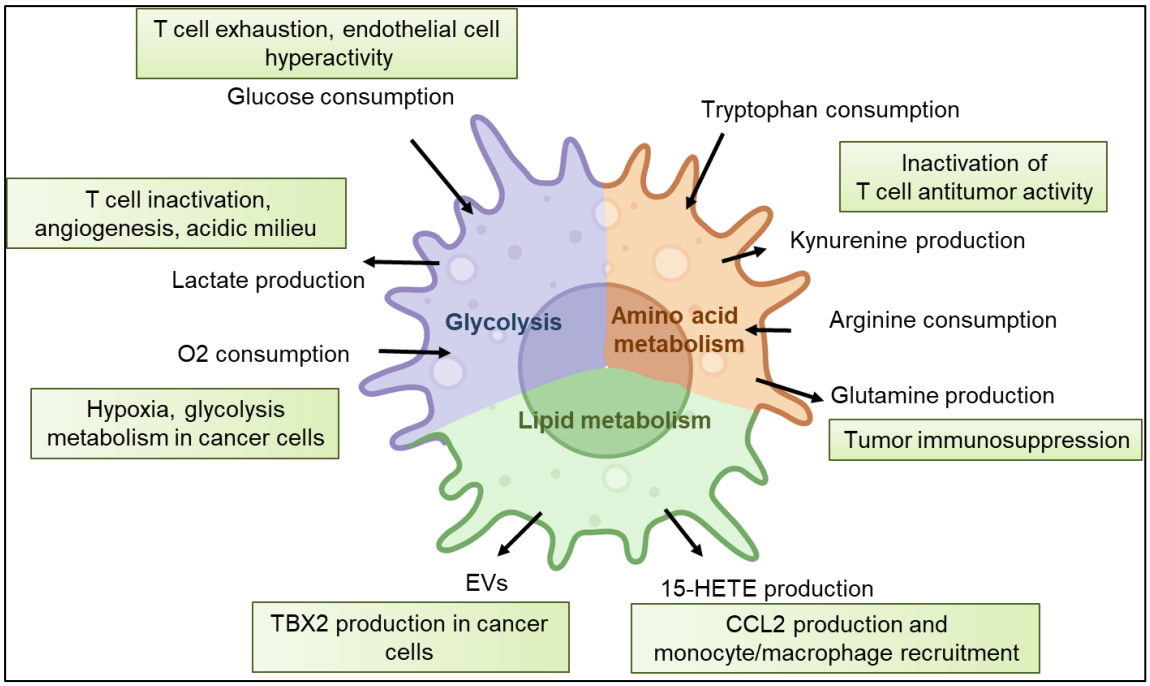

Figure 1-2. Metabolic phenotype of TAMs and their impact on TME and cancer cells. The direction of the arrow indicates whether the metabolites are secreted or taken up by the Mϕ. The green box indicates the function of the associated metabolite(s). HETE: hydroxyeicosatetraenoic acid. EV: extracellular vesicle). TXB2: thromboxane B2. The figure was prepared in www.Biorender.com with this agreement number: *JO26EKYGM9*.

1.4.4.4 IRG1/Itaconic acid axis

Itaconate, a metabolite abundantly produced by Mϕ during the pro-inflammatory polarization of Mϕ triggered by various factors such as LPS, viral components or IFNγ, plays a crucial role in immunomodulation (Lampropoulou, Sergushichev et al. 2016, Hooftman and O'Neill 2019, Swain, Bambouskova et al. 2020). A gene called IRG1 (immune responsive gene 1, also known as Acod1) is responsible for the production of itaconate in the mitochondria of activated Mϕ under pro-inflammatory condition (Lee, Jenkins et al. 1995, Michelucci, Cordes et al. 2013). In pro-inflammatory situations, IRG1/itaconate and its derivatives have immunomodulatory functions in Mϕ. They inhibit succinate dehydrogenase (SDHA) and glyceraldehyde-3-phosphate dehydrogenase (GAPDH) and TET-family DNA dioxygenases while activate nuclear factor erythroid 2-related factor 2 (NRF2) and activating transcription factor 3 (ATF3) (Lampropoulou, Sergushichev et al. 2016, Mills, Ryan et al. 2018, Liao, Han et al. 2019, Chen, Morcelle et al. 2022). In contrast, anti-inflammatory Mϕ downregulate the expression of IRG1/itaconate through mechanisms involving the nuclear receptor peroxisome proliferator-activated receptor γ (PPARγ) and the microRNA miR-93/IRF9 axis, highlighting the inhibitory role of IRG1/itaconate in the polarization of anti-inflammatory

Mϕ (Ganta, Choi et al. 2017, Nelson, Nguyen et al. 2018). Importantly, supplementing anti-inflammatory Mϕ with itaconate or its derivative, 4-octyl-itaconate (Octyl Ita), shifts them to a pro-inflammatory phenotype and suppresses the Janus Kinase 1 (JAK1)/STAT6 pathway required for anti-inflammatory polarization (Runtsch, Angiari et al. 2022). These results indicate that IRG1/itaconate is a characteristic feature of anti-tumor Mϕ that should be suppressed in pro-tumor Mϕ to counteract its immunomodulatory effects.

2 The aim of study

The TME is a stressful environment in which oxygen levels, pH and nutrient availability are finely tuned not only by cell-autonomous regulation but also by a precise metabolic interplay between different TME components, in particular TAMs and cancer cells. TAMs can exhibit either anti-tumor or pro-tumor functions. Interestingly, these two phenotypes are associated with completely different metabolic profiles of TAMs. Itaconate is one of the unique metabolites produced during the pro-inflammatory response in Mϕ. Considering the anti-tumor functions of pro-inflammatory Mϕ, this study investigates the functional role of itaconate and IRG1 as its response gene in lung tumorigenesis and evaluates the therapeutic potential of Octyl Ita in human and mouse lung cancer models. For this study we have set ourselves the following aims (Figure 2-1);

1. Understanding the role of Irg1 in lung tumorigenesis in mice using different lung tumor models in mice.
2. Clarify the effects of itaconate and Octyl Ita on lung tumorigenesis *in vitro*, *ex vivo* and *in vivo*.
3. Identify the underlying mechanisms by which Octyl Ita affects lung cancer cell growth and proliferation.
4. Investigate the potential effects of Octyl Ita on tumor friendly Mϕ and the underlying mechanisms.
5. Evaluate the potential role of IRG1 in conferring an anti-tumor phenotype to anti-tumor Mϕ.

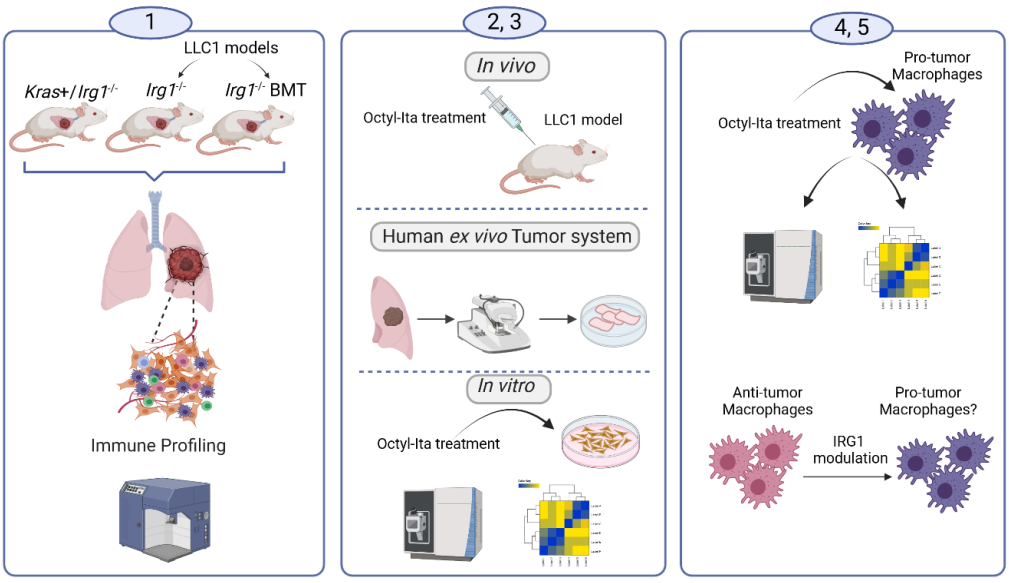

Figure 2-1. Aims of study. The figure was prepared in www.Biorender.com with this agreement number: *PR26EKYNP6.*

3 Materials and Methods

3.1 Cell biological methods & cell culture

3.1.1 Cell cultivation

Human lung cancer cell lines A549, H838, H1975, H1650, H226 and mouse lung cancer cell line LLC1 were purchased from the American Type Culture Collection (ATCC, Manassas, USA) and cultured under cell culture conditions according to ATCC guidelines and incubated at 37 °C in an atmosphere of 5 % CO_2 in 75 cm² cell culture flasks. Cells were divided every 2–3 days with trypsin/EDTA (25200056) when they were 80-90% confluent. A549 cells were cultured in Dulbecco's modified Eagle's medium supplemented (DMEM, 41965 039) with 10 % (v/v) fetal calf serum (FCS, 10500-064) and 1 % (v/v) penicillin/streptomycin (P/S, 15140-122). Other human cell lines and LLC1 cells were cultured in RPMI 1640 medium (21875-034) supplemented with 10% (v/v) FCS and 1% (v/v) P/S. All cell lines were tested for mycoplasma using the LookOut® Mycoplasma PCR Detection Kit (Merck, Darmstadt, Germany). All the cell culture materials mentioned above were purchased from Gibco® life technologies, USA.

For long-term storage, we centrifuged the cells after trypsinization and then suspended the cell pellet in freezing medium including 90 % FCS, 10 % dimethyl sulfoxide (DMSO, D2438, Sigma-Aldrich, USA). The cells were then stored in tanks with liquid nitrogen. To reuse the frozen cells, we first placed the cryotubes in a 37 °C water bath to partially thaw the cells. Then the pre-warmed medium was added to the cell suspension to gradually and completely thaw the cells. Finally, the cells were centrifuged and the cell pellets were resuspended in the appropriate culture media for each cell type and seeded into a new 75 cm² flask.

3.1.2 Generation of macrophages

Human Mϕ were generated from peripheral blood mononuclear cells (PBMCs) as previously described (Sarode, Zheng et al. 2020, Karger, Mansouri et al. 2023). For this purpose, we isolated PBMCs from buffy coats obtained from the blood bank of the Lung Center of the Universities of Giessen and Marburg using Ficoll density gradient centrifugation. The research with these blood samples was ethically approved by the Ethics Committee under file number AZ 58/15. We added 15 ml of Ficoll-Paque media (L6115, BIOCOLL Biochrom AG, Germany) to Leucosep centrifuge tubes (227290, Greiner Bio-one, Germany). We then carefully layered the blood samples onto the media. The centrifugation process was performed for 35 minutes at 440 g without applying the brakes. After centrifugation, the upper white layer with the separated mononuclear cells was carefully transferred to a new 50 ml Falcon tube. Platelets and red blood cells

(RBCs) were removed by two washes with RBC lysis buffer (555899, BD Biosciences, Germany) and phosphate-buffered saline (PBS, 14190-094, Gibco® life technologies, USA), respectively. Then, PBMCs were seeded on 6-well plates (83.3920.300, Sarstedt, Germany) in RPMI 1640 medium supplemented with 1% (v/v) P/S. After 2 hours, the non-adherent cells were removed. The remaining adherent cells were differentiated into Mϕ for 10 days in Mϕ complete medium (RPMI 1640 media supplemented with 2% (v/v) human serum and 1% (v/v) P/S).

For the isolation and differentiation of mouse Mϕ, we first sterilized the skin of the mice with 80% ethanol and then dissected the tibia and femur of the mice. We then rinsed each bone with 15 ml RPMI 1640 medium containing 1% (v/v) P/S. The cell suspension was passed through a 40-µM cell strainer (CLS431750-50EA, Merck, Germany) and then centrifuged at 500 g for 10 minutes. The supernatant was then removed and the cell pellet was suspended in RPMI 1640 medium containing 10% (v/v) FCS, 1% (v/v) P/S and mouse Mϕ colony-stimulating factor (M-CSF) (20 ng/ml; 416-ML, R and D System, USA) and seeded onto a six-well plate. The medium was alternated with RPMI 1640 medium containing 10% (v/v) FCS, 1% (v/v) P/S and mouse M-CSF (20 ng/ml) until differentiated Mϕ were obtained after 5-6 days.

For Mϕ polarization, we generated anti-tumor Mϕ by stimulating unpolarized Mϕ with LPS (100ng/ml; L5418, Sigma-Aldrich, USA) and IFNɣ (100U/ml; 285-IF, R and D Systems, USA) for 6 hours or 24 hours as indicated in each specific experiment. For the generation of pro-tumor Mϕ, unpolarized Mϕ were treated with IL-4 (20ng/ml; 204-IL, R and D Systems, USA) for 24 hours.

Regarding cell treatment with metabolites, it should be noted that the pH of the media was checked after dissolving the metabolites and adjusted between 7.2 and 7.4 before treating the cells. The metabolites were used in this thesis listed as; Octyl Ita (25374, Cayman, USA) dimethyl fumarate (sc-239774, Santa Cruz, USA). The rest of metabolites were purchased from Sigma, USA including, itaconate (I29204), dimethyl malonate (136441), diethyl succinate (112402), D-ribose (R9629), ribose-5-phosphate (R7750), 6-phosphogluconate (P7877).

3.1.3 Indirect co-culture

LLC1 and Mϕ co-culture experiments were performed using a Transwell system (83.3930.800, Sarstedt, Germany), which allows co-culture of different cell types in indirect contact. Initially, $0.5x10^6$ LLC1 cells were placed on inverted transwells and allowed to adhere for 2 hours before being positioned on cell culture plates containing $0.5x10^6$ mouse Mϕ per well. As a control, LLC1 and Mϕ were seeded separately. The

entire co-culture process was performed in RPMI 1640 supplemented with 10% FCS. After 24 hours, the supernatant (referred to as conditioned medium (CM)) was collected and stored at -80°C for future experiments.

3.1.4 Transfection with siRNA

The Mϕ and A549 cells were transfected with different siRNAs. The transfection reagent HiPerFect (371707, Qiagen, Hilden, Germany) and serum-free Opti-MEM medium (11058021, Sigma-Aldrich, Taufkirchen, Germany) was used according to the manufacturer's protocol. First, the HiPerFect reagent was added to the Opti-MEM medium and vortexed briefly. Then the siRNAs were added and carefully mixed and incubated for 5–10 minutes at room temperature. In the meantime, the Mϕ or A549 medium was removed and the transfection mixture was added dropwise over the cells and incubated for 6 hours. The complete medium was then added for a further 24 or 48 hours. All siRNAs were purchased from Qiagen (Qiagen, Hilden, Germany) as shown in Table 3-1.

Table 3-1. Custom siRNAs used for knockdown of the respective gene.

Target RNA	siRNA name	Catalog Nr.	Company	Final con.
Negative control	AllStars negative	1027292	Qiagen	25nM
IRG1	Hs_IRG1_4	SI05379920	Qiagen	25nM
IRG1	Hs_IRG1_3	SI05172685	Qiagen	25nM
G6PD	Hs_G6PD_6	SI03082450	Qiagen	25nM
G6PD	Hs_G6PD_2	SI00008862	Qiagen	25nM

3.1.5 Transfection with plasmid

We transfected A549 and H1650 with IRG1 overexpressing (catalog number: Ex-I1206-Lv105) and empty control plasmid (catalog number: Ex-NEG-Lv105) from GeneCopoeia (Rockville, USA) using TurboFect transfection reagent (R0531, Fermentas, USA). According to the protocol, we transfected A549 cells with the IRG1 overexpressing plasmid (1 µg) in parallel with the empty control plasmid (1 µg) in TurboFect reagent and incubated the cells for 24 hours or longer as indicated.

3.2 Cellular functional assays

3.2.1 Proliferation and apoptosis assay

We seeded cancer cells (A549 or H1650) at a number of 6,000 cells per well in a 96-well plate and allowed them to grow for 24 hours, followed by serum starvation for another

24 hours. After starvation, the cancer cells were incubated for a further 24 or 48 hours with different Mϕ CM and different metabolites or reagents as indicated in the results section. On the following day, we checked cell proliferation and apoptosis using a bromodeoxyuridine (BrdU) cell proliferation assay kit (11647229001, Roche Diagnostics GmbH, Germany) and cell death detection kit (11920685001, Roche Diagnostics GmbH, Germany), according to the manufacturer's protocol.

For cell proliferation rate, the BrdU assay was used as a colorimetric immunoassay that measures the incorporation of BrdU during DNA synthesis. The cells were exposed to the BrdU labeling solution and incubated for a further 90 minutes at 37°C in an atmosphere of 5% CO_2. To fix the cells, the labeling medium was replaced with 200 µl/well FixDenat for 30 minutes at room temperature. After fixation, the solution was removed by gently swirling and tapping. Then 100 µl/well anti-BrdU-POD solution (diluted 1:100) was added and incubated for 2 hours at room temperature in the dark. After that, the antibody conjugate was removed by stripping and the wells were washed three times with 300 µl/well of wash solution. Finally, 100 µl/well of substrate solution was added and cell proliferation was determined by measuring the absorbance at 370 nm with a reference wavelength of 492 nm (infinite M200 PRO, Tecan Group, Maennedorf, Switzerland).

To determine the degree of apoptosis of the cells, we used the Cell Death Detection ELISAPLUS kit from Roche according to the manufacturer's instructions. After cellular treatment, the cells were centrifuged at 200 g for 10 minutes and then the supernatant was removed. Subsequently, 200 µl 1x lysis buffer was added to each well and incubated for 30 minutes. After lysis, a further 10-minute centrifugation at 200 g was performed to pellet the cell debris and 20 µl of the supernatant was transferred to the streptavidin-coated microplate wells provided in the kit. To each well, 80 µl of the freshly prepared immunoreagent from the kit was added and the plate was shaken at 300 rpm for 2 hours in the dark. The solution was then removed by tapping and the wells were rinsed three times with 200 µl of incubation buffer. After the last wash step, the wash solution was removed and 100 µl of the ABTS solution was added to each well. The analysis was performed by measuring the absorbance at 405 nm with a reference wavelength of 490 nm (infinite M200 PRO, Tecan Group, Maennedorf, Switzerland).

3.3 Molecular biology

3.3.1 RNA isolation

Total RNA was extracted with RNeasy Mini Kit (74104, Qiagen, Germany) as described before (Sarode, Zheng et al. 2020, Karger, Mansouri et al. 2023). The process involved

washing the adherent cells with PBS followed by immediate lysis with TRIzol (79306, Qiagen, Germany) 700 µl per condition. The lysates were then transferred to a separate tube and homogenized by several pipetting steps using a 1 ml pipette. Subsequently, 140 µl of chloroform was added per 700 µl of TRIzol. The tube was shaken for 15 seconds, incubated at room temperature for 2 minutes and then centrifuged at 12,000 g at 4°C for 15 minutes. This centrifugation step led to the separation of the upper aqueous phase, which was then transferred to a new tube to avoid any contamination with the lower layers.

To precipitate the RNA from this aqueous phase, 450 µl of 100% ethanol per 300 µl of the aqueous phase was added and mixed by pipetting two or three times and applied to the top of the RNA isolation column from the kit. The columns were centrifuged at 10,000 g for 15 seconds at room temperature. The collected liquid was removed and the columns were washed in three steps with the wash solutions provided in the kit and finally with 80% ethanol. All washing steps were performed at 10,000 g centrifugation for 15 seconds at room temperature, except the last step with 80% ethanol for 2 minutes. The columns were then dried by centrifugation only at 10,000 g for 5 minutes at room temperature. Finally, the RNA was eluted by adding 14 µl of RNase-free water to the top of the column, followed by centrifugation at 12,000 g for 1 minute at room temperature. The concentration and purity of the RNA were determined using a spectrometer (ThermoFisher Scientific, USA) and the RNA was stored long-term at -80°C.

3.3.2 Complementary DNA synthesis, and quantitative PCR

The RNA was then transcribed into complementary DNA (cDNA) using the High-Capacity cDNA Reverse Transcription Kit (4368814, Applied Biosystems, USA) according to the manufacturer's instructions. The reaction solution protocol and temperature programs used for the conversion of RNA to cDNA are listed in Table 3-2 and Table 3-3.

Table 3-2. Reaction mix and temperature program used for reverse transcription

Reagent	Volume [µl]
RNA template	1 µg in 10 µl
10x RT Buffer	2
10x RT Random Primer	2
dNTPs (100 mM)	0.8
MultiScribe Reverse Transcriptase (50 U/µl)	1
RNase Inhibitor (20 U/µl)	1
RNase free water	3.2

Table 3-3. Reverse transcription program

Time	Temperature
10 min	25 °C
120 min	37 °C
5 min	85 °C
∞	4 °C

Quantitative PCR (qPCR) was then performed using the SYBR Green PCR Master Mix (A25742, Applied Biosystems, USA) (Table 3-4) in the StepOne real-time PCR System (Applied Biosystems, USA) under the following conditions: 10 min at 95°C, followed by 40 cycles of 30s at 95°C, 30s at 58°C to 60°C. Analysis was performed using StepOne plus software and GraphPad Prism. Expression was determined using the ΔΔCT method, followed by fold change calculation. CT values were normalized to the housekeeping gene encoding hypoxanthine-guanine phosphoribosyl transferase (HPRT1) using the equation $\Delta CT = CT_{reference} - CT_{target}$. For each q-PCR run, a no template control which contains RNase-free water instead of template was included as a technical control to exclude any cDNA template from the reaction, thereby checking for extraneous nucleic acid contamination. In order to assess the qPCR efficiency and specificity, we analyzed both the efficiency of the PCR reaction itself and the melt curve. We ensured that the amplicon displayed a single peak, and that the reactions with serially diluted templates exhibited an efficiency more than of 90%. The primer sequences were designed using sequence information from the National Center for Biotechnology Information database and purchased from Sigma-Aldrich (USA) (see Table 3-5).

Table 3-4. qPCR reaction mixture

Reagent	Volume [µl]
Template cDNA (1:20 dilution)	4
SYBR green mix (Applied Biosystems)	5
Forward primer (10 µM)	0.5
Reverse Primer (10 µM)	0.5

Table 3-5. qPCR primer list

Gene	Sequence (5`–3`)	
Human HPRT	FP	TGACACTGGCAAAACAATGCA
	RP	GGTCCTTTTCACCAGCAAGCT
Human G6PD	FP	TGACCTGGCCAAGAAGAAGA
	RP	CAAAGAAGTCCTCCAGCTTG
Human TNFα	FP	GAGGCCAAGCCCTGGTATG
	RP	CGGGCCGATTGATCTCAGC
Human CSF-1R	FP	GAGAGCTATGAGGGCAACAG
	RP	TCCGAGGGTCTTACCAAACT
Human PGDH	FP	ATATAGGGACACCACAAGACGG
	RP	GCATGAGCGATGGGCCATA
Human TKT	FP	GCTGAACCTGAGGAAGATCA
	RP	TGTCGAAGTATTTGCCGGTG
Human TALDO1	FP	GTCATCAACCTGGGAAGGAA
	RP	CAACAAATGGGGAGATGAGG
Human IRG1	FP	GAGAGAGCCCTGCTTCCAAC
	RP	TGGCCTGTTGATCTGGCATT
Mouse HPRT	FP	GCTGACCTGCTGGATTACAT
	RP	TTGGGGCTGTACTGCTTAAC
Mouse TNFα	FP	CATCTTCTCAAAATTCGAGTGACAA
	RP	TGGGAGTAGACAAGGTACAACCC
Mouse Arginase1	FP	GGTTCTGGGAGGCCTATCTT
	RP	CACCTCCTCTGCTGTCTTCC
Mouse Fizz1	FP	GGAACTTCTTGCCAATCCAGC
	RP	AAGCACACCCAGTAGCAGTC

3.3.3 Protein isolation and western blotting

The RIPA lysis buffer was used to lyse the Mϕ and A549 cells. For this purpose, the cells were washed with PBS before being collected in RIPA buffer (sc-249482, Santa Cruz Biotechnologies, USA) supplemented with proteinase inhibitor, phenylmethylsulfonyl

fluoride (PMSF) and sodium orthovanadate. The cell suspension was placed on ice and incubated for 10 minutes. The cells were then centrifuged at 12,000 g for 15 minutes at 4°C, which led to the separation of the protein-containing supernatant. This supernatant was then carefully transferred to a fresh 1.5 ml Eppendorf tube and kept on ice. Quantification of proteins was performed using a modified Lowry assay and the DC™ Protein Assay Kit (5000111 and 5000112, Bio-Rad, Germany). A series of protein standards with different concentrations of bovine serum albumin (BSA), ranging from 0.125 to 2 µg/µl, were used as reference. The resulting blue color development as protein concentration was evaluated at a wavelength of 750 nm using a microplate reader (infinite M200 PRO, Tecan Group, Maennedorf, Switzerland). Then the protein samples that had the same protein concentration were mixed with 5x sodium dodecyl-sulfate (SDS) (1057.1, Carl Roth, Germany) sample loading buffer and boiled at 95°C for 3-5 minutes.

Subsequently, the heat-denatured proteins were separated using 10% SDS-polyacrylamide gels and transferred to polyvinylidene difluoride membranes (1620264, Bio-Rad, USA). After blocking with 5% (w/v) BSA in Tris-buffered saline with Tween 20 (TBST) formulated as 20 mM Tris (4855.2, Carl Roth, Germany), 150 mM NaCl (3957.1, Carl Roth, Germany) and 0.1% (w/v) Tween®-20 (P1379, Sigma, USA) detergent, the membranes were incubated with a primary antibody diluted 1:1000 in 5% (w/v) BSA/TBST with constant shaking overnight at 4°C. After washing 3 times with TBST, the blots were incubated with secondary antibodies coupled with horseradish peroxidase dissolved in 5% milk in TBST buffer. The protein-antibody conjugates were detected using an enhanced chemiluminescence detection system by adding WesternBright™ ECL or Sirius (K-12045-D20 or K-12043-D20, Advansta, California, USA) solution. Protein expression was quantified using band intensity values (in arbitrary units) normalized to β-actin (ACTB) or glyceraldehyde-3-phosphate dehydrogenase (GAPDH) using ImageJ software. The Western blots shown in the figure are representative of 3 independent experiments, unless mentioned in the figure legends. Details of the antibodies can be found in Table 3-6.

Table 3-6. List of primary and secondary antibodies

Antibody	Catalog number	Company	Application
GAPDH	MA5-15738	Invitrogen	WB 1;5000
Anti-IRG1	77510	Cell signaling	WB 1;1000
Anti-G6PD	12263	Cell signaling	WB 1;1000
Anti-HMOX1	70081	Cell signaling	WB 1;1000
Anti-Beta actin	Ab8272	Abcam	WB 1;5000
Anti-mouse IgG HRP-linked	W4018	Promega	WB 1;10000
Anti-rabbit IgG HRP-linked	W4028	Promega	WB 1;10000
CD68	Ab-955	Abcam	IF 1;300
ACOD1	ab238580	Abcam	IF 1;100
Fluor 488 goat anti-rabbit IgG	A11008	Life technologies	IF 1;1000
Fluor 647 donkey anti-mouse IgG	A31571	Life technologies	IF 1;1000
PCNA	Sc-56	Santa Cruz	IF 1;200
Anti-Caspase8	Ab227430	Abcam	IF 1;300

3.4 Cell isolation from human lung tissues

3.4.1 Human lung tissues

Lung tissue samples were acquired in RPMI medium supplemented with 10µg/mL cycloheximide (C4859, Sigma-Aldrich, St. Louis, USA) from the Institute for Pathology in Giessen, Germany. The specimens were kept at 4°C on to start the cell isolation procedure in the same day. The study protocol for tissue donation received approval from the ethics committee ("Ethik Kommission am Fachbereich Humannmedizin der Justus Liebig Universität Giessen") at the University Hospital Giessen, in compliance with national regulations and "Good Clinical Practice/International Conference on Harmonisation" guidelines. Written informed consent was obtained from each patient (reference ethical number: AZ 58/15).

3.4.2 MACS sorting of TAMs from human

To isolate TAMs from human lung tumors and normal tissue, we started the process by preparing single cell suspensions. Human lung tumor single-cell suspensions were

prepared using the Tumor Dissociation Kit (130-095-929, Miltenyi Biotec, Germany) according to the manufacturer's instructions. Accordingly, the enzyme mixture for 0.2-1.0 gram tissue was prepared by adding 200 µl of enzyme H, 100 µl enzyme R and 15 µl of enzyme A in 4.7 ml of RPMI 1640 media. The enzyme mix was transferred into gentleMACS™ C Tube (130-093-237, Miltenyi Biotec, Germany). The tumor sample was chopped precisely into 2–4 mm small pieces then transferred into gentleMACS™ C Tube. The sample dissociation was started by placing the tubes on gentleMACS Dissociator (Miltenyi Biotec, Germany) by running gentleMACS program h_tumor_01 followed by incubation of sample for 20 minutes at 37°C under continuous rotation using the MACSmix™ Tube Rotator (Miltenyi Biotec, Germany). The dissociation procedure was stopped by adding 15 ml of RPMI 1640. Thereafter, the tube was centrifuged at 500 g for 10 minutes at 4°C and the cell pellet was suspended in 20 ml RPMI 1640 media followed by filtering through a MACS SmartStrainer (30 µm, 130-098-458, Miltenyi Biotec, Germany) placed on a 50 ml tube. The cells were collected with centrifugation at 500 g for 10 minutes at 4°C. Then, RBC was lysed by incubation with 1X RBC lysis buffer for 15 minutes followed by centrifugation at 500 g for 10 minutes. The cell pellet washed with 20 ml of RPMI 1640 and resuspended as required for further applications.

Mϕ were isolated from single-cell suspensions using magnetic sorting with primary antibody CD68-PE human (130-096-807, Miltenyi Biotec, Germany) and secondary antibody Anti-PE MicroBeads (130-048-801, Miltenyi Biotec, Germany), following the manufacturer's instructions. Briefly, a total of 10^7 cells were washed using 1-2 m of buffer containing PBS, pH 7.2, 0.5% BSA, and 2 mM EDTA (8040.3, Carl Roth, Germany) then centrifuged at 500 g for 10 minutes. The cell pellet was then resuspended in 100 µl of the buffer and mixed with 10 µL of CD68-PE antibody, followed by a 10 minutes incubation in the dark at 2-8°C. To remove unbound primary antibody, 1-2 ml of the buffer per 10^7 cells were added and centrifuged at 500g for 10 minutes. The cell pellet was subsequently resuspended in 80 µl of the buffer, and 20 µl of Anti-PE microbeads per 10^7 cells were added and incubated for 15 minutes in the dark at 2-8°C. Again, unbound antibody was removed by adding 1-2 ml of buffer per 10^7 cells then the samples were centrifuged at 300g for 10 minutes. The pellet was resuspended in 500 µl of buffer and then applied on LS column (130-042-401, Miltenyi Biotec, Germany) attached to a magnetic field separator. Thereafter, the column was washed three times with the buffer. After the final wash, 5 ml of buffer was applied on column after removing from the magnetic separator then CD68 positive cells were flushed out by firmly pushing the plunger into the column. The cells were centrifuged at 300g for 10 minutes and the pellet were used based on experimental plans.

3.4.3 Flow cytometry and cell sorting

Single-cell suspensions were prepared as mentioned in 3.4.2 and then blocked with FcR blocking reagent (Miltenyi Biotec) in 0.5% PBS-BSA for 20 min, stained with fluorochrome-conjugated antibodies and analyzed on a FACSSymphony A5SE flow cytometer (BD Biosciences). Live single cells were identified by FSC/SSC characteristics. Data were analyzed using FlowJo V10 (TreeStar). All antibodies and secondary reagents were titrated to determine optimal concentrations. Comp-Beads (BD) were used for single-color compensation to create multicolor compensation matrices. For gating, fluorescence minus one controls were used. The instrument calibration was controlled daily using Cytometer Setup and Tracking beads (BD Biosciences). The following antibodies were used: anti-CD3-PE-CF594, anti-CD4-BV711, anti-CD8-BV650, anti-CD11b-BV605, anti-CD11c-AlexaFluor700, anti-CD19-APC-H7, anti-Ly6C-Per-CP-Cy5.5, anti-CD80 PE (BD Biosciences), anti-CD45-VioBlue, anti-MHC-II-APC (Miltenyi Biotec), anti-F4/80-PE-Cy7, anti-CD206-FITC, and anti-Ly6G-APC-Cy7 (BioLegend).

3.5 RNA-seq analysis

For RNA-seq, RNA was isolated from Mϕ and A549 cells using the miRNeasy micro-Kit (217084, Qiagen, Hilden, Germany) combined with on-column DNase digestion (DNase-Free DNase Set, Qiagen) to avoid contamination by genomic DNA. RNA and library preparation integrity were verified with LabChip Gx Touch 24 (Perkin Elmer). 1µg of total RNA was used as input for SMARTer Stranded Total RNA Sample Prep Kit - HI Mammalian (Clontech). Sequencing was performed on the NextSeq500 instrument (Illumina) using v2 chemistry with 1x75bp single end setup. The resulting raw reads were assessed for quality, adapter content and duplication rates with FastQC (Available online at: http://www.bioinformatics.babraham.ac.uk/projects/fastqc). Trimmomatic version 0.33 was employed to trim reads after a quality drop below a mean of Q18 in a window of 5 nucleotides (Bolger, Lohse et al. 2014). Only reads above 30 nucleotides were cleared for further analyses. Trimmed and filtered reads were aligned versus the Ensembl human genome version hg38 (ensemble release 99) using STAR 2.7.3a with the parameter "--outFilterMismatchNoverLmax 0.1" to increase the maximum ratio of mismatches to mapped length to 10% (Dobin, Davis et al. 2013). The number of reads aligning to genes was counted with featureCounts 1.6.5 tool from the Subread package (Liao, Smyth et al. 2014). Only reads mapping at least partially inside exons were admitted and aggregated per gene. Reads overlapping multiple genes or aligning to multiple regions were excluded. Differentially expressed genes were identified using DESeq2 version 1.26.0 (Love, Huber et al. 2014). Only genes with a minimum fold

change of +- 1.5 (log2 +-0.59), a maximum Benjamini-Hochberg corrected p-value of 0.05, and a minimum combined mean of 5 reads were deemed to be significantly differentially expressed. The Ensemble annotation was enriched with UniProt data (release 24.03.2017) based on Ensembl gene identifiers (Activities at the Universal Protein Resource (UniProt)).

For public available transcriptomic dataset, the data first was extracted and then preprocessed counts were imported to Scanpy and analyzed using standard packages (Wolf, Angerer et al. 2018).

Sample distribution was accessed by performing principal component analysis (PCA). R package PCAtools v2.6.0 with default settings was used for the analysis. Log2 scaled counts per million data was used as input. Differential gene expression analysis was performed using R package limma v3.50.0 (Ritchie, Phipson et al. 2015). Genes with p.adj < 0.05 were considered as significantly expressed.

3.6 Metabolome measurement via LC-MS/MS

3.6.1 Quantification of Oxylipins by LC-MS/MS

All types of samples were spiked with 10 µL of internal standard solution. The lipids were extracted by a two-phase liquid-liquid extraction. Ethyl acetate was added, the samples were shaken vigorously, centrifuged (10,000 g, 5 min, 4 °C) and the upper organic phase was collected. The extraction was repeated with ethyl acetate + 0.1% formic acid. These lipid extracts were evaporated to dryness under a continuous stream of nitrogen at vacuum pressure and then resuspended in 50/50 methanol/water (with 100 ng/mL flufenamic acid as an internal control). Finally, the samples were analyzed for primary fatty acids and oxylipins by liquid chromatography coupled to tandem mass spectrometry (LC-MS/MS).

The UPLC-MS/MS method is based on Wang et al. (Wang, Armando et al. 2014) with some minor modifications. Reverse phase separation was performed on an Acquity UPLC BEH shield RP18 column (2.1 × 100 mm; 1.7 µm; Waters, Milford, USA) on an Agilent 1290 Infinity LC system (Agilent, Waldbronn, Germany). The mobile phase consisted of (A) ACN/water/acetic acid (60/40/0.02, v/v/v) and (B) ACN/isopropanol (50/50, v/v). Elution of the analytes was performed for 5.8 minutes at a flow rate of 0.5 mL/min. The gradient conditions were as follows: 0–4.5 min, 0.1–55% B; 4.5–5.0 min, 55–99% B; 5.0–5.8 min, 99% B, followed by a re-equilibration step 0.1% B for 2 min. 8 µL of each sample was injected onto the column. The temperature of the column was maintained at 40 °C. Samples were stored at 4 °C until analysis. Mass spectrometry was performed using a QTrap 5500 mass spectrometer (Sciex, Darmstadt, Germany)

equipped with a Turbo V ion source. Electrospray ionization in negative mode was used. The parameters of the ion source were as follows: CUR 20 psi, IS -4500 V, TEM 525 °C, GS1 30 psi, GS2 30 psi, CAD medium (nitrogen was used as collision gas). Analyst 1.6.2 and MultiQuant 3.0 (Sciex, Darmstadt, Germany) were used for data acquisition and analysis, respectively.

3.6.2 Quantification of TCA cycle metabolites

Cell samples were lysed in ice-cold 85% methanol (10 µL/mg) with two freeze-thaw cycles. Medium samples were processed as usual. The homogenate or culture medium was centrifuged (15,000 g, 5 minutes, 4 °C). An equal volume of supernatant was collected, isotope-labeled internal standard was added, and samples were evaporated to dryness in a ConcentratorPlus (Eppendorf, Wesseling-Berzdorf, Germany). Samples were reconstituted in 50 µL water + 0.5% formic acid, transferred to autosampler vials and subsequently analyzed by LC-MS/MS.

Liquid chromatography was performed using an Agilent 1290 Infinity LC system (Agilent, Waldbronn, Germany) consisting of a 1290 Bin Pump, a 1290 TCC column oven, a 1290 sampler and a 1290 thermostat. Reversed-phase LC separation was performed using a Waters Acquity UPLC HSS T3 column (150 mm × 2.1 mm, 1.8 µm (Waters, Eschborn, Germany)) at 40 °C. Gradient elution was performed with 0.5% formic acid in water (mobile phase A) and 0.5% formic acid in methanol (mobile phase B) at a flow rate of 400 µL/min. The gradient conditions were 2% B for 1.5 minutes, followed by a 3-minute gradient to 100% B, followed by a purification and equilibration step, so that the total LC run time was 10 minutes. The injection volume was 2.5 µL for all samples. The temperature of the autosampler was 6 °C. Mass spectrometry was performed using a QTrap 5500 mass spectrometer (Sciex, Darmstadt, Germany) equipped with an ESI TurboIonSpray source. Electrospray ionization at 400 °C and 4500 V in negative ionization mode was used. The gas parameters of the ion source were as follows: CUR 30 psi, GS1 45 psi, GS2 25 psi. The specific MRM transition for each compound was normalized to appropriate isotopically labeled internal standards. Calibration curves were performed with authentic standards. Analyst 1.6.2 and MultiQuant 3.0 (both from Sciex, Darmstadt, Germany), were used for data acquisition and analysis, respectively.

3.7 Metabolic flux analysis

We used a Seahorse XFe96 extracellular flux analyzer (Seahorse Bioscience, Agilent Technologies, USA) to measure oxygen consumption rate (OCR) and extracellular acidity rate (ECAR). Mitochondrial perturbation experiments were performed by sequentially adding 1.5 µM oligomycin, 1 µM FCCP (carbonyl cyanide 4-

(trifluoromethoxy) phenylhydrazone), and 0.5 µM rotenone/antimycin. The glycolysis rate was measure by sequentially adding 1.5 µM oligomycin, 2 gram/liter D-glucose and 100 mM 2-deoxygulatare. The OCR or ECAR changes after addition of the substrate were calculated relative to the rate before injection. The OCR measurement compounds (103015-100) and ECAR analysis reagents (103020-100) were purchased from Agilent Technologies, USA.

3.8 Proteomics analysis

The data was first normalized using different methods using the R package NormalyzerDE v1.12.0 (Willforss, Chawade et al. 2019). Normalization using quantile method was found better and it was used for all downstream analysis. Principal component analysis (PCA) was performed using R package PCAtools v2.6.0 with default settings. Differential expression analysis was performed using R package limma v3.50.0 (Ritchie, Phipson et al. 2015). Proteins with p.adj < 0.05 were considered as significantly expressed.

3.9 Integrative analysis

A weighted co-expression network analysis was performed and co-expression communities were identified separately for proteomics and transcriptomics data. Quantile-normalized data were used as input for proteomics network analysis. Proteins with a variance of less than 0.01 were removed prior to analysis. In addition, Spearman correlations between proteins were calculated and significant correlations (padj < 0.05) were used to construct the co-expression network. Normalized data (transcripts per million (TPM)) were used for transcriptomics network analysis. Genes with a variance of less than 0.1 were removed from the data. Spearman correlations between genes were then calculated and significant correlations (padj < 0.05) were used to construct the co-expression network.

The significant correlations were analyzed in igraph (https://igraph.org). The spearman correlation coefficient was used as edge weight. Modularity maximization through the Leiden algorithm (Traag, Waltman et al. 2019) was used to find co-expression communities. Centrality of the communities were computed by calculating average degree centrality of all nodes in the corresponding community. Functions of the co-expression communities were identified by performing gene-set enrichment using enrichr module from the tool gseapy v0.10.5 (Chen, Tan et al. 2013) (Subramanian, Tamayo et al. 2005). Hallmark gene sets v7.5.1 obtained from the Molecular Signatures Database (MSigDB) was used as reference for the analysis. Significantly enriched gene-sets (p.adj <0.05) of each of the communities of proteomics and transcriptomics co-expression

networks were selected to find the functional overlap between the communities. Fisher's exact test was executed to find the functional relationship between each pair of communities. Significant relationships (padj < 0.1 for Mϕ data and padj < 0.05 for A549 data) were used to define functional similarity between proteomics and transcriptomics co-expression landscape.

3.10 Visualizations

Volcano plots and sankey plots were generated using R package ggplot2 v3.3.5. Heatmaps were created using R package ComplexHeatmap v2.10.0 (Gu, Eils et al. 2016). Bubble plots were created using Cytoscape v3.6.1.

3.11 Olink assay

The Olink Target 96 Panels, developed by Olink Proteomics in Uppsala, Sweden, employ proximity extension assay technology, enabling the simultaneous analysis of 92 different biomarkers with just 1ul of cell lysate sample prepared using RIPA buffer, as described in section 3.3.3 for protein isolation. Binding of target proteins in the sample to the antibody pairs equipped with coupled DNA oligonucleotides is the main principle for 96-plex immunoassay of Olink. Oligonucleotides located in close proximity hybridize and are extended by a DNA polymerase. This process generates double-stranded DNA barcodes, which are subsequently amplified through PCR and quantified using microfluidic real-time PCR. The resulting data undergoes rigorous quality control and normalization procedures employing internal controls to minimize both intra- and inter-assay variations. The outcomes are reported in Normalized Protein eXpression (NPX) values, represented in an arbitrary unit on a log2-scale.

3.12 Glucose-6-phosphate dehydrogenase enzyme activity

For the preparation of the tissue sections, the heart tissue was removed, frozen and stored at −80°C. Tissue blocks embedded in optimal cutting temperature (OCT) preparation were sectioned at a slow and constant speed to 6µm thickness and mounted on the superfrost slides (Carl Roth, Germany). The slides were stored at −80°C for further staining of enzyme activity. Staining of glucose-6-phosphate dehydrogenase (G6PD) enzyme activity on the tissue sections was performed as described by Miller et. al (Miller, Nagy et al. 2017).

In brief, we used 0.1 M Tris-HCl buffer pH 7.5 for the G6PD activity. In the G6PD-specific buffer, 10% polyvinyl alcohol (341584, Sigma, USA) was dissolved at 60°C with stirring until the mixture was clear. Then G6PD-specific assay media were prepared by adding 15 mM D-glucose 6-phosphate (G6P) (G7879, Sigma, USA), 0.8 mM β-nicotinamide adenine dinucleotide phosphate hydrate ($NADP^+$) (N1511, Sigma, USA), 4 mM $MgCl_2$

(M8266, Sigma, USA), 5 mM sodium azide (S2002, Sigma, USA), 0.45 mM 1-Methoxy-5-methylphenazinium methyl sulfate (M8640, Sigma, USA) and 5 mM nitroblue tetrazolium chloride (NBT) (4421.1, Carl Roth, Germany) including negative control reactions with the addition of 30 mM trans-dehydroandrosterone (DHEA) (D4000, Sigma, USA) (for G6PD inhibition). The assay medium containing the enzyme-specific substrates was applied to the entire tissue section. The enzyme reactions were performed at room temperatures for approximately 5-10 minutes or until strong staining was visible and stopped by removing the incubation medium and washing with warm PBS. To remove nonspecific activity, we used DHEA to inhibit G6PD. When we detected nonspecific activity in the presence of DHEA, we subtracted the G6PD activity without DHEA from the activity with DHEA.

For cell lysate, spectrophotometric detection of G6PD activity was conducted according to Miller et al. (Miller, Nagy et al. 2017). In brief, lung cancer cells or Mϕ were sonicated in a G6PD-stabilizing buffer (50 mM Tris (4855.2, Carl Roth, Germany) pH 7.5; 1 mM EDTA (8040.3, Carl Roth, Germany)) and then centrifuged 16000 g, 10 minutes at 4°C. The protein concentration of the supernatant was measured using the BCA protein assay kit as mentioned before. G6PD activity was determined in the presence of 65 mM $MgCl_2$, 0.38 mM $NADP^+$ and varying G6P concentrations from 25µM mM to 2000 µM in 200 µl total reaction volume of 50 mM Tris pH 7.8 in the 96 wells microplate. Reactions were initiated by addition of cell lysate or recombinant G6PD (ab167987, abcam). Enzymatic activity was monitored at 340 nm, controlling the formation of NADPH from NADP+ for 20 minutes at room temperature using a Tecan microplate reader (infinite M200 PRO, Tecan Group, Maennedorf, Switzerland) in kinetic mode (read interval = 25 seconds). As a negative control, we measured the absorbance at 340 nm in 200 µl total reaction volume of 50 mM Tris pH 7.8 with 65 mM MgCl, 0.38 mM $NADP^+$ in the presence of cell lysate or recombinant G6PD without G6P as the main substrate.

3.13 Glutathione (GSH) and oxidized glutathione (GSSG) measurement

A549 cells were seeded at 10^5 cells per ml in opaque 96-well plates. Cells were treated with Octyl Ita (250 µM) for 6 hours. The cell supernatant was then removed and the ratio of reduced glutathione (GSH) to oxidized glutathione (GSSG) was quantified using the Promega GSH/GSSG-Glo assay (V6611, Promega, USA) according to the manufacturer's instructions. Luminescence was quantified using a Tecan microplate reader (infinite M200 PRO, Tecan Group, Maennedorf, Switzerland).

3.14 In silico analysis of G6PD activity

3.14.1 Ligand Preparation

All the Itaconic derivatives were prepared using the Marvin sketch, and all the molecules were saved as .MOL file and will be subjected to molecular docking analysis. All the molecules were subjected to energy minimization using PyRx to complete the normalization process and background corrections. These were analyzed using Marvin view which is an advanced chemical viewer for 2D or 3D structures of chemicals and their related information. Following this, using Biovia Discovery software the selected ligands were converted into the 3D structure for further use.

3.14.2 Protein preparation

The three-dimensional structure of the G6PD dehydrogenase was retrieved from the PDB databank (PDB ID: 2BHL), solved by the XRAY diffraction method, with a resolution of 5.00A against our selected lawsone derivatives. Before docking, polar hydrogens were added to the retrieved protein structure using the Discovery Studio Visualizer.

3.14.3 Molecular Docking Analysis

The G6PD protein's active site contained β-D Glucopyranose-6-Phosphate as the natural or reference ligand. For docking analyses, we employed the AutoDock vina software, a widely used molecular docking program known for its accuracy and efficiency. This program is a turnkey computational docking program that is based on a simple scoring function and rapid gradient-optimization conformational search. The hydrogen bonding interactions of itaconate in the active site of G6PD and docking scores (ΔG; kcal/mol) were determined.

3.15 Tumor Precision Cut Lung Slice (tPCLS)

3.15.1 Preparation of tPCLS from human lung cancer patients

To prepare tumor precision cut lung slices (tPCLS), freshly resected human lung lobes with lung tumors were first infused in surgery or pathology via an accessible bronchus/artery with a solution of 1% low-melting agarose (A9414, Sigma, USA) in DMEM/F12 medium without any additives (Karger, Mansouri et al. 2023). All lung tissues used were from the Lung Center of the Universities of Giessen and Marburg (UGMLC). The research with these tissues was ethically approved by the Ethics Committee under file number AZ 58/15. After inflating the entire lobe and closing the entry site, the lobe was placed on ice to facilitate cooling and solidification of the agarose. The filled lung flap was then cut into smaller pieces and embedded in 4% agarose in 1x PBS. These sections were then finely cut into 300–400 µm thick slices using a VT1200S vibratome (Leica, Wetzlar, Germany). The resulting slices were cultured in PCLS culture medium

consisting of DMEM F12 with 10% FCS, 1% P/S and 0.1% amphotericin and used for subsequent experiments (Karger, Mansouri et al. 2023).

3.15.2 Proliferation and apoptosis measurement in tPCLS

To assess proliferation, 20 µM 5-ethynyl-2'-deoxyuridine (EdU) was added to the tPCLS and incubated overnight in the cell incubator. EdU, a thymidine nucleoside analog, is integrated into the DNA during replication. After this incubation period, the tPCLS were fixed overnight at 4°C in 1% paraformaldehyde (PFA). They were then permeabilized with 0.3% Triton X-100 in PBS for 30 minutes at room temperature. To visualize the incorporated EdU, staining was performed according to the instructions in the Click-iT™ EdU Cell Proliferation Kit (C10337, ThermoFisher Scientific, USA). To identify apoptotic cells, we used the in situ cell death detection kit from Roche (Basel, Switzerland) according to the manufacturer's instructions. The stained cells were then imaged using Leica SP8 confocal microscopy.

3.16 Histological procedure

3.16.1 Haematoxylin & Eosin (H&E) staining

Hematoxylin and Eosin (H&E) staining involve two distinct chemicals in their process. Hematoxylin is responsible for staining cell nuclei a dark purple color, while Eosin is used to stain the cytoplasm and extracellular matrix in varying shades of pink. For H&E staining of cryosections, the tissue sections were thawed at room temperature for 10 minutes. Then, they were fixed in a solution of Aceton/Methanol (1:1) at -20°C for 20 minutes. After an additional 10 minutes at room temperature, the slides were rinsed 5 minutes in distilled water. After that, the sections were stained with Hematoxylin (Mayer) for 20 minutes followed by washing with flowing water for further 5 minutes. Then the slides were submerged in Ethanol (96%) for 1 minute which continued by Eosin staining for 4 minutes and then rinsed with water followed by dipping twice for 2 minutes each in Ethanol (96%) for dehydration. After, the slides were placed in Xylol three times for 5 minutes each. Finally, the slides were mounted with coverslips using Entellan mounting medium from Merck Millipore in Germany.

3.16.2 Immunofluorescence staining

To perform immunofluorescence (IF) staining, we used frozen tissue sections and fresh tPCLS. In the first step, the tissue sections were fixed by treatment with 4% PFA for 10 minutes at room temperature. For the tPCLS, however, we fixed them overnight at 4°C with 1% PFA. After fixation, the tissue sections and tPCLS were washed three times in succession with 1x PBS for 5 minutes each on a shaker. They were then treated with 0.3% Triton X-100 in PBS for 10 minutes (for tissue sections) or 30 minutes (for tPCLS)

at room temperature and permeabilized. This step was followed by blocking with 5% BSA in PBS for 1 hour at room temperature. In the next step, the primary antibody (diluted in 1% BSA/PBS) was added to the tissues, followed by overnight incubation at 4°C. This was followed by three thorough washes with 1x PBS on a shaker. A secondary fluorochrome-conjugated antibody (in 1% BSA/PBS) was then applied and incubated for 1 hour at room temperature, followed by three more washes with 1x PBS on a shaker. Finally, tissue sections were mounted with DAPI-containing medium and stored at 4°C until imaging. In the case of tPCLS, DAPI staining was performed separately for 15 minutes at room temperature with DAPI (10 mg/ml; Invivogen, USA) at a dilution of 1:500 in 1x PBS. After washing twice with 1x PBS, the tPCLS were stored in 1x PBS at 4°C until imaging. It should be noted that for each immunofluorescence staining procedure, we used isotype-specific immunoglobulins at a protein concentration corresponding to that of the primary antibody as a negative control.

For the IF staining of mouse lung tumors, we adopted a random sampling approach when collecting images from each individual mouse. To ensure statistical robustness, we included a minimum of three mice in each experimental group. The criteria for this random selection process were based on the number of tumor nodules observed within the entire lung section.

3.17 Animal experiments

All mice including C57Bl/6J, *Irg1*$^{-/-}$ and *Kras*^{LA2} transgenic (Kras) mice were kept under specific pathogen-free conditions and handled according to the European Union Commission guidelines for laboratory animals. The animal experiments conducted as part of this research were approved by the local authorities (Regierungspraesidium Darmstadt, Hessen, Germany, animal proposal: B2-2000). For our experiments, we used C57BL/6 and *Irg1*$^{-/-}$ mice aged 7 to 8 weeks and Kras mice aged 3 to 5 months. Kras mice develop alveolar adenomatous hyperplasia 1 week after birth (Johnson, Mercer et al. 2001). Kras mice harbor two copies of *Kras* exon 1 containing an activating mutation where glycine is substituted with aspartic acid at codon 12 (p.G12D). In the absence of intrachromosomal recombination, this particular allele fails to generate any protein, resulting in the demise of homozygous mutants during embryogenesis. In heterozygous individuals, intrachromosomal recombination events consistently give rise to an active p.G12D allele. Expression of the G12D protein initiates the formation of lung tumors (Johnson, Mercer et al. 2001). These mice were obtained from Charles River Laboratories.

To obtain Kras/*Irg1*$^{-/-}$ mice, we first crossbred heterozygous Kras (*Kras*$^{+/-}$) mice with homozygous *Irg1* (*Irg1*$^{-/-}$). In the first generation, *Kras*$^{+/-}$/*Irg1*$^{-/+}$ offspring were crossbred with *Irg1*$^{-/-}$ littermate to achieve *Kras*$^{+/-}$/ *Irg1*$^{-/-}$ mice in the second generation. We used the latter one in further experimental setups in this thesis.

3.17.1 Genotyping

Genomic DNA was isolated from ear punches by lysating them in a Tris-EDTA Buffer pH 8, containing 0.5% SDS and 20mg/ml Proteinase K at 56°C for minimum 6 hours. After centrifugation, the supernatant containing genomic DNA was diluted and subjected to PCR. All genotyping PCR reactions were performed using KAPA2G Fast ReadyMix (2GFRMKB, Sigma, USA) as shown in Table 3-7.

Table 3-7. Master mixture material for genotyping PCR

Reagent	Volume [µl]
H_2O	6
KAPA2G Fast ReadyMix	12
$MgCl_2$	0.5
Primer 1	1.25
Primer 2	1.25
Primer 3	1.25
DMSO	1.25
Template	1

The primers and PCR reaction program which used for Kras mice are depicted in Table 3-8 and Table 3-9.

Table 3-8. Genotyping primer list and PCR product for Kras mice. (1-2 and 4) wild type, (3 and 5) heterozygous mice (Kras$^{+/-}$), (n) negative control and (L) ladder.

Primer	Sequence 5' --> 3'
Kras^{LA2} wild type-Forward	TGCACAGCTTAGTGAGACCC
Kras^{LA2} wild type-Reverse	GACTGCTCTCTTTCACCTCC
Kras^{LA2} mutant-Reverse	GGAGCAAAGCTGCTATTGGC

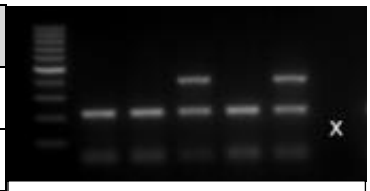

(L) (1) (2) (3) (4) (5) (n)

Table 3-9. PCR reaction for Kras mice

Temperature	Time	Cycle
95°C	3 minutes	1
95°C	30 seconds	
64°C	1 minuntes	35
72°C	1 minutes	
72°C	2 minutes	1
4°C	∞	1

The primers and PCR reaction program which used for *Irg1*$^{-/-}$ mice are depicted in Table 3-10 and Table 3-11.

Table 3-10. Genotyping primer list and PCR product for *Irg1*$^{-/-}$ mice. (1-4) knockout (*Irg1*$^{-/-}$), (5) wild type, (n) negative control and (L) ladder.

Primer	Sequence 5' --> 3'
Irg1 wild type -Forward	GTGGGGAGGGGAACTATGAG
Irg1 wild type-Reverse	ATTTGGAGGAACCCCATGAC
Irg1 mutant-Reverse	CAGCCTCTAAGCCAGACAGC

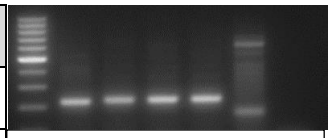

(L) (1) (2) (3) (4) (5) (n)

Table 3-11. PCR reaction for *Irg1*$^{-/-}$ mice

Temperature	Time	Cycle
95°C	5 minutes	1
95°C	20 seconds	
64°C	30 seconds	35
72°C	15 seconds	
72°C	10 minutes	1
4°C	∞	1

3.17.2 Tumor cell injection

For the subcutaneous (SC) tumor model, the animals are anesthetized using isoflurane (1.5-2.0% (v/v) in 0.5 l/min of air and 0.5 l/min of oxygen) to ensure precise injection. The animals receive an injection of 10^6 LLC1 tumor cells in 100µl of isotonic saline solution subcutaneously under the skin on their backs using a fine needle. Tumor measurements were conducted every 4 days using an external digital caliper to assess both the greatest longitudinal diameter (length) and the greatest transverse diameter (width). The tumor volume was then calculated using the modified ellipsoidal formula: tumor volume (mm^3)

= 0.5 × length × width². On the 16th day following the implantation of tumor cells, mice were euthanized, and both lung tissue and SC tumors were collected, photographed and fixed in 4% PFA for immunohistochemistry. Some parts were frozen for enzyme activity analysis, while others were used for FACS analysis.

For the intravenous injection model, 10^6 LLC1 tumor cells were injected in a total volume of 100µl, using a fine needle, into the lateral tail vein of C57BL/6 or *Irg1*$^{-/-}$ mice. To ensure optimal administration, the animals are gently restrained (mouse box with an opening for the tail). After the injection, the needle is removed, and slight pressure is applied to the injection site until any potential bleeding stops. If necessary, tissue adhesive may be used. All mice were closely monitored for the following 17 days. One day prior to sacrifice, mice underwent µCT imaging. After reaching the predetermined humane endpoints, the mice were sacrificed and their lungs were removed after perfusion. The lungs were photographed and the macroscopic nodules were quantified. Lung tissue was fixed in 4% PFA for immunohistochemistry and a portion was used for FACS analysis.

To investigate the effect of Octyl Ita on the growth of SC and lung tumors, we first dissolved Octyl Ita in 2-hydroxypropyl-beta-cyclodextrin (H107, Sigma, USA) and then administered it intraperitoneally at a dose of 100mg/kg every other day for 10 days, starting 4 days after tumor induction in both SC and tail vain injected models. The placebo group received 2-hydroxypropyl-beta-cyclodextrin in the same way as the Octyl Ita group. In the SC model, tumor growth was measured every 4 days using a digital caliper. On day 16 and day 17 of SC and tail vain injected models, respectively, the mice were euthanized and their tumors were harvested, photographed and fixed in 4% PFA for immunohistochemistry. Some parts were frozen for enzyme activity analysis, while others were used for FACS analysis.

3.17.3 Bone marrow transplantation

The recipient mic were irradiated firstly once using the RS-2000 Biological Irradiator, Rad Source Technologies, Inc., Alpharetta, GA, USA. The radiation dose is calculated for the cage area (Special Cage Irradiator), ensuring that the dose is 19.5 mGray/sec or 1.17 Gy/min throughout the cage. The animals are irradiated for 483 seconds, resulting in a total dose of 9.5 Gy. After irradiation, the C57BL/6 recipient mice receive an intravenous transfer of 1.5-2x10^7 bone marrow cells from the *Irg1*$^{-/-}$ donor mice. For this purpose, the donor mice were injected intraperitoneally with 500 units of heparin and anesthetized with a lethal dose of ketamine and xylazine at a ratio of 1:1:2. Muscle tissue was removed from the femurs and the bone marrow cells were flushed with RPMI 1640 culture medium containing 1% P/S. After centrifugation, the cells were resuspended in fresh medium,

filtered through a cell strainer with a pore size of 40µm, counted and then transplanted into irradiated acceptor mice (3×10^6 cells/100µl NaCl per mouse were injected intravenously). For this, the recipient mice were immobilized in a prone position in a mouse box (black box with an opening for the tail), and a maximum of 200µL of cell suspension (cells in NaCl) was injected into the tail vein of C57BL/6 recipient mice, which has been pre-warmed using a red light lamp. The animals' immune systems can now begin to reconstitute. The bone marrow reconstitution takes place within 21 days, and we allow the animals to rest for an additional 10 days before injecting the tumor cells. The weight of the mice was monitored until they reached the same weight as before bone marrow transplantation. Thereafter, 10^6 LLC1 cells were injected into the tail of the bone marrow transplanted mice. On day 18, the mice were euthanized and their tumors were harvested as described in section 3.17.3.

3.17.4 µCT measurement

For µ-CT measurements, the animals to be examined are immobilized under isoflurane anesthesia (1.5-2.0% (v/v) in 0.5 l/min air and 0.5 l/min oxygen) and positioned comfortably in a pre-made measurement bed to ensure painlessness. Monitoring of the animal during the µCT measurement is carried out through the integrated physiological monitoring subsystem. The µCT device (Bruker Skyscan 1276) has been specifically designed for in vivo measurements of small animals and stands out due to its exceptionally short scanning time with low radiation exposure (maximum 1 Gy with three measurements). If necessary, the administration of a contrast agent is done intraperitoneally or intravenously into the tail vein of mice. The choice of contrast agent is made separately based on the specific research question, following the manufacturer's recommendations, and taking into account the maximum recommended dose of GV-Solas. After the measurement, the animals are returned to their cages and wake up immediately. The obtained images were used to assess the lung tumor burden by thickness histogram analysis which relies on analyzing the thickness histogram of soft tissue structures within the lungs. This analysis involves comparing the lung tissues of control mice with those affected by tumors, ensuring that the mice in the study are comparable.

3.18 Statistical analysis

Statistical analysis was performed using Prism 8 software (GraphPad Software Inc., San Diego, USA). Student’s t-test (two-tailed) was used to compare two groups. If there were more than two groups, the differences between the groups were determined using a one-way ANOVA Tukey’s multiple comparison test for unpaired non-parametric variables. The data are given as mean ± s.e.m.; statistical significance was set at $p\leq0.05$.

4 Results

4.1 Irg1 ablation exacerbates lung tumor growth *in vivo*

4.1.1 Irg1 deficient mice reveals enhancement of lung tumor growth

To investigate the functional role of Irg1 in lung tumorigenesis, we studied the growth and metastasis of lung tumors in two lung tumor models of mice; first, in Kras/*Irg1*$^{-/-}$ mice. To obtain this mouse strain, we crossed Kras with *Irg1*$^{-/-}$ mice. It should be mentioned that the Kras mouse model represents a spontaneous somatic activation of the latent *Kras*^{LA2} allele leading to alveolar adenomatous hyperplasia 1 week after birth. After establishing the double transgenic line of Kras/*Irg1*$^{-/-}$ mice, we examined lung tumor development in mice at 3 months of age. In the second lung tumor model, we used an orthotopic lung tumor model in which LLC1 cells were injected intravenously into both *Irg1*$^{-/-}$ and wild type (WT) littermate mice. In this model, lung tumor progression was monitored between 17 and 18 days after LLC1 injection. Analysis of tumor nodules and µCT images of the lung showed that depletion of Irg1 exacerbated lung tumor growth and metastasis not only in Kras/*Irg1*$^{-/-}$ mice, but also in the orthotopic model in *Irg1*$^{-/-}$ mice compared to WT littermates (Figure 4-1, A-C). These data suggest an anti-tumor function of Irg1 during lung tumorigenesis.

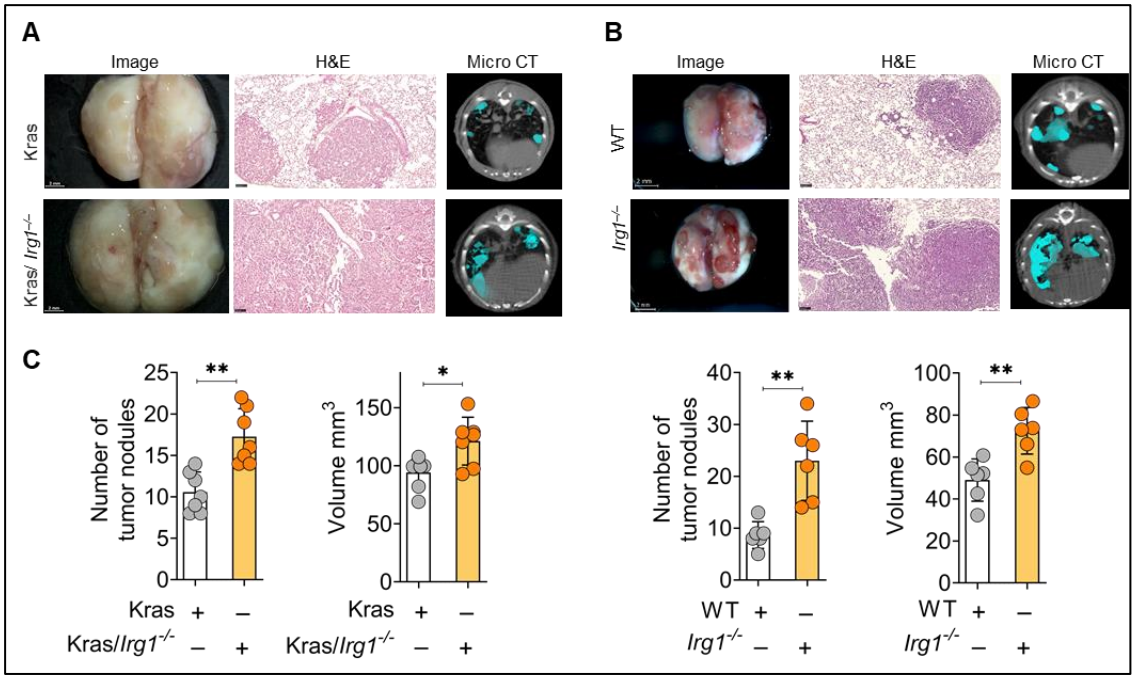

Figure 4-1 Loss of Irg1 accelerates the lung tumor growth and metastasis. (**A-B**) Representative images of extracted lungs (scale bars: 2 mm), H&E-stained lung sections (scale bars: 100 µm) and µCT from (**A**) Kras and Kras/*Irg1*$^{-/-}$ mice and (**B**) wild type (WT) and *Irg1*$^{-/-}$ mice which are inoculated with LLC1 cells intravenously for lung tumor induction. (**C**) Quantification of lung tumor nodules that are counted microscopically and lung intensity of µCT images (n=7 mice for Kras and Kras/*Irg1*$^{-/-}$ model, left panels and n=6 mice for WT and *Irg1*$^{-/-}$ model, right panels).

The data represent the mean ± s.e.m. Statistical significance was assessed by a two-tailed unpaired Student's *t*-test. *p <0.05, **p <0.01.

4.1.2 Irg1 ablation induces proliferation rate without effects on apoptosis in lung tumors

Consistent with tumor number and tumor volume, IF staining of lung sections to determine proliferation and apoptosis markers, proliferating cell nuclear antigen (PCNA) and caspase 8, revealed that the absence of Irg1 resulted in a significant increase in overall lung tumor proliferation compared to the control group. Importantly, this change does not appear to have a significant effect on the apoptosis rate (Figure 4-2, A-B).

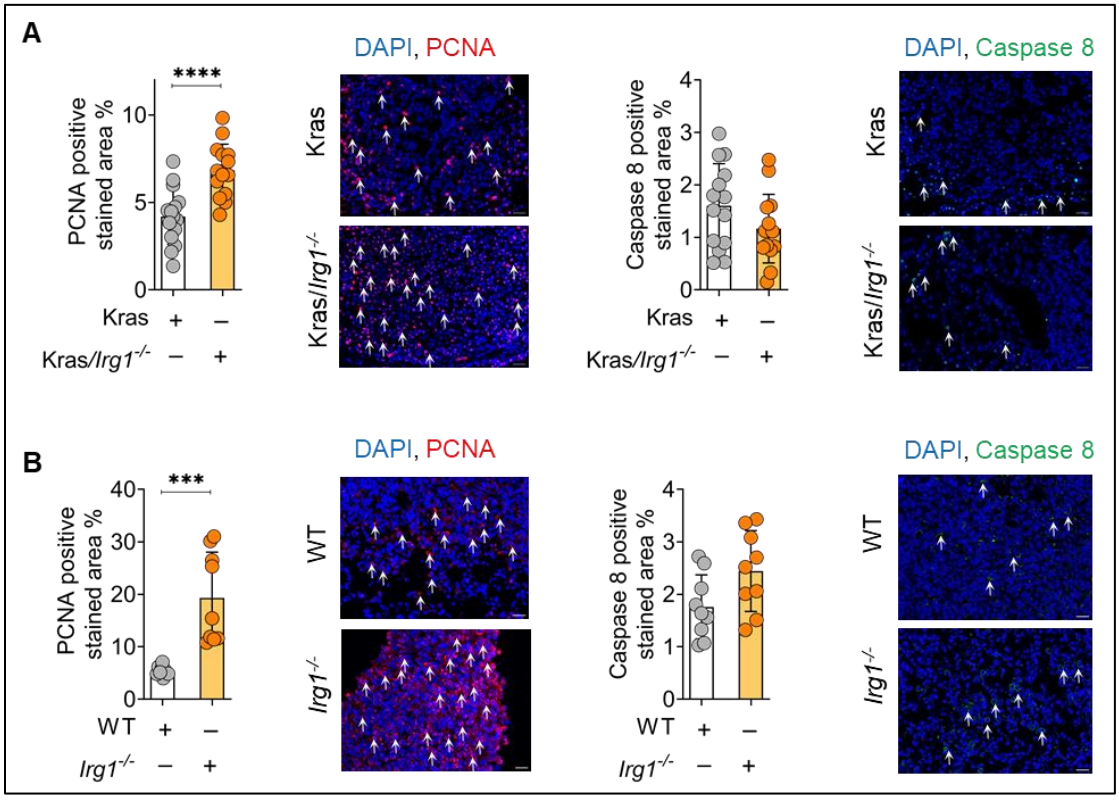

Figure 4-2. Loss of Irg1 induces proliferation rate without effects on apoptosis in lung tumors. (**A-B**) Quantification and representative images of immunofluorescence staining for PCNA as a proliferation marker (red), caspase 8 as an apoptosis marker (green) and cell nuclei (blue) in lung tumor sections (**A**) Kras and Kras/*Irg1*$^{-/-}$ mice (n=15) and (**B**) WT and *Irg1*$^{-/-}$ mice (n=9). Scale bar=100µm. Data represent the mean ± s.e.m. Statistical significance was determined using a two-tailed, unpaired Student's t-test. ***p < 0.001, ****p < 0.0001.

In the next step, we wanted to identify the specific cell type within the lung tumor TME that is responsible for Irg1 expression. To do this, we used our previously published scRNA-seq dataset of immune cells isolated from lung tumors in Kras mice and mice injected with LLC1 cells (Weigert, Zheng et al. 2022). Re-analysis of the data revealed

that the expression of *Irg1* was significantly enriched within the Mϕ cluster among all CD45^{+} immune cells in the lung TME (Figure 4-3).

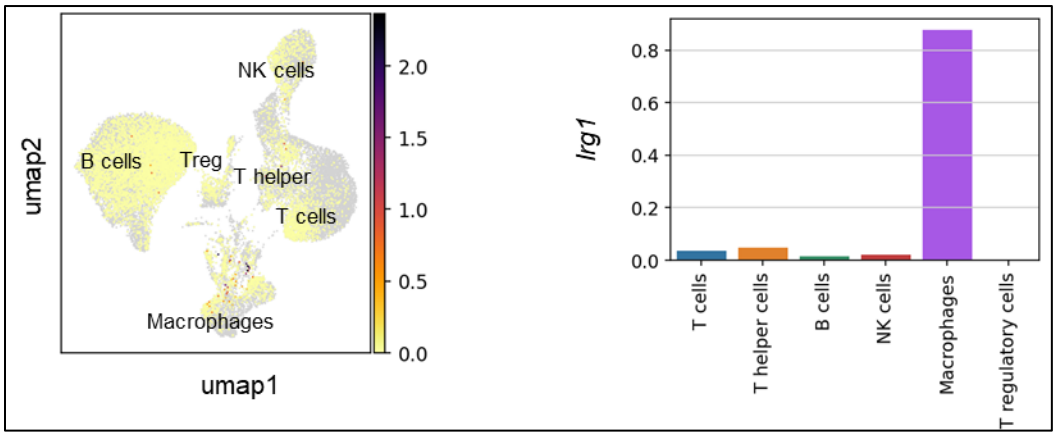

Figure 4-3. Irg1 cell specific profile in mouse lung tumors. Uniform manifold approximation and projection (UMAP) representation from scRNA-seq CD45^{+} cells of LLC1 mice lung tumor which are clustered by the Leiden algorithm revealing 6 clusters (left). Distribution of *Irg1* expression in all CD45^{+} clusters is shown in right panel.

Our study went beyond mouse models and also included publicly available scRNA-seq data on human lung cancer (Kim, Kim et al. 2020). This analysis confirmed that myeloid cells are the primary cell population responsible for *IRG1* expression among all other immune cells, epithelial and malignant cells as it depicted in uniform manifold approximation and projection (UMAP) graph (Figure 4-4A), although not many myeloid cells were positive for *IRG1* which is similar to mouse lung tumors. Furthermore, Mϕ population including alveolar Mϕ, monocyte, pleural Mϕ and monocyte-derived Mϕ (monocyte- Mϕ) are exhibited the highest level of IRG1 expression among all myeloid cell types (Figure 4-4B). Next, we asked which tissue is more responsible for *IRG1* expression in Mϕ. Interestingly, the tissue-specific IRG1 expression profile showed that normal lung tissue had higher *IRG1* expression compared to other tissues, including tumor tissue (Figure 4-4C). To further confirm these findings, we examined *IRG1* mRNA expression in Mϕ isolated from human lung tumors and adjacent normal tissues. The results were consistent with our previous observations as MACS-sorted TAMs showed significantly lower *IRG1* mRNA expression compared to Mϕ isolated from normal tissue (Figure 4-4D).

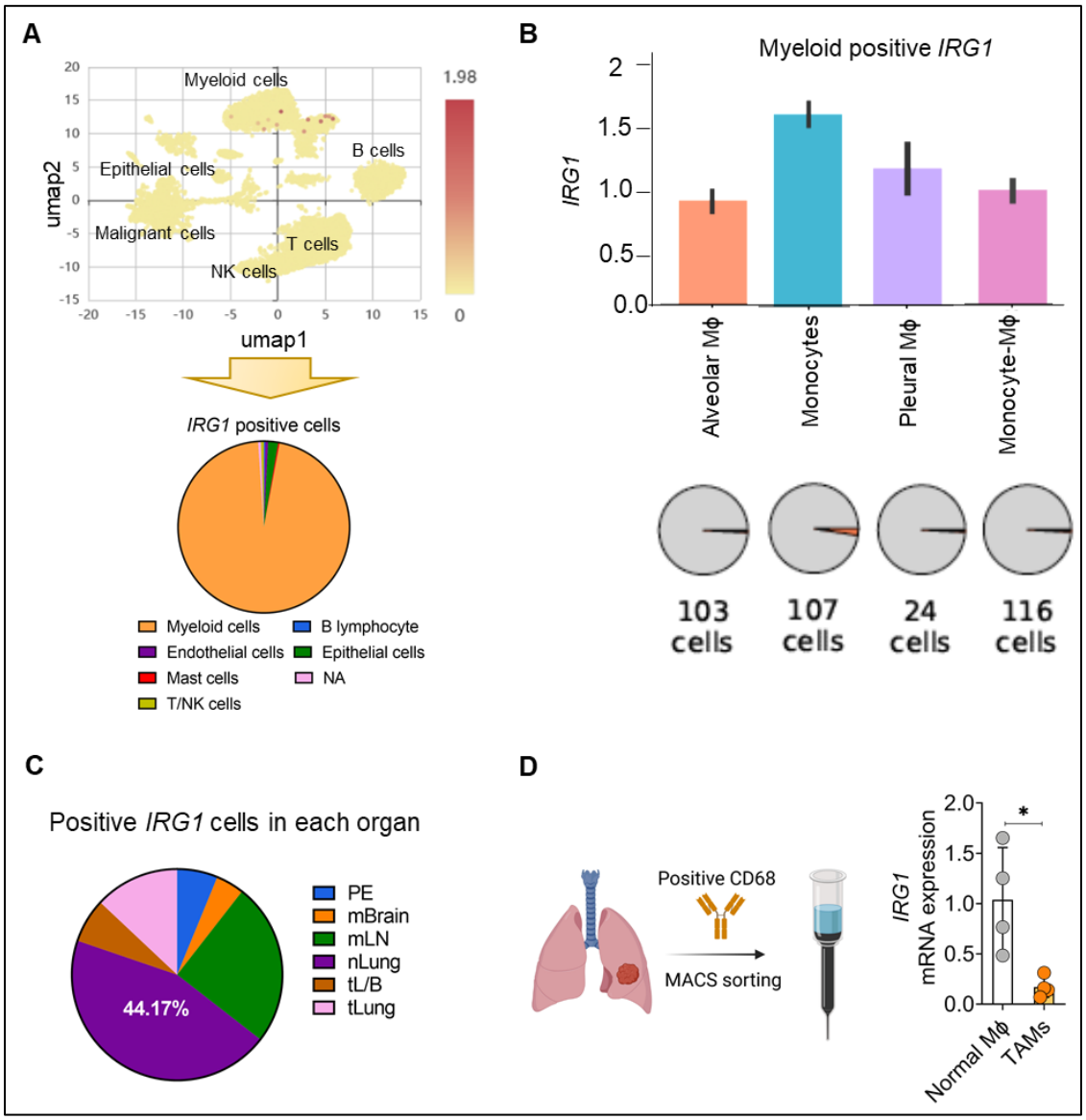

Figure 4-4. IRG1 cell specific profile in human lung tumors. (**A**) UMAP representation from public available scRNA-seq of human metastatic lung adenocarcinoma https://immucanscdb.vital-it.ch/LUAD_UNB_10X_GSE131907 in which *IRG1*⁺ cells are depicted mainly in myeloid cluster followed by distribution of *IRG1*⁺ cells in various cell types (lower panel). (**B**) Distribution of *IRG1*⁺ cells in myeloid cell population in human metastatic lung adenocarcinoma. (**C**) Distribution of *IRG1*⁺ cells by tissue origin in human metastatic lung adenocarcinomas; pleural fluid (PE), brain metastases (mBrain), lymph node metastases (mLN), normal tissue from lung (nLung) and lymph node (nLN), early and advanced stage lung tumors (tLung and tL/B, respectively). (**D**) mRNA expression of *IRG1* in human normal Mϕ and TAMs isolated from normal lung tissue and tumor tissue, respectively, using CD68 antibody-linked magnetic beads (n=4). Data represent the mean ± s.e.m. Statistical significance was determined using a two-tailed unpaired Student's t-test. *p < 0.05.

Next, we asked about differentially expressed genes (DEGs) between IRG1⁺ and IRG1⁻ Mϕ in scRNA-seq data related to human lung cancer (Kim, Kim et al. 2020). This analysis

uncovered an intriguing pattern. Approximately 40% of the upregulated DEGs in IRG1^{+} Mϕ were associated with anti-tumor Mϕ markers for example CXCL8, CXCL2, NAMPT, SAT1 etc. (Karger, Mansouri et al. 2023), while only 10% were related to pro-tumor Mϕ markers for example TGFBI and TIMP2 (Figure 4-5). This pattern strongly suggests the prevalence of an anti-tumor phenotype within IRG1^{+} TAMs. These data indicate that Mϕ are the major contributors to Irg1/IRG1 expression in the lung TME. These Mϕ exhibit properties associated with an anti-tumor phenotype, further highlighting the potential importance of IRG1/itaconate in modulating the immune response against lung tumors.

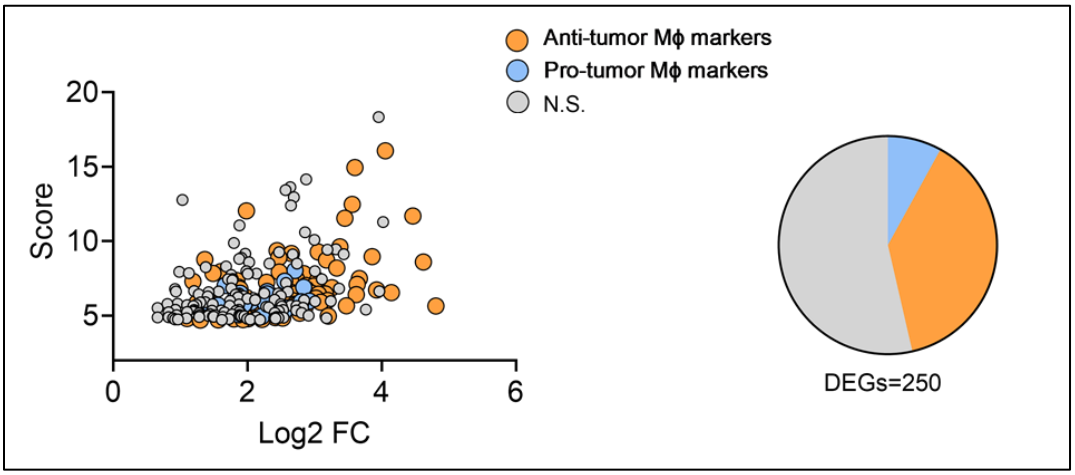

Figure 4-5. Transcriptomic analysis between IRG1+ and IRG1- Mϕ population in human lung tumors. Top 250 differentially expressed genes (DEGs) between IRG1^{+} and IRG1^{-} Mϕ populations in human lung tumors from Figure 4-4A, which are classified based on anti-tumor and pro-tumor Mϕ markers. N.S.=non significant.

In the same line, TAMs isolated from Kras/*Irg1*$^{-/-}$ and *Irg1*$^{-/-}$ lung tumors exhibited a more pronounced pro-tumor phenotype than TAMs from Kras and WT lung tumors, respectively, as indicated by the lower expression of CD80 (as an anti-tumor marker) and the high expression of CD206 (as a pro-tumor marker) (Figure 4-6, A-B).

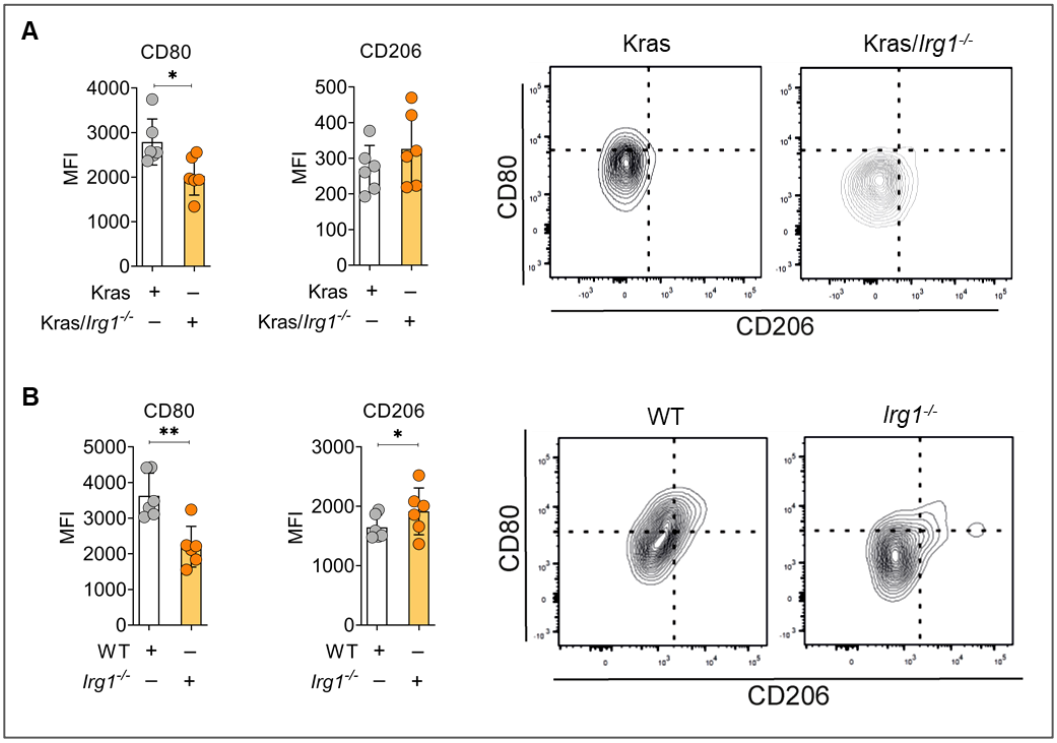

Figure 4-6. Characteristic phenotype of TAMs isolated from mouse lung tumors. (A-B) Mean fluorescence intensity (MFI) of CD80 and CD206 analyzed by FACS on Mϕ in the lungs of (**A**) Kras and Kras/*Irg1*$^{-/-}$ and (**B**) WT and *Irg1*$^{-/-}$ mice inoculated intravenously with LLC1 cells (n=6 mice for each model). Data represent the mean ± s.e.m. Statistical significance was determined using a two-tailed unpaired Student's t-test. *$p < 0.05$, **$p < 0.01$.

Overall, our results show that Irg1 plays a role in the suppression of lung tumor growth and metastasis. Moreover, Irg1 expression is associated with an anti-tumor phenotype in Mϕ, which may be the primary immune cells responsible for Irg1 expression in lung TME.

4.1.3 Loss of Irg1 in bone marrow cells exacerbates lung tumor formation

To investigate the involvement of Irg1-expressing Mϕ in lung tumorigenesis, we performed bone marrow (BM) transplantation experiments. In these experiments, BM cells from *Irg1*$^{-/-}$ and WT littermates were transplanted into irradiated WT mice. Subsequently, lung tumors were induced in these mice by intravenous injection of LLC1 tumor cells. The absence of Irg1 in the BM cells led to an increase in lung tumor growth and metastasis, as shown in Figure 4-7.

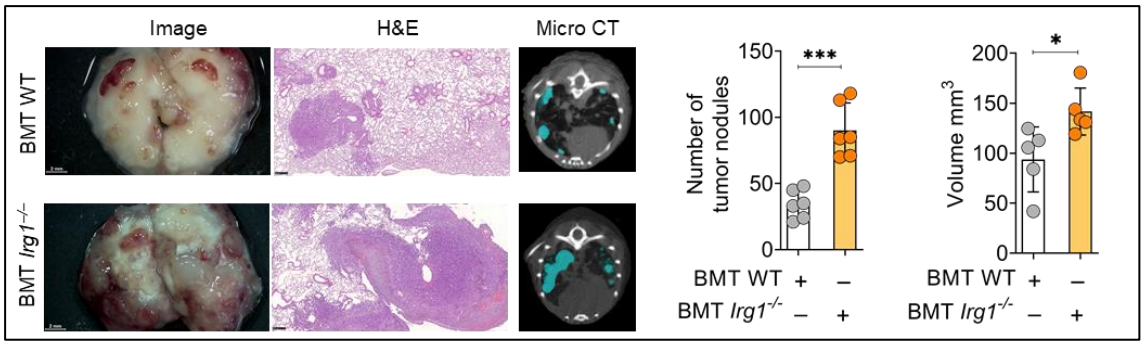

Figure 4-7. Loss of Irg1 in bone marrow cells accelerates the growth of lung tumors. Representative images of harvested lungs (scale: 2 mm), H&E-stained lung sections (scale: 100 μm), and micro-CT of WT mice that first underwent bone marrow transplantation (BMT) of WT or *Irg1*$^{-/-}$ BM and were then injected with LLC1 cells via the tail for lung tumor induction. Quantification of lung tumor nodules counted microscopically (n=6 mice for each group) and lung intensity of μCT images (n=5 mice for each group) (right panel). Statistical significance was determined using a two-tailed unpaired Student's t-test. *$p < 0.05$, ***$p < 0.001$.

In addition, we detected increased PCNA expression in the lung tumors as a marker of proliferation and a reduction in apoptosis as evidenced by decreased caspase-8 expression (Figure 4-8A), supporting the anti-tumor functions of Irg1-expressing Mϕ during lung tumorigenesis.

We also examined the phenotype of Mϕ, an important immune cell population known to express Irg1 in lung tumors. Consistent with the results from Kras/*Irg1*$^{-/-}$ and *Irg1*$^{-/-}$ mice, we detected a pro-tumor phenotype in Mϕ from tumors transplanted with *Irg1*$^{-/-}$ cells from BM. This pro-tumor phenotype was characterized by decreased expression of CD80, as shown in Figure 4-9B. These results highlight the protective role of Irg1-positive Mϕ within the lung TME in attenuating tumor progression.

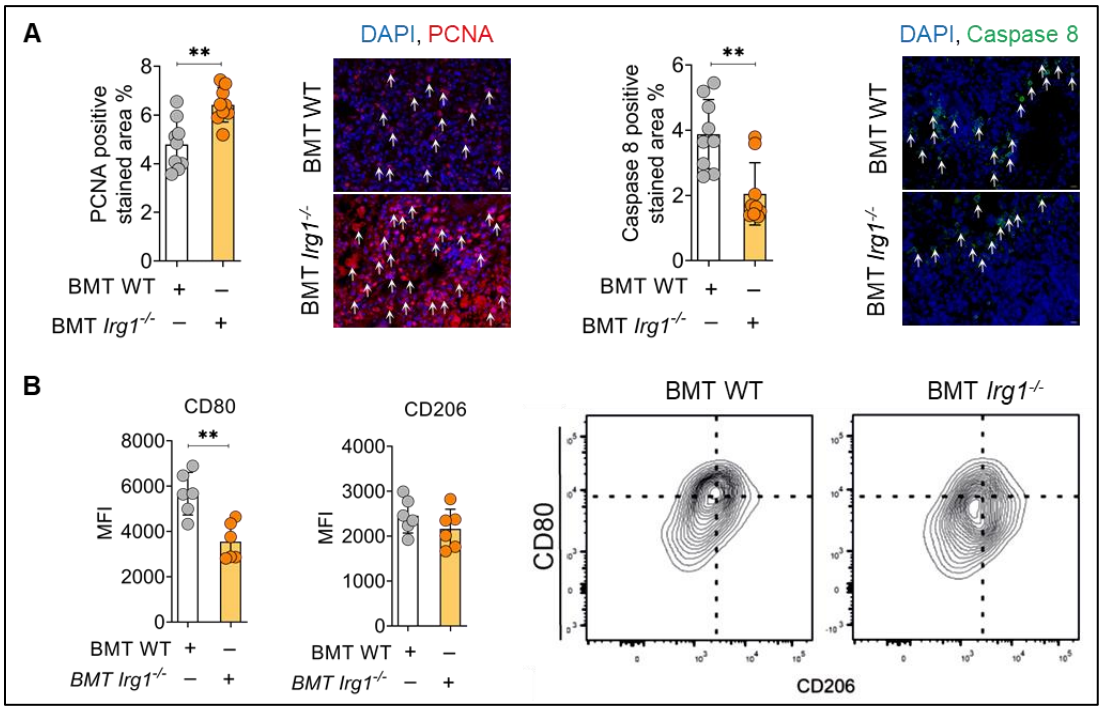

Figure 4-8. Loss of Irg1 in Mϕ induces proliferation rate and reduces apoptosis in lung tumors. (**A**) Quantification with representative images of immunofluorescence staining for PCNA as a proliferation marker (red), caspase 8 as an apoptosis marker (green) and nuclei (blue) in lung tumor sections (n=9). Scale bar=100µm. (**B**) Mean florescence intensity (MFI) of CD80 and CD206 analysed by FACS on Mϕ in the lungs of BMT WT with WT or *Irg1*$^{-/-}$ BM after injection of LLC1 cells into the tail (n = 6 mice for each group). Data represent the mean ± s.e.m. Statistical significance was determined by a two-tailed unpaired Student's t-test. *p < 0.05, **p < 0.01.

To further investigate the proteomic profile of lung tumors without Irg1, we used the Olink® exploration kit (Olink®, Sweden), which captures a variety of inflammation-associated proteins such as cytokines, chemokines and cancer-associated proteins. Interestingly, we detected higher levels of pro-tumor proteins in Kras/*Irg1*$^{-/-}$ lung tumors, including CXCL 1, aryl hydrocarbon receptor (AHR) and subunit B of platelet-derived growth factor (PDGFB), CCL2, CCL3 and CXCL1 in orthotopic *Irg1*$^{-/-}$-LLC1 lung tumors and colony-stimulating factor (CSF) 2, CCL3 and CXCL1 in Irg1$^{-/-}$-BM-transplanted lung tumors compared to WT counterparts (Figure 4-9).

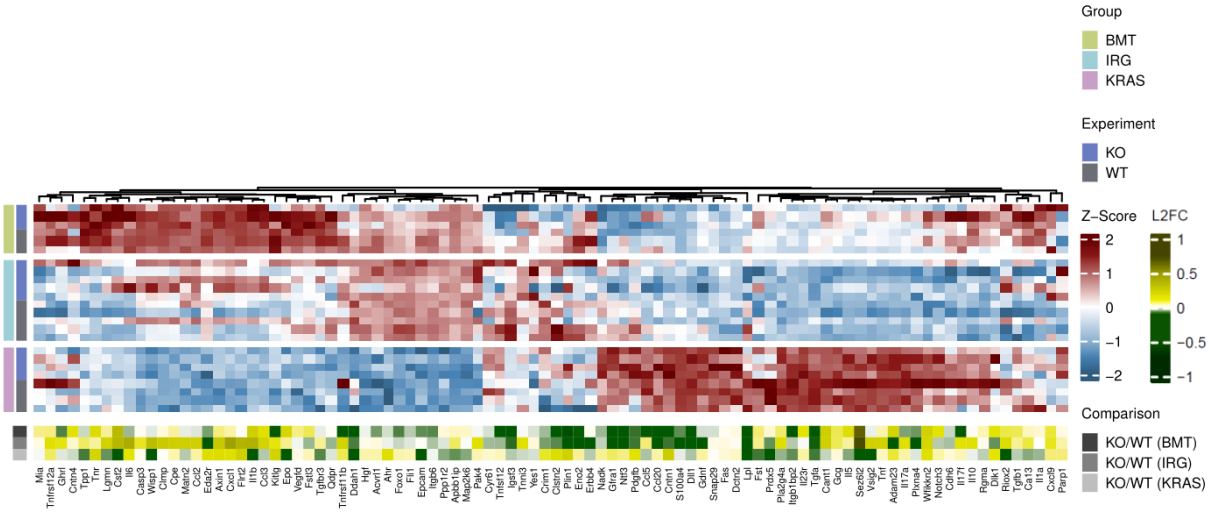

Figure 4-9. Proteome analysis for mouse lung tumor tissue. Heatmap of Olink® Target 96 mouse exploratory kit from lung tumor of Kras and Kras/*Irg1*$^{-/-}$ mice (light purple, n=4), WT and *Irg1*$^{-/-}$ mice (light blue, n=4), BMT WT and BMT *Irg1*$^{-/-}$ (green, n=3 mice). Blue and gray are used to indicate KO and WT mice in each comparison in Z-Score heatmap (upper one). The lower heatmap indicates the comparison of mean log 2 fold change (L2FC) in each three group. AbbreviationsBMT: bone morrow transplantation, KO: knock-out Irg1 mice, WT: wild-type mice.

Overall, these results support the idea that Irg1 plays a key protective role in inhibiting the growth and metastasis of lung tumors. Importantly, they also shed light on the central role that immune cells, particularly Mϕ, play in mediating the effects of Irg1 on lung tumorigenesis. This highlights the interplay between Irg1^{+} Mϕ and cancer cells during lung tumorigenesis.

4.2. 4-Octyl Itaconate reduces lung tumor growth and metastasis

4.2.1 4-Octyl Itaconate effects on mouse lung tumor progression and metastasis

Itaconate is currently recognized as the primary and exclusive product resulting from the activity of Irg1 (Michelucci, Cordes et al. 2013). To validate the anti-tumor capabilities of Irg1, we conducted thorough assessments of the effects of itaconate on the development of lung tumors, both *in vivo* and *ex vivo*, as well as *in vitro* experiments. For these investigations, we utilized a cell-permeable derivative of itaconate known as 4-Octyl Itaconate (Octyl Ita) (Mills, Ryan et al. 2018). Remarkably, Octyl Ita showed a considerable inhibitory effect on the growth and metastasis of lung tumors in mice harboring lung tumors (Figure 4-10A), highlighting the protective role of Irg1 in the context of lung tumor development, possibly due to the production of itaconate. In the same line, treatment with Octyl Ita resulted in significantly decreased PCNA expression, indicating a reduced proliferation rate in lung tumors. However, no discernible effect on the apoptosis rate was observed (Figure 4-10B). Regarding the Mϕ phenotype in lung

tumors after Octyl Ita treatment, we found that Octyl Ita reduced the pro-tumor phenotype of TAMs, as evidenced by a decrease in CD206 expression (Figure 4-10C). These observations are consistent with the previous identification of Irg1-null lung tumors that exhibit Mϕ with pro-tumor phenotypes.

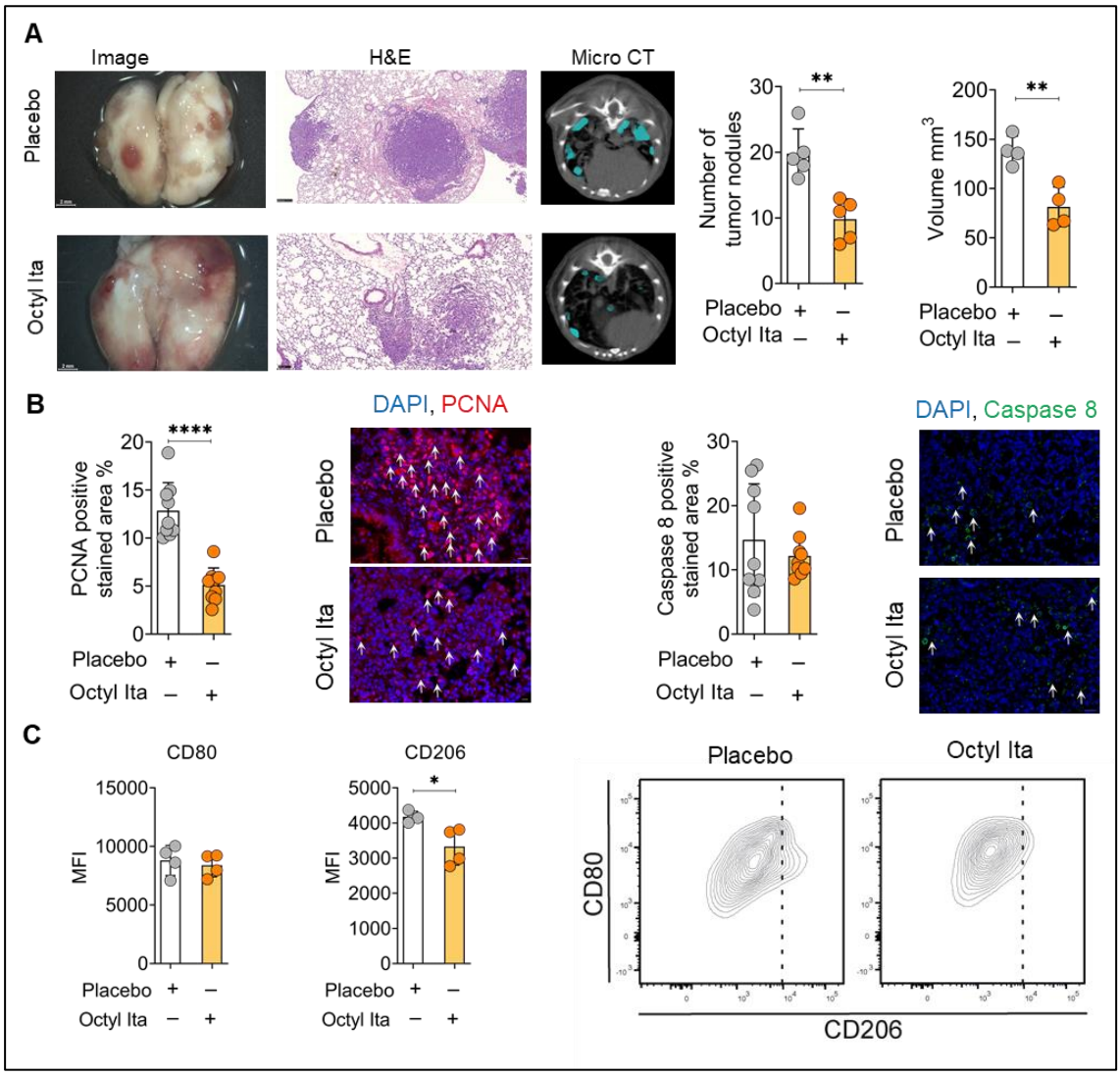

Figure 4-10. Octyl Ita suppresses the growth and metastasis of lung tumors. (A) Representative images of harvested lungs (scale bar: 2 mm), H&E-stained lung sections (scale bar: 100 μm), and micro-CT of WT mice that were first injected with LLC1 cells via the tail for lung tumor induction and then treated intraperitoneally with Octyl Ita (100 mg/kg) every other day for 2 weeks. Quantification of macroscopically counted lung tumor nodules (n=5 mice per group) and lung intensity of μCT images (n=4 mice per group). **(B)** Quantification and representative images of immunofluorescence staining for PCNA as a proliferative marker (red) and caspase 8 as an apoptosis marker (green) in lung tumor sections (n=9) and cell nuclei (blue). Scale bar=100μm (**C**) Mean fluorescence intensity (MFI) of CD80 and CD206 analyzed by FACS on Mϕ in lung tumors from mice treated with Octyl Ita and placebo (n=4 mice per group). Statistical significance was determined using a two-tailed unpaired Student's t-test. *p < 0.05, **p < 0.01, ****p 0.0001

We also confirmed the antitumor effect of Octyl Ita in a subcutaneous (SC) LLC1 tumor model. Specifically, Octyl Ita significantly inhibited tumor growth, as shown in Figure 4-11A. In addition, there was a reduction in tumor cell proliferation, as indicated by the reduced presence of positive PCNA cells (Figure 4-11B). In this SC tumor type, we observed higher rates of apoptosis after treatment with Octyl Ita, characterized by positive caspase8 cells (Figure 4-11B). This increase in apoptosis may be attributed to the particular nature of the SC tumor compared to lung tumors, in which apoptosis rates remained unchanged after treatment with Octyl Ita.

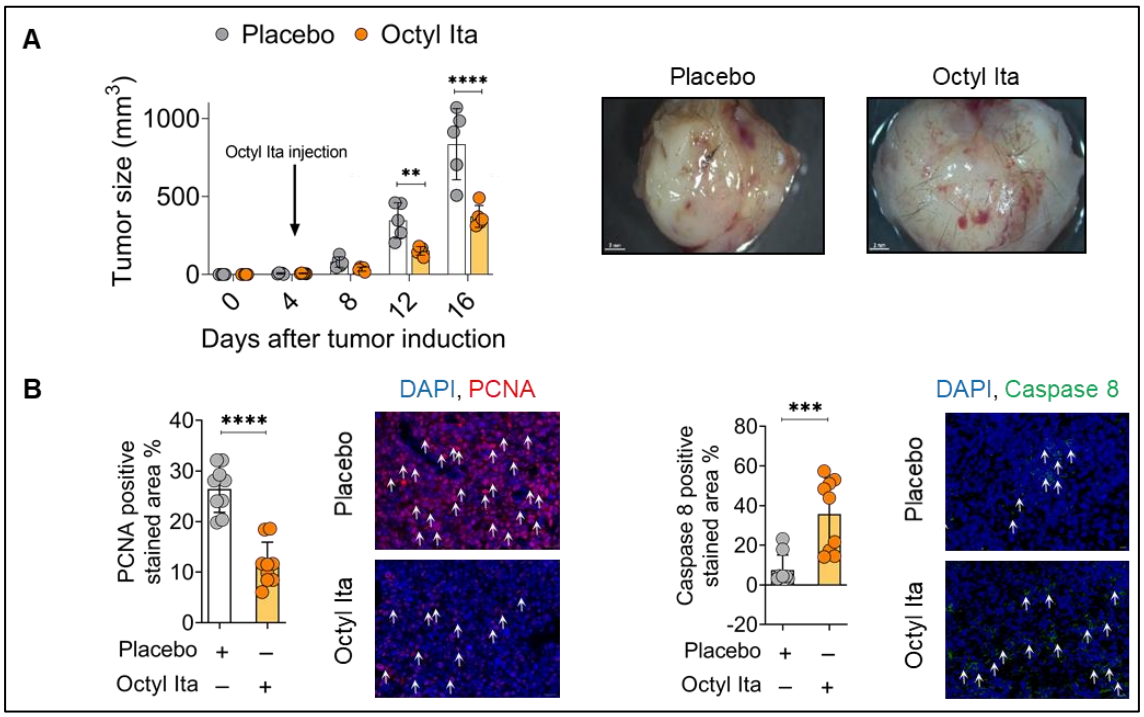

Figure 4-11. Octyl Ita reduced tumor growth in the subcutaneous tumor model of mice. **(A)** Measurement of tumor size during subcutaneous (SC) growth of LLC1 tumors treated with Octyl Ita (100mg/kg) intraperitoneally every other day for 10 days started 4 days after tumor induction (n=5 mice for each group). **(B)** Quantification and representative images of immunofluorescence staining for PCNA as proliferation marker (red) and caspase 8 as apoptosis marker (green) and cell nuclei (blue) in SC tumor sections (n=9). Scale bar = 100 µm. Data represent the mean ± s.e.m. Statistical significance was determined by a two-tailed, unpaired Student's t-test and a two-way ANOVA Tukey's Multiple Comparison Test. **p < 0.01, ***p < 0.001, ****p < 0.0001.

4.2.2 Octyl Ita diminished tumor proliferation and modulated TME immune phenotype in human tPCLS

To test the potential antiproliferative effect of Octyl Ita in human lung tumors, we next tested the antitumor potential of Octyl Ita in the human system. For this purpose, we established an *ex vivo* system using tPCLS obtained from freshly resected human lung

tumor samples, as shown in Figure 4-12A. To generate tPCLS, a freshly resected human lung tumor was filled with agarose in the operating room to preserve the structural integrity of the lung. Then, in collaboration with a pathologist, we carefully separated the tumor tissue from the non-tumor tissue and cut the tissue agarose blocks into approximately 400-300 μm thick sections using the vibrotome. The freshly prepared tPCLS from patients with lung cancer were treated with Octyl Ita (250μM) for 48 hours. Consistent with our *in vivo* results, the application of Octyl Ita resulted in a significant reduction in cell proliferation, as evidenced by a decrease in the number of EdU^+ cells within the tPCLS. However, it's worth noting that the apoptosis rate indicated by $TUNEL^+$ cells remained unchanged after treatment with Octyl Ita, as shown in Figure 4-12, B-C. Considering the immunomodulatory functions of Octyl Ita, especially in the TME, we also examined the TME immune profile of tPCLS after Octyl Ita treatment. The immune profile of tPCLS showed that Octyl Ita had a recognizable effect on the Mϕ phenotype in the TME. Specifically, it promoted an enhanced anti-tumor phenotype in the TAMs compared to the placebo-treated group by reducing $CD206^+$ TAMs (Figure 4-12D).

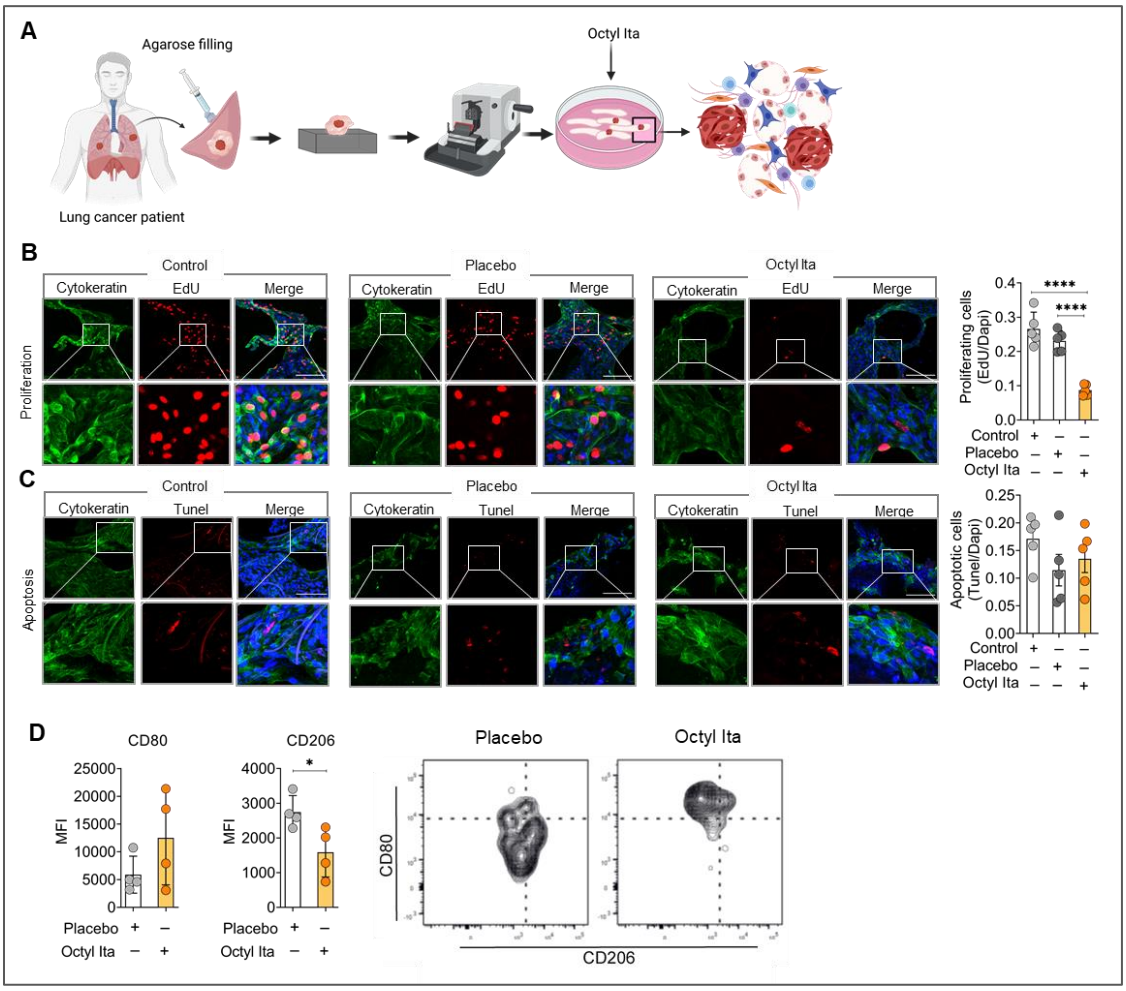

Figure 4-12. Octyl Ita reduced tumor proliferation and modulated TME immunophenotype in human tumor precision cut lung slices (tPCLS). (A) Schematic overview of the preparation of tPCLS from freshly harvested human lung tumors. **(B-C)** Representative fluorescence images of tPCLS (n=5 human lung tumors) treated with Octyl Ita (250µM) and DMSO as placebo for 48 hours, stained with proliferative (EdU$^+$) and apoptotic (TUNEL+) (red) markers and nuclear dye (DAPI$^+$, blue) in the tumor area (cytokeratin$^+$, green), followed by the quantification of proliferative (EdU$^+$) and apoptotic (Tunel$^+$) cells in relation to the total cell number (DAPI$^+$, blue) in the tumor area (cytokeratin$^+$, green). Scale bars = 250 µm (upper field for B and C) and 50 µm (lower field for B and C). (**D**) FACS analysis of Mϕ in tPCLS (n=4 human lung tumors) treated with Octyl Ita (250µM) and DMSO (placebo) for 48 hours. Statistical significance was determined by a two-tailed, unpaired Student's t-test and a one-way ANOVA Tukey's Multiple Comparison Test. *p < 0.05, ****p < 0.0001.

4.2.3 Octyl Ita reduced the proliferation of human lung cancer cells *in vitro*

Octyl Ita is renowned for its ability to activate the NRF2 by alkylation of Kelch-like ECH-associated protein 1 (KEAP1) protein (Mills, Ryan et al. 2018). Given the prevalence of KEAP1 mutations in lung cancers (Cancer Genome Atlas Research 2014), we conducted a comprehensive assessment of Octyl Ita's antiproliferative effects on various lung cancer cell lines, some with KEAP1 mutations (A549 and H838) and others without (H1650, H1975, and H226) (Tate, Bamford et al. 2019). To determine the optimal and non-toxic treatment concentration, we first performed viability tests (see Figure 4-13A) and decided on a concentration of 250µM Octyl Ita. Remarkably, Octyl Ita attenuated proliferation in all lung cancer cell lines tested, regardless of whether KEAP1 mutations were present or not (Figure 4-13B). This suggests that the proliferation inhibitory effect of Octyl Ita is independent of the KEAP1/NRF2 signaling pathway and the likely mutational landscape of the cells. Moreover, we observed that Octyl Ita not only reduced the number of A549 cells but also slightly increased the apoptosis rate (Figure 4-13C). Interestingly, we investigated whether Octyl Ita treatment could lead to an increase in intracellular itaconic acid levels. To assess this, we performed LC–MS analysis and found a significant increase in intracellular itaconic acid levels in A549 cells after 6 hours of Octyl Ita treatment (Figure 4-13D). Accordingly, we examined the effects of direct itaconic acid treatment, which also led to a reduction in A549 cell proliferation (Figure 4-13E). Overall, these data support our *in vivo* and *ex vivo* antiproliferative effects of Octyl Ita in mice and human lung cancer.

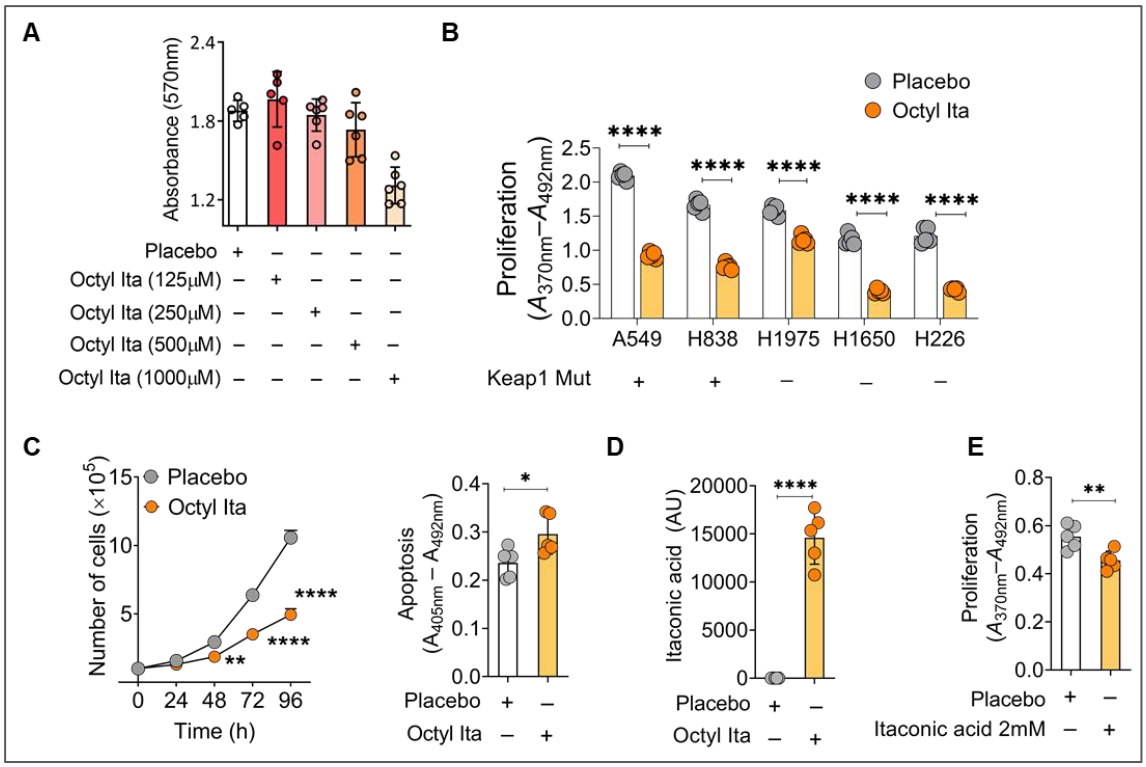

Figure 4-13. Octyl Ita/itaconic acid reduced the proliferation of human lung cancer cell lines *in vitro*. **(A)** Cytotoxic evaluation of Octyl Ita at various concentrations in the A549 cell line after 48 hours as measured by the 3-(4,5-dimethylthiazol-2-yl)-2,5-diphenyl-2H-tetrazolium bromide (MTT) assay (n=6). **(B)** Proliferation rate of different lung cancer cell lines after treatment with Octyl Ita (250μM) and DMSO (placebo) for 48 hours (n=5). **(C)** Number of A549 cells after 96-hour treatment with Octyl Ita (250μM) (n=3), followed by the apoptosis rate of A549 cell line after 48-hours treatment with Octyl Ita (250μM) and DMSO (placebo) (n=5). **(D)** Intracellular itaconic acid concentration measured by LC-MS in A549 cells treated with Octyl Ita (250μM) for 6 hours (n=5). **(E)** Proliferation of A549 cells after treatment with itaconic acid 2mM for 48 hours (pH adjusted to 7.5) (n=5). Data represent the mean ± s.e.m. Statistical significance was determined by a two-tailed, unpaired Student's t-test and a one-way ANOVA Tukey's Multiple Comparison Test. *p < 0.05, **p < 0.01, ****p < 0.0001.

4.2.4 Irg1 deficient macrophages showed pro-tumor phenotype after indirect co-culture with lung cancer cells *in vitro*

To further validate the anti-tumor properties of Irg1-expressing Mϕ, we performed *in vitro* co-cultures of Irg1-deficient BM derived-macrophages (BMDMs) with LLC1 cancer cells, as shown in Figure 4-14A. Our results from these in vitro co-culture experiments were very informative. When Irg1-deficient BMDMs were co-cultured with LLC1 cancer cells, this resulted in the development of a pro-tumor Mϕ phenotype within the Irg1-deficient BMDMs. This pro-tumor phenotype was characterized by a decrease in the expression of the anti-tumor Mϕ marker Tnf and an increase in the expression of pro-tumor Mϕ such

as Arg1 and Fizz1, as shown in Figure 4-14B. These *in vitro* results were consistent with our previous *in vivo* results and confirmed our general conclusions. When LLC1 cancer cells were exposed to CM from co-cultures of Irg1-deficient BMDMs and LLC1, we observed a marked increase in the proliferation of LLC1 cells. In addition, there was a slight reduction in apoptosis in LLC1 cells compared to co-cultures with WT Mϕ, as shown in Figure 4-14C.

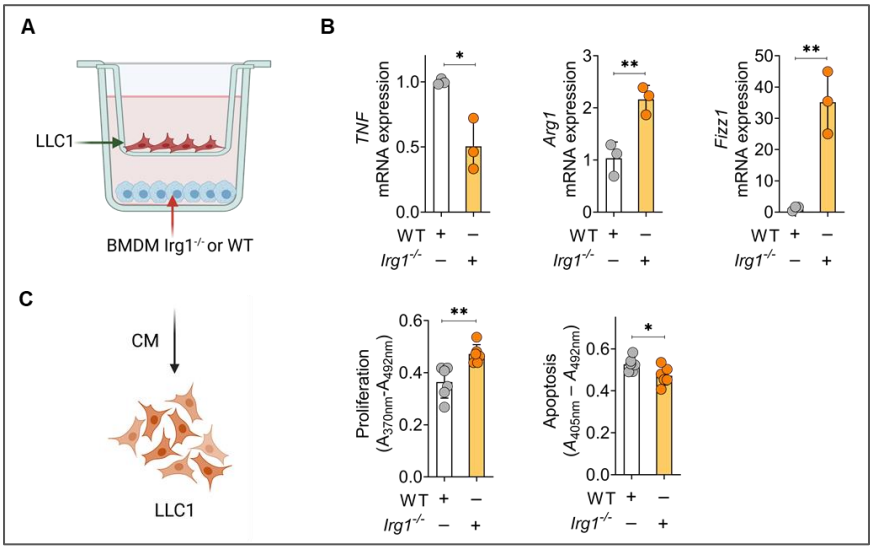

Figure 4-14: Indirect co-culture of bone marrow-derived macrophages with the cancer cell LLC1. (**A**) Schematic representation of co-culture between LLC1 and bone marrow-derived macrophages (BMDM) isolated from WT or *Irg1*$^{-/-}$ mice. (**B**) mRNA levels of Tnf as anti-tumor Mϕ marker and Arg1 and fizz1 as pro-tumor Mϕ markers (n= 3). (**C**) Proliferation and apoptosis of LLC1 treated with conditional media (CM) of co-culture between LLC1 and WT or *Irg1*$^{-/-}$ BMDM (n=6). Data represent the mean ± s.e.m. Statistical significance was determined by a two-tailed unpaired Student's t-test. *p < 0.05, **p < 0.01.

4.2.5 Overexpression of IRG1 in lung cancer cells reduced the proliferation rate *in vitro*

To test the intracellular effect of itaconate, we examined the effect of overexpression of IRG1, the key gene responsible for itaconate production in cancer cells (Figure 14-15A). Indeed, when IRG1 was overexpressed, we found a remarkable reduction in both the number of A549 cells and their proliferation rates, with no significant change in apoptosis levels (Figure 14-15, B-C). We also demonstrated that IRG1 overexpression can reduce the proliferation rate of H1650 cells that do not harbor KEAP1 mutations (Figure 14-15D).

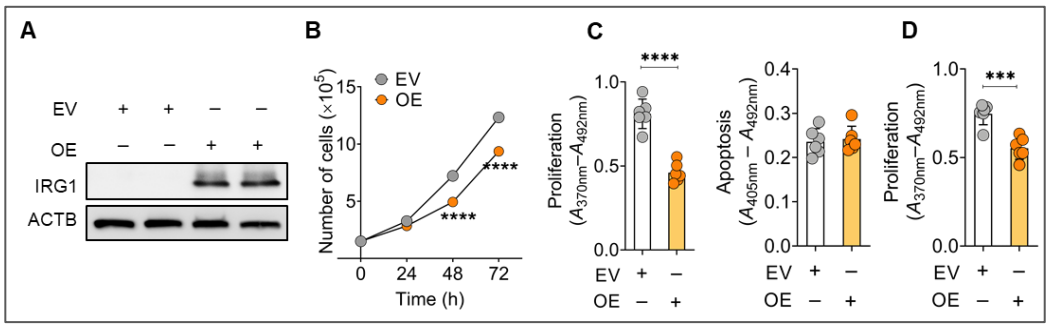

Figure 4-15. Overexpression of IRG1 reduces the proliferation of lung cancer cells. (A) Representative images of Western blot analysis of IRG1 in A549 cells transfected with the IRG1 overexpression (OE) and empty vector (EV) construct (n=3). **(B)** Cell numbers of A549 transfected with IRG1 OE and EV during 72 hours (n=3). **(C)** Proliferation and apoptosis rate of IRG1 OE and EV-transfected A549 (n=6). **(D)** Proliferation rate of IRG1 OE and EV-transfected H1650 (n=6). Data represent the mean ± s.e.m. Statistical significance was determined by a two-tailed, unpaired Student's t-test comparison. ***p < 0.001, ****p < 0.0001.

Taken together, our results provide substantial support for Octyl Ita and itaconate as potent antiproliferative metabolites. These compounds inhibited tumor growth in various experimental settings, including *in vivo* mouse models, *ex vivo* human lung tPCLS, and *in vitro* lung cancer cell lines. Furthermore, these data shed light on the critical proliferation-inhibitory role of IRG1 in the context of lung tumorigenesis.

4.3 Octyl Ita regulates pentose phosphate metabolism and associated antioxidant signaling pathways

4.3.1 Octyl Ita reduces pentose phosphate metabolites in lung cancer

To understand the mechanism by which Octyl Ita exerts its inhibitory effect on cancer cell proliferation, we first examined the metabolic changes induced by Octyl Ita in A549 cells. To gain insight into these changes, we performed a targeted metabolomic analysis by LC-MS on A549 cell lysates after 6 hours of Octyl Ita treatment. The results of this analysis showed a surprising and significant reduction in the levels of most metabolites associated with the pentose phosphate pathway (PPP) after 6 hours of Octyl Ita treatment, as shown in Figure 4-16A. To further validate the time-dependent nature of this effect, we checked PPP metabolite levels at 24 hours after Octyl Ita treatment. Remarkably, consistent data emerged showing a sustained and significant reduction in PPP metabolites at 24 hours compared to both the placebo control and the 6-hour Octyl Ita treatment group (Figure 4-16B). To further confirm PPP downregulation after Octyl Ita treatment, the ratio of ribose 5-phosphate (5P) to ribulose 5-phosphate was determined. This ratio showed a decrease, which serves as further evidence for the suppression of the PPP by Octyl Ita, as shown in Figure 4-16C.

In agreement with our previous results, Octyl Ita reduced cellular GSH levels and the ratio of GSH to GSSG after 6 hours, as shown in Figure 4-16D. This decrease in GSH levels and GSH/GSSG ratio implies a decrease in the availability of reduced nicotinamide adenine dinucleotide phosphate (NADPH), an important product of PPP required for the reduction of GSSG. These results are consistent with our previous observations of the influence of Octyl Ita on PPP metabolism. To examine the effects of Octyl Ita-induced PPP downregulation on cellular metabolism, we investigated mitochondrial and glycolytic changes. To this end, we measured OCR as an indicator of mitochondrial function and ECAR as a marker of glycolysis rate in A549 cells after 24 hours of ctyl Ita treatment. Surprisingly, Octyl Ita did not elicit any significant effects on OCR or ECAR levels, as shown in Figure 4-16E. This suggests that the inhibition of PPP by Octyl Ita does not significantly affect other metabolic pathways in A549 cells, indicating a possibly different mechanism underlying its proliferation inhibitory effect.

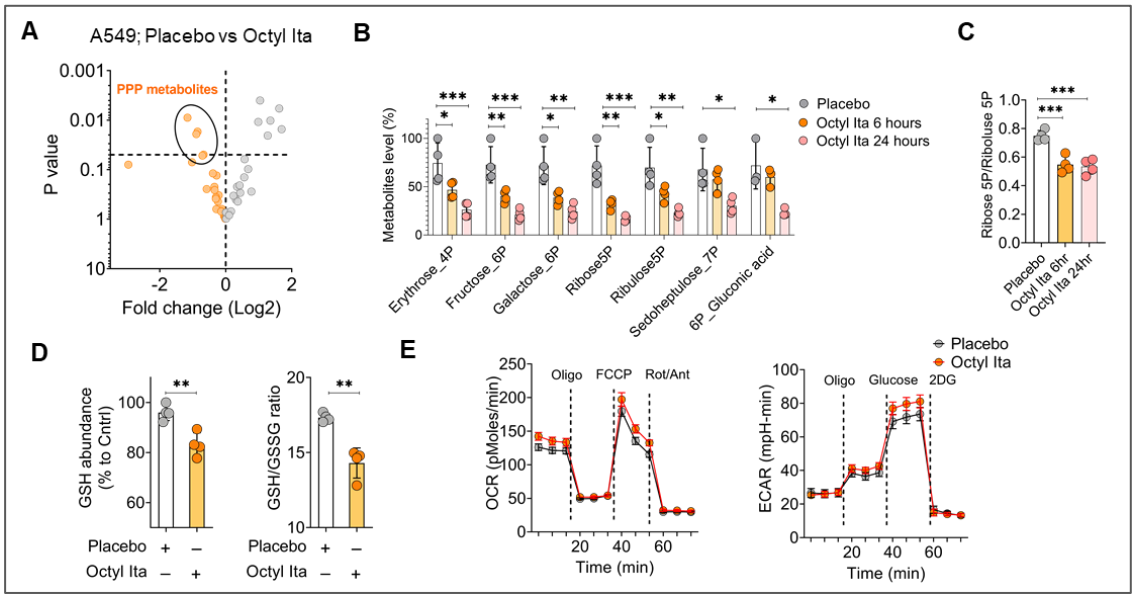

Figure 4-16. Octyl Ita regulates the pentose phosphate metabolic pathway and associated downstream signaling pathways in lung cancer cells. (**A**) Volcano plot of metabolites showing that PPP metabolites are the most reduced metabolites in A549 cell lysate after 6-hour treatment with octy Ita (250μM) (n=4). (**B**) Levels of PPP metabolites in A549 cell lysate measured by LC-MS metabolomics after 6-hour and 24-hour octy Ita treatment, shown as percentage (%) to control group (n=4). (**C**) Ratio of ribose-5-phosphate (5P) to ribolus-5P in A549 cell lysate after 6 hours and 24 hours of octyl- Ita treatment (n=4). (**D**) Ratio of glutathione (GSH) and GSH/glutathione disulfide (GSSG) in A549 cell lysate after 6 hours of Octyl Ita treatment (n=4). (**E**) Oxygen consumption rate (OCR) and extracellular acid rate (ECAR) in A549 after 24 hours of Octyl Ita treatment (n=3 independent samples). Oligo, oligomycin; FCCP, carbonyl cyanide (p-trifluoromethoxy) phenylhydrazone Rot/Ant, rotenone/antimycin; 2DG, 2-deoxy-d-glucose. Data represent the mean ± s.e.m. Statistical significance was determined by a two-tailed, unpaired

Student's t-test and a one-way ANOVA Tukey's Multiple Comparison Test. *p < 0.05, **p < 0.01, ***p < 0.001.

4.3.2 Octyl Ita modulates the transcriptomic and proteomic profile of cancer cells

The next question was what transcriptomic and proteomic effects PPP reduction by Octyl Ita may have in cancer cells. To this end, we performed RNA-seq and proteomic analyzes on A549 cells after 48 hours of Octyl Ita treatment. Octyl Ita-treated cells exhibited a distinct transcriptomic and proteomic profile as shown in the principal component analysis (PCA) plots (Figure 4-17A). In particular, heme oxygenase 1 (HMOX1), a downstream target of Octyl Ita (Mills, Ryan et al. 2018), was significantly upregulated at the mRNA and protein levels after treatment with Octyl Ita (Figure 4-17A, depicted in volcano plots). Through the integrated analysis of RNA-seq and proteomic data, we found the intertwining of different pathways that PPP-associated signaling pathways including peroxisome, ROS pathway and UV response are enriched to (Figure 4-17B).

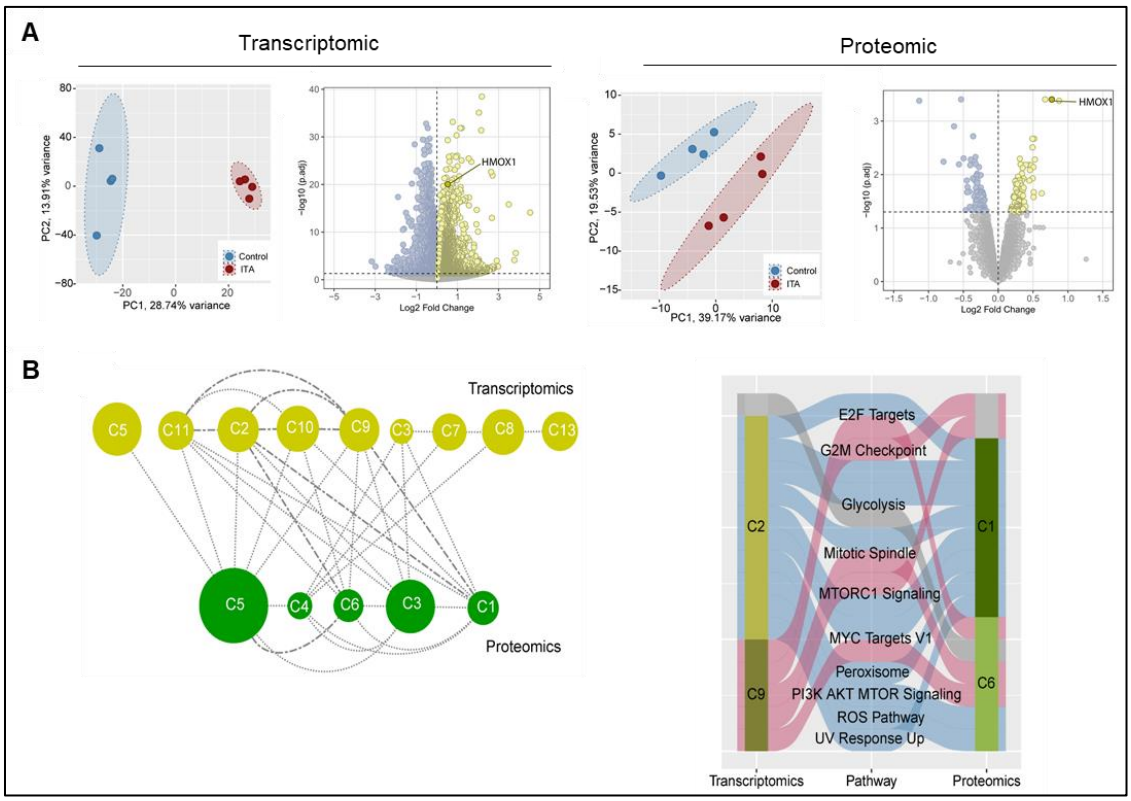

Figure 4-17. Octyl Ita modulates the transcriptomic and proteomic profile of lung cancer cells. (**A**) Principal component analysis (PCA) score plot showing different transcriptomic and proteomic signatures in DMSO (placebo) and Octyl Ita-treated A549 after 48 hours. Volcano plot of genes showing HMOX1 as one of the most upregulated genes and proteins in A549 after 48 hours of Octyl Ita treatment (n=4 independent samples) (**B**) Integration analysis of transcriptomic and proteomic data in A549 after 48 hours of Octyl Ita treatment showing the global association

analysis network and identified communities (left panel). Sankey plot illustrating the association of transcriptome and proteome data and showing the pathways correlated between transcriptome and proteome data (right panel).

Given the proliferation inhibitory effect of Octyl Ita in lung cancer cells, we also examined proliferation and cell cycle genes at the transcriptomic level, both of which were significantly downregulated in A549 cells after 48 hours of Octyl Ita treatment (Figure 4-18, A-B).

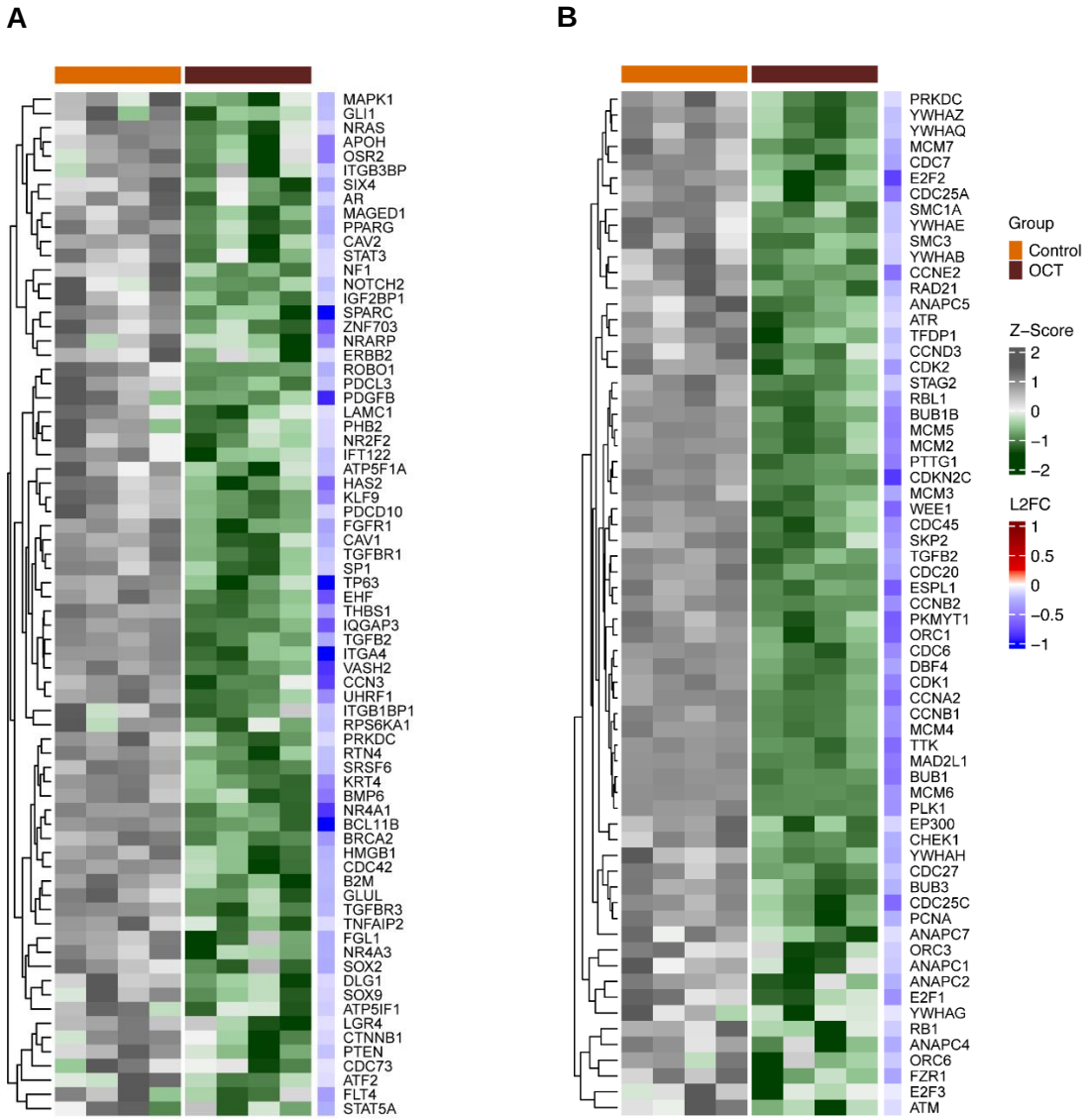

Figure 4-18. Octyl Ita reduced proliferation and cell cycle-associated genes. (A-B) Heatmap of genes involved in (**A**) cell proliferation and (**B**) cell cycle that are reduced in A549 treated with Octyl Ita for 48 hours compared to DMSO (control). Transcript levels were analyzed by RNA-seq (n=4).

In summary, these results suggest that Octyl Ita reprograms cancer cell metabolism primarily by inhibiting PPP, which subsequently leads to differential regulation at the

transcriptome and proteome levels, particularly in metabolic pathways associated with antioxidant defense.

4.4 Octyl Ita inhibits G6PD and thus exerts antiproliferative effects

4.4.1 IRG1/Itaconate and Octyl Ita inhibit the activity of G6PD

We investigated the mechanisms by which Octyl Ita regulates PPP metabolism and its downstream effects. Initially, we focused on NRF2, a transcriptional regulator of PPP metabolism that could potentially be affected by Octyl Ita. However, we could not detect any significant changes in NRF2 levels after 6 hours of Octyl Ita treatment (Figure 4-19A). We directed our attention to the early inhibitory effects of Octyl Ita on PPP, particularly within the first 6 hours, and hypothesized that Octyl Ita might target G6PD, which serves as the first limiting enzyme in PPP. However, Western blot analysis showed comparable levels of G6PD protein in the Octyl Ita-treated group and the placebo group (Figure 4-19A). In addition, we found no significant changes in the mRNA expression of other enzymes involved in PPP (Figure 4-19B).

Interestingly, Octyl Ita showed significant inhibition of G6PD activity in A549 cells (Figure 4-19C). As for the effects of intracellular itaconate on G6PD, overexpression of IRG1 also decreased G6PD activity without affecting NRF2 and G6PD protein levels (Figure 4-19D). Further analysis of G6PD enzyme kinetics in A549 homogenate revealed that Octyl Ita significantly reduced the G6PD maximum velocity (V_{max}) from 1.52 (U) in the placebo group to 1.19 (U) in the treated group. However, we did not detect any significant changes in the Michaelis constant (K_m) between the two groups, which remained at 188 μM in the placebo group and 178 μM in the Octyl Ita treated group (Figure 4-19E).

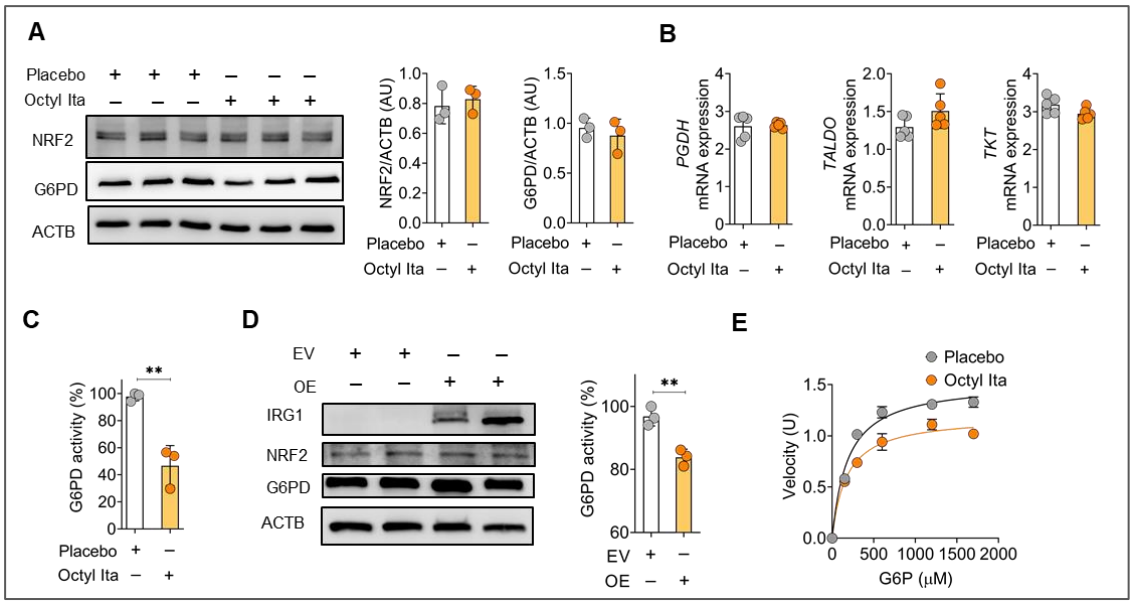

Figure 4-19. IRG1 and Octyl Ita inhibit the activity of glucose-6-phosphate dehydrogenase (G6PD). (A) Western blot analysis of NRF2 and G6PD in A549 cells after 6 hours of treatment with Octyl Ita, followed by densitometric quantification of relative NRF2 and G6PD expression. ACTB (β-actin) was used as a loading control (n=3). **(B)** G6PD, phosphogluconate dehydrogenase (PGDH), transaldolase (TALDO) and transketolase (TKT) mRNA expression in A549 cells treated with Octyl Ita (250μM) for 24 hours (n=5). **(C)** Activity of G6PD by photometric detection of NADPH production in homogenates of A549 treated with Octyl Ita (250μM) for 6 hours (n=3). **(D)** Western blot analysis of IRG1, NRF2 and G6PD in A549 cells transfected with IRG1 OE and EV constructs (n=3. G6PD activity by photometric detection of NADPH production in homogenates of A549 cells transfected with IRG1 OE and EV constructs (n=3). **(E)** Michaelis-Menten kinetics of G6PD activity in A549 homogenates was measured by photometric detection of NADPH production. Data represent the mean ± s.e.m. Statistical significance was determined using a two-tailed unpaired Student's t-test **p < 0.01.

We then tested the direct inhibitory effect of itaconic acid on the recombinant human G6PD enzyme. Indeed, itaconic acid strongly inhibited the recombinant G6PD activity with a half-maximal inhibitory concentration (IC50) of about 150 μM, suggesting a direct effect of itaconic acid on G6PD activity (Figure 4-20A). Kinetic analysis of the enzyme also showed that itaconic acid (200μM) significantly reduced the V_{max} (2.83 U for control versus 1.55 U for itaconic acid) and slightly altered the K_m value (404.9 μM for control versus 369.3 μM for itaconic acid) (Figure 4-20B). To test whether other mitochondrial metabolites also have an inhibitory effect on G6PD, we measured G6PD activity after incubation with dimethyl fumarate, diethyl succinate and dimethyl malonate as a succinate dehydrogenase inhibitor. We only found that itaconic acid was able to reduce G6PD activity, no other metabolites (Figure 4-20C).

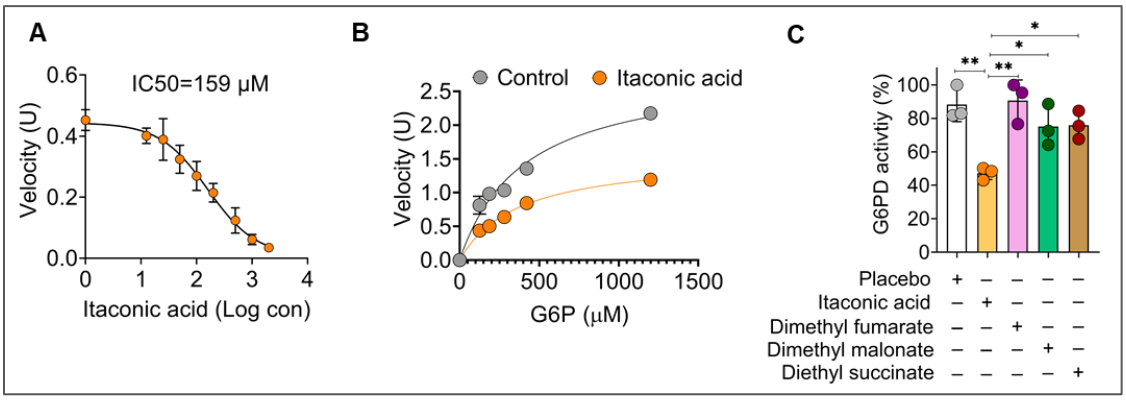

Figure 4-20. Itaconic acid inhibits G6PD activity. (A) Activity of the recombinant human G6PD enzyme directly after incubation with different concentrations (con) of itaconic acid (n=3). The pH of the reaction was optimized between 7.2 and 7.4. **(B)** Michaelis-Menten kinetics of recombinant G6PD activity with and without treatment with itaconic acid (200µM) was measured by photometric detection of NADPH production. Data represent the mean of three independent experiments. **(C)** Recombinant human G6PD enzyme activity directly after incubation with itaconic acid and various metabolites (n=3). Data represent the mean ± s.e.m. Statistical significance was determined by a two-tailed, unpaired Student's t-test *p < 0.05, **p < 0.01.

To confirm the direct effect of itaconic acid on the activity of the G6PD enzyme, we performed an in silico analysis to determine the potential binding of itaconic acid to G6PD. Itaconic acid interacts with the residues in the binding sites of G6PD mainly via hydrogen bonds with the amino acids Ala436, Gly204, Pro434, Glu206 and Lys205. The interaction of itaconic acid with G6PD was confirmed by calculating the binding affinity, which showed -5.2 (Kcal/mol) for itaconic acid compared to -4.9 (Kcal/mol) for β-D-glucopyranose-6-phosphate as a natural substrate of G6PD (Figure 4-21, A-B). All these data indicate that Octyl Ita and itaconic acid can bind directly to G6PD and strongly inhibit its activity.

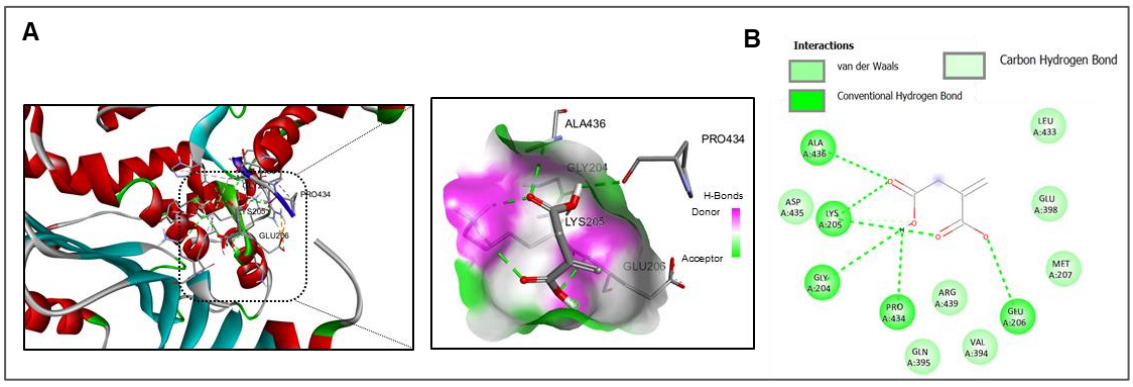

Figure 4-21. Itaonic acid directly binds to G6PD activity. (A) Docking pose of itaconic acid inside human G6PD (left). On right, the conformation of the itaconic acid (in stick) inside the enzymatic binding site of human G6PD, represented as solvent accessible surface (SAS) and

colored according to the hydrophobicity of the residues. (**B**) A two-dimensional representation of the molecular interactions between itaconic acid and human G6PD. Here, the colors used to refer the different interactions, as indicated in the legend.

4.4.2 Octyl Ita reduces the proliferation of cancer cells by inhibiting G6PD

To investigate whether the proliferation inhibitory effect of Octyl Ita is related to its inhibitory effect on G6PD, we performed experiments in which we knocked down G6PD in A549 cells and then treated them with Octyl Ita for an additional 24 hours. A549 cells deficient in G6PD showed lower proliferation rates, and this effect was consistent between the Octyl Ita-treated and placebo groups. These results confirm the functional importance of G6PD in mediating the proliferation inhibitory effect of Octyl Ita in cancer cells (Figure 4-22A).

Furthermore, we investigated whether supplementation of downstream G6PD metabolites could counteract the proliferation-inhibitory effect of Octyl Ita. Pretreatment of A549 cells with 6-phosphogluconate (6GP), D-ribose (DR) and ribose-5-phosphate (R5P) as downstream metabolites of G6PD prevented the proliferation-inhibitory effect of Octyl Ita (Figure 4-22B). In contrast, the antiproliferative effect of Octyl Ita remained unaffected in the presence of N-acetylcysteine (NAC), a potent antioxidant (see Figure 4-22C).

These results suggest that the proliferation-inhibiting effect of Octyl Ita is related to its ability to suppress ribose production, which is essential for RNA/DNA synthesis. This link appears to be more significant than the modulation of the antioxidant system associated with G6PD activity.

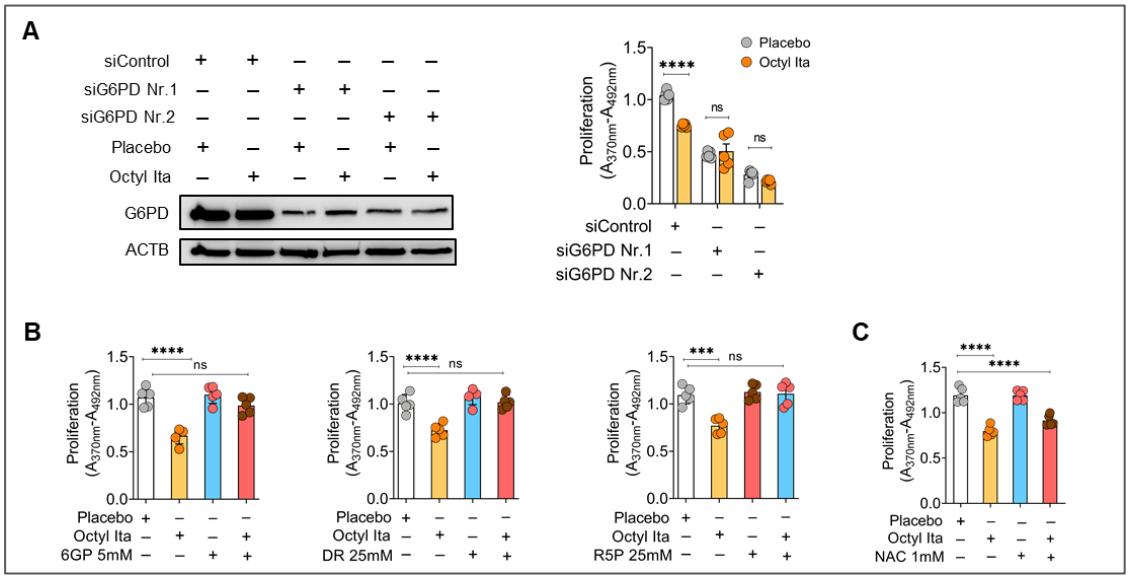

Figure 4-22. Octyl Ita reduces the proliferation of cancer cells by inhibiting G6PD. **(A)** Western blot analysis confirming the knockdown of G6PD in A549 cells after siG6PD and siControl transfection for 24 hours, followed by Octyl Ita (250µM) treatment for another 24 hours.

Validation of G6PD knockdown in A549 in which ACTB (β-actin) was used as loading control (left panel). Proliferation rate of A549 cells first transfected with siRNA against G6PD (siG6PD) and siRNA scramble (siControl) for 48 hours and then treated with Octyl Ita for another 24 hours (n=6) (right panel). **(B)** Proliferation rate of A549 cells pretreated with G6PD metabolites such as 6-phosphogluconate (6GP) 5mM, D-ribose (DR) 25mM and ribose 5-phosphate (R5P) for 3 hours followed by Octyl Ita treatment for a further 24 hours (n=5). **(C)** Proliferation rate of A549 cells pretreated with N-acetylcysteine (NAC) for 3 hours followed by Octyl Ita treatment for 24 hours (n=5). Data represent the mean ± s.e.m. Statistical significance was assessed by one- and two-way ANOVA Tukey's multiple comparison test. ns=not significant, ***p < 0.001, ****p < 0.0001.

4.4.3 Octyl Ita regulates HMOX1 expression by G6PD in cancer cells

We also investigated whether the increased levels of HMOX1 induced by Octyl Ita are dependent on G6PD. Interestingly, A549 cells with G6PD deficiency exhibited higher HMOX1 protein levels, supporting the link between HMOX1 and G6PD (comparison between lines 1 and 3 in Figure 4-23A and Figure 4-23B). Although early treatment with Octyl Ita (after 6 hours) did not result in significant changes in HMOX1 protein levels (the comparison between lines 1 and 2 in Figure 4-23A), there was significant upregulation of HMOX1 after 48 hours of Octyl Ita treatment (the comparison between lines 1 and 2 in Figure 4-23B), confirming our proteomic data. Interestingly, G6PD-deficient cells in both the Octyl Ita-treated and placebo groups showed similar upregulation of HMOX1 after 48 hours of Octyl Ita treatment, suggesting that Octyl Ita increases HMOX1 levels through its modulation of G6PD (comparison between lines 2 and 4 in Figure 4-23B). Overall, these results suggest that the ability of Octyl Ita to inhibit G6PD is a major reason for its proliferation inhibitory effect, which in turn leads to the upregulation of HMOX1.

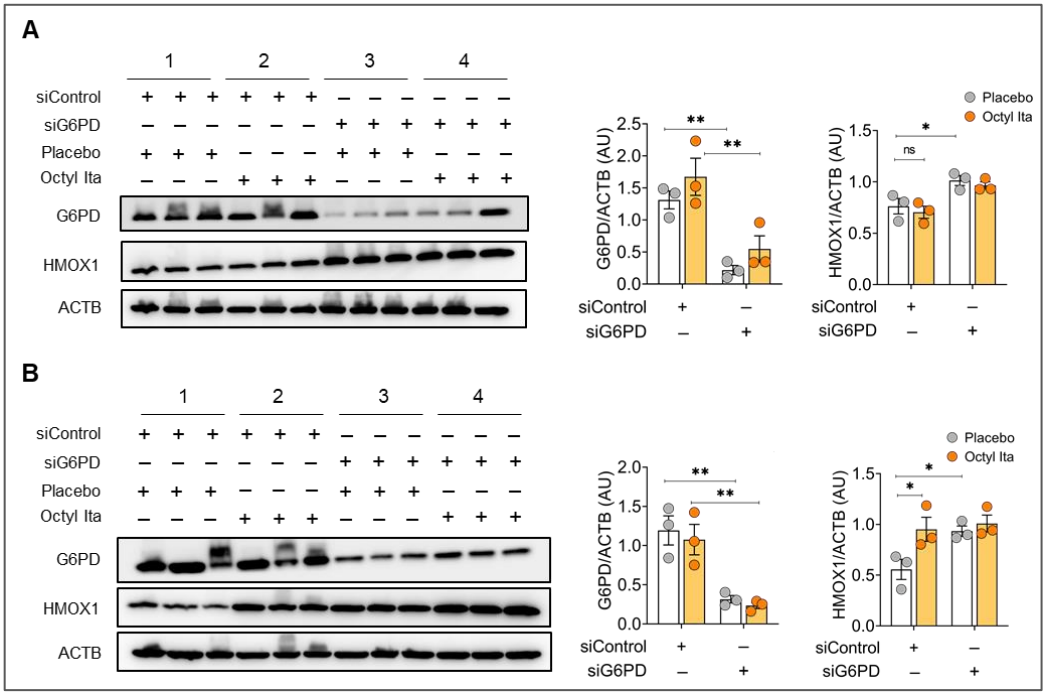

Figure 4-23. Octyl Ita regulates HMOX1 expression by G6PD. (A-B) Western blot analysis of HMOX1 and G6PD followed by densitometric quantification of relative HMOX1 expression in A549 transfected with siG6PD and siControl for 24 hours and then treated with Octyl Ita (250μM) for an additional **(A)** 6 hours or **(B)** 48 hours. ACTB (β-actin) was used as a loading control (n=3). Data represent the mean ± s.e.m. Statistical significance was determined by a two-way ANOVA Tukey's multiple comparison test. ns=not significant, *p < 0.05, **p < 0.01.

4.5 IRG1/Itaconate and Octyl Ita regulate PPP metabolism and induce an anti-tumor phenotype in macrophages

4.5.1 IRG1/Itaconate and Octyl Ita reduce G6PD activity and confer an anti-tumor phenotype to macrophages

To extend our understanding of the role of IRG1/itaconate in shaping the lung TME via the regulation of G6PD and PPP in Mϕ, we first focused on determining IRG1/itaconate levels in different Mϕ states, including naïve Mϕ (M0), anti-tumor Mϕ polarized with LPS (100 ng/ml) and IFNγ (100 U/ml) for 24 hours, and pro-tumor Mϕ polarized with IL4 (20 ng/ml) for 24 hours (Sarode, Zheng et al. 2020, Zheng, Weigert et al. 2020). Significantly, we observed that *IRG1* and itaconate levels were higher in anti-tumor Mϕ, which are known for their antiproliferative and pro-apoptotic effects on cancer cells (Figure 4-24, A-B). Interestingly, this upregulation of IRG1/itaconate was accompanied by a decrease in G6PD activity specifically in anti-tumor Mϕ, in contrast to M0 and pro-tumor Mϕ, which had lower itaconate levels and higher G6PD activity (Figure 4-24C).

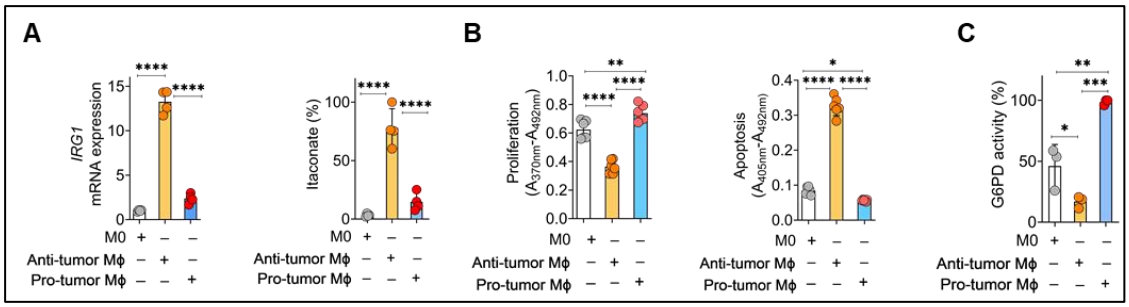

Figure 4-24. Profiling of *IRG1* gene expression, itaconic acid level and G6PD activity in Mϕ. **(A)** mRNA level of *IRG1* and intracellular itaconic acid level measured by LC-MS in M0, anti-tumor Mϕ (polarized with LPS (100 ng/ml) and IFNγ (100 U/ml) for 24 hours) and pro-tumor Mϕ (polarized with IL4 (20 ng/ml) for 24 hours), shown as percentage based on M0 group (n=4). **(B)** Proliferation and apoptosis rate of A549 treated with CM of M0, anti-tumor Mϕ and pro-tumor Mϕ for 24 hours (n=6). **(C)** G6PD activity measured by photometric determination of intracellular NADPH production in M0, anti-tumor Mϕ and pro-tumor Mϕ and presented as a percentage relative to the anti-tumor Mϕ group (n=3). The data represent the mean ± s.e.m. Statistical significance was assessed by a one-way ANOVA Tukey's multiple comparison test. *p < 0.05, **p < 0.01, ***p < 0.001, ****p < 0.0001.

Given the upregulation of itaconate in anti-tumor Mϕ, we asked whether Octyl Ita could reprogram pro-tumor Mϕ to anti-tumor Mϕ. Treatment of A549 cells with CM from pro-tumor Mϕ treated with Octyl Ita (250μM) resulted in a greater reduction in proliferation rate than direct Octyl Ita treatment (Figure 4-25A, left panel). However, the apoptosis rate of A549 was not significantly affected (Figure 4-25A, right panel). To verify our results in cancer cells, we examined G6PD protein and activity levels in pro-tumor Mϕ treated with Octyl Ita (250μM). While G6PD protein levels remained unchanged upon treatment with Octyl Ita (Figure 4-25B), G6PD activity was significantly reduced (Figure 4-26C).

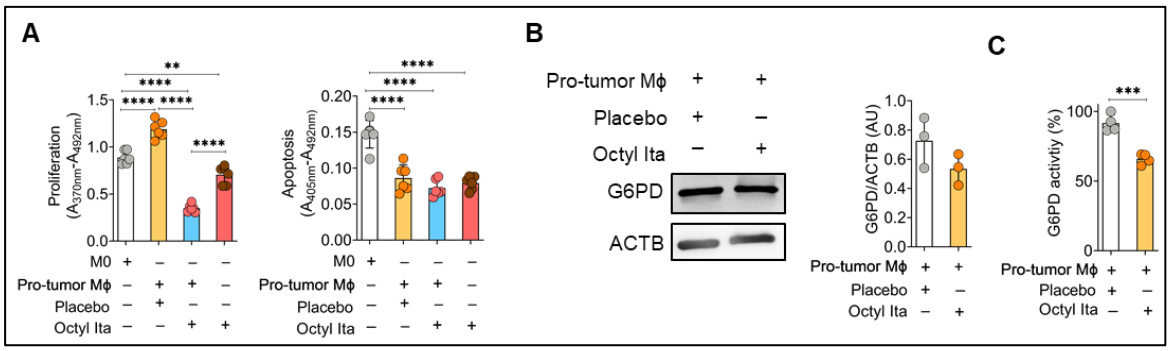

4-25. Octyl Ita confers an anti-tumor phenotype to pro-tumor Mϕ and reduces G6PD activity. (A) Proliferation and apoptosis rate of A549 cells after 24 hours treatment with direct Octyl Ita (250μM) and CM of pro-tumor Mϕ treated with DMSO (placebo) or Octyl Ita (250μM) for

24 hours (n=6). **(B)** Western blot analysis of G6PD in pro-tumor Mϕ treated with DMSO (placebo) and Octyl Ita (250µM) for 12 hours, followed by densitometric quantification of Western blot analysis for relative G6PD expression. ACTB (β-actin) was used as a loading control (n=3). **(C)** Activity of G6PD measured by photometric determination of intracellular NADPH production in pro-tumor Mϕ after treatment with DMSO (placebo) and Octyl Ita (250µM) for an additional 12 hours, presented as a percentage relative to the placebo group (n=4). The data represent the mean ± s.e.m. Statistical significance was determined using a two-tailed unpaired Student's t-test and a one-way ANOVA Tukey's Multiple Comparison Test. **p < 0.01, ***p <0.001, ****p < 0.0001.

Furthermore, the reduction in G6PD activity was accompanied by a significant downregulation of PPP metabolism and a decrease in the ratio of ribose-5P to ribulose-5P after 12 hours of Octyl Ita treatment in pro-tumor Mϕ (Figure 4-26, A-B).

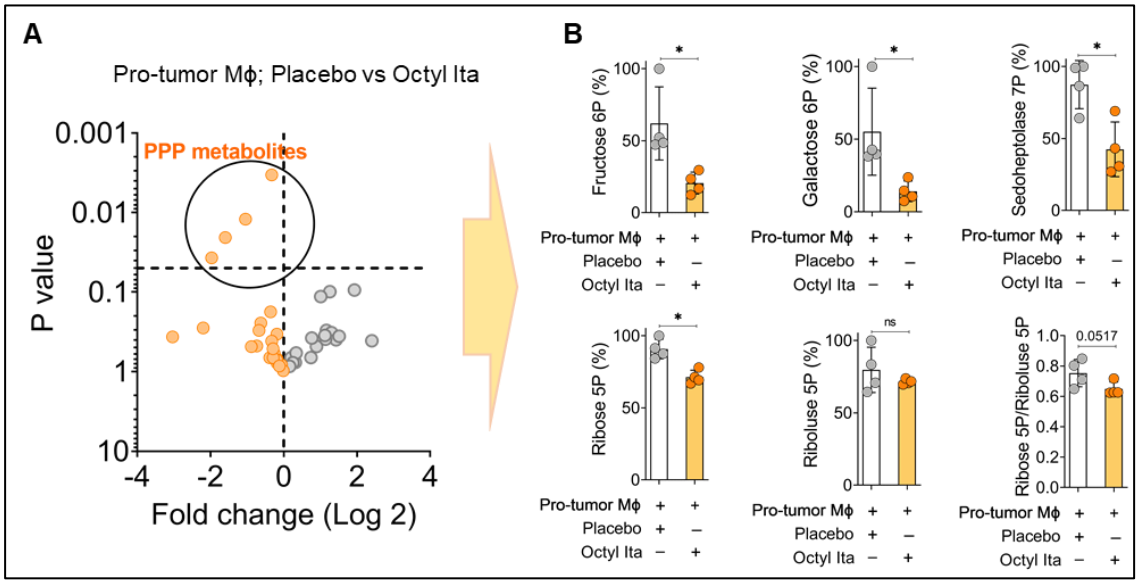

Figure 4-26. Octyl Ita reduces PPP metabolism in pro-tumor Mϕ. (**A**) Targeted metabolome showing that PPP metabolites significantly decreased in pro-tumor Mϕ cell lysate (polarized with IL4 (20 ng/ml) for 24 hours) after octy Ita (250µM) treatment for 12 hours (volcano diagram, left panel). (**B**) PPP metabolites measured by LC-MS, shown as a percentage of placebo groups, and ratio of ribose-5-phosphate (5P) to ribolus-5P in the pro-tumor Mϕ cell lysate after 12 hours of octy Ita (250µM) treatment (n=4). Data represent the mean ± s.e.m. Statistical significance was determined by a two-tailed unpaired Student's t-test. *p < 0.05.

All in all, these data show that the inhibitory effect of Octyl Ita can be considered a general phenomenon that can occur independently of cell types. However, it appears that the inhibitory effect of Octyl Ita on PPP metabolism is stronger in cancer cells than in Mϕ, which may be due to other compensatory mechanisms capable of replenishing downstream G6PD metabolites. Previous studies have shown that Octyl Ita can activate NRF2 in Mϕ (Runtsch, Angiari et al. 2022), which contrasts to our findings in cancer cells.

However, we also detected an upregulation of NRF2 protein after Octyl Ita treatment in pro-tumor mϕ, together with increased mRNA expression of PPP-related enzymes (Figure 4-27, A-B). This suggests a cell-specific regulation of NRF2 and indicates a preceding inhibitory effect of Octyl Ita on G6PD activity.

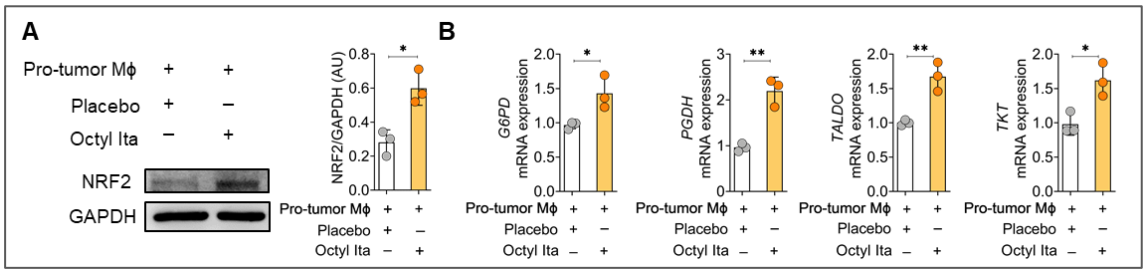

Figure 4-27. Octyl Ita induces NRF2 and related genes in pro-tumor Mϕ. (A) Western blot analysis of NRF2 in pro-tumor mϕ treated with DMSO (placebo) and Octyl Ita (250µM) for an additional 24 hours. Right panel: densitometric quantification of Western blot analysis for relative NRF2 expression. ACTB (β-actin) was used as a loading control (n=3). **(B)** G6PD, PGDH, TALDO and TKT mRNA expression in pro-tumor Mϕ after treatment with DMSO (placebo) and Octyl Ita (250µM) for an additional 24 hours (n=3). The data represent the mean ± s.e.m. Statistical significance was determined by a two-tailed unpaired Student's t-test. *p < 0.05, **p < 0.01.

In a next step, we investigated the transcriptomic and proteomic effects of PPP reduction by Octyl Ita in pro-tumor Mϕ. To this end, we performed RNA-seq and proteomic analysis in pro-tumor Mϕ after 24 hours of treatment with Octyl Ita. PCA transcriptome analysis showed that 24 hours treatment with Octyl Ita significantly altered the transcriptome profile of pro-tumor Mϕ, particularly enriching pathways related to PPP and the antioxidant defense system, such as heme metabolism, UV response, ROS pathway, and xenobiotic metabolism (Figure 4-28A, left panel). Remarkably, an induction of anti-tumor Mϕ markers (TNF, CXCL8, STAT1 and IRF1) and a reduction of pro-tumor Mϕ markers (CSF1R, IL10, ALOX15 and IL4R) were observed upon treatment with Octyl Ita in pro-tumor Mϕ (Figure 4-28A, right panel). These data support the antitumor function of Octyl Ita. Proteomic analysis also revealed a significant upregulation of HMOX1 with an enhancement of xenobiotic metabolism and ROS metabolic pathways dependent on PPP metabolism (Figure 4-28B). Integration of transcriptomic and proteomic data revealed the intertwining of various signaling pathways, including anti-tumor signaling pathways associated with inflammation, such as the interferon-γ response, and signaling pathways associated with PPP, including peroxisome, ROS signaling, and UV response (Figure 4-28, C-D).

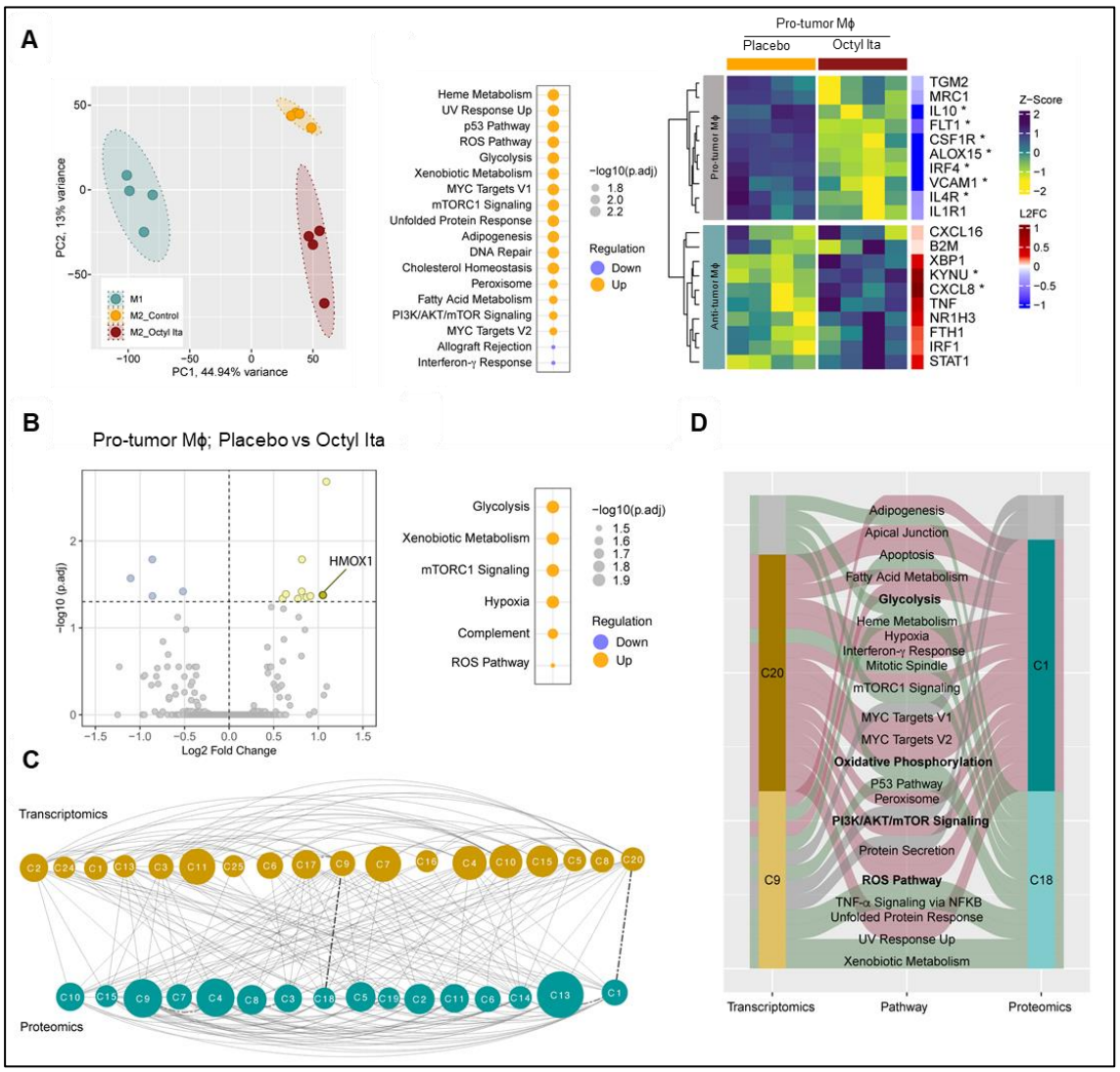

Figure 4-28. Transcriptome and proteome profile of pro-tumor Mϕ after Octyl Ita treatment. **(A)** Left panel; PCA score plot showing the different transcriptomic signature of anti-tumor Mϕ and pro-tumor Mϕ after 24 hours of further treatment with DMSO (placebo) or Octyl Ita (250μM). Middle panel: Analysis of transcriptomic changes in pro-tumor Mϕ treated with either DMSO (placebo) or Octyl Ita (n=4). Right panel: heatmap depicting the expression of anti-tumor and pro-tumor associated genes in pro-tumor Mϕ treated with either DMSO (placebo) or Octyl Ita (250μM) over a 24-hour period. **(B)** Volcano plot of proteomic analysis and associated enriched pathways between pro-tumor Mϕ treated with DMSO (placebo) or Octyl Ita (250μM) for 24 hours (n=4). **(C)** Integration analysis of the transcriptomic and proteomic data from A and B showing the global association analysis network and the identified communities. **(D)** Sankey plot illustrating the association of transcriptomic and proteomic data and showing the signaling pathways that show correlation between the two data sets.

To determine whether the anti-tumor properties of pro-tumor Mϕ treated with Octyl Ita depended on G6PD, we applied a strategy of G6PD knockdown in pro-tumor Mϕ followed by treatment with Octyl Ita at a concentration of 250µM for 24 hours (Figure 4-29A, upper left schematic). The CM from G6PD-deficient pro-tumor Mϕ cells was found to reduce the proliferation rate of A549 cells compared to CM from pro-tumor Mϕ cells transfected with siControl, highlighting the pro-tumor role of G6PD in Mϕ (see Figure 4-29A). Of note, CM of Octyl Ita-treated G6PD KD pro-tumor Mϕ resulted in a higher proliferation rate in A549 cells compared to CM of Octyl Ita-treated pro-tumor Mϕ with intact G6PD function (Figure 4-29A). This observation suggests that G6PD, although playing a partial role, contributes to the anti-tumor phenotype induced by Octyl Ita in pro-tumor Mϕ. However, it is important to note that there was no significant effect on the apoptosis rate of A549 cells when exposed to CM from G6PD-deficient pro-tumor Mϕ, regardless of whether they were treated with placebo or Octyl Ita (Figure 4-29A).

In addition, G6PD-deficient pro-tumor Mϕ exhibited elevated levels of *TNF*, which is considered an anti-tumor marker (Figure 4-29B). Octyl Ita was able to increase *TNF* levels in G6PD-deficient pro-tumor Mϕ by approximately 50%, suggesting a partial involvement of G6PD in the induction of anti-tumor markers in pro-tumor Mϕ by Octyl Ita. Of note, however, G6PD deficiency had no detectable effect on *CSF1R*, which is associated with pro-tumor Mϕ markers (Figure 4-29A). This suggests that the regulation of CSF1R, a pro-tumor marker, by Octyl Ita is independent of G6PD function. We also examined the effects of G6PD deficiency on HMOX1 protein expression in pro-tumor Mϕ. Interestingly, the absence of G6PD in pro-tumor Mϕ resulted in a slight increase in HMOX1 expression. However, the induction of HMOX1 by Octyl Ita in pro-tumor Mϕ was found to be apparently independent of G6PD (Figure 4-29C). These data suggest that the mechanism underlying the upregulation of HMOX1 by Octyl Ita is context-specific; in cancer cells it occurs via G6PD, whereas in pro-tumor Mϕ it is associated with NRF2 (Mills, Ryan et al. 2018).

In summary, these results demonstrate that Octyl Ita has the ability to reprogram pro-tumor Mϕ into an anti-tumor phenotype while suppressing PPP metabolism in pro-tumor Mϕ by inhibiting G6PD activity.

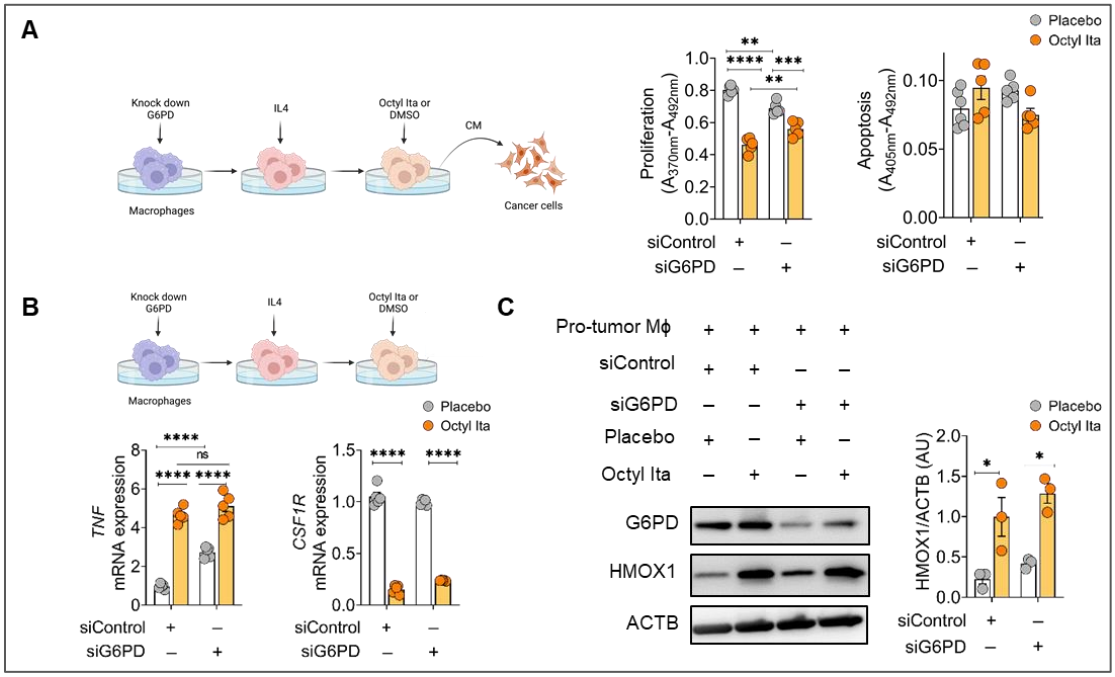

Figure 4-29. G6PD is partially involved in the anti-tumor function of Octyl Ita in the reprogramming of pro-tumor Mϕ into an anti-tumor phenotype. (A) Proliferation and apoptosis rate of A549 after 24-hour treatment with CM of siG6PD-transfected pro-tumor Mϕ that were subsequently subjected to treatment with DMSO (placebo, 24 hours) or Octyl Ita (250μM, 24 hours) (n=5). **(B)** mRNA levels of TNF and CSF1R in pro-tumor Mϕ transfected with siG6PD or siControl followed by treatment with Octyl Ita (250μM) or DMSO (placebo) for 24 hours (n=5). **(C)** Western blot analysis of HMOX1 and G6PD and densitometric quantification of relative HMOX1 expression in G6PD-deficient or control pro-tumor Mϕ treated with DMSO (placebo) or Octyl Ita (250μM) for an additional 24 hours (n=3), followed by densitometric quantification of Western blot analysis for relative G6PD expression. ACTB (β-actin) was used as a loading control. Data represent the mean ± s.e.m. Statistical significance was determined by two-tailed unpaired Student's t-test and one-way ANOVA Tukey's Multiple Comparison Test. ns=not significant, *p < 0.05, **p < 0.01, ***p < 0.001, ****p < 0.0001.

4.5.2 IRG1/Itaconate axis is necessary for anti-tumor phenotype of macrophages

To investigate whether IRG1 and intracellular itaconate play a role in regulating G6PD activity in anti-tumor Mϕ, we performed experiments in which we knocked down IRG1 in Mϕ and then polarized them into an anti-tumor Mϕ phenotype using LPS (100 ng/ml) and IFNγ (100 U/ml) for 6 hours. This specific time point was chosen because the expression of *IRG1* and the secreted levels of itaconate were higher compared to the 24 hours time point (Figure 4-30, A-B). Interestingly, we observed that IRG1-deficient anti-tumor Mϕ had similar levels of G6PD protein as the control group (Figure 4-30C). However, the loss of IRG1 in anti-tumor Mϕ resulted in an increase in G6PD activity and a decrease in itaconic acid production (Figure 4-30, D-E).

In addition, IRG1-deficient anti-tumor Mϕ showed lower mRNA levels of *TNF*, an anti-tumor marker, and higher mRNA levels of *CSF1R*, a pro-tumor marker, at the phenotypic level (Figure 4-30F). Moreover, the proliferation rates of A549 cancer cells were higher when treated with CM from IRG1-deficient anti-tumor Mϕ, indicating the involvement of IRG1/itaconate in the anti-tumor function of anti-tumor Mϕ. However, this is worth noting that CM of IRG1-deficient anti-tumor Mϕ did not significantly affect apoptosis rates in A549 cancer cells (Figure 4-30G).

To further test whether reduced G6PD activity is associated with anti-tumor functions in Mϕ, we performed knockdown experiments in which G6PD was knocked down in Mϕ, followed by polarization with LPS (100 ng/ml) and IFNγ (100 U/ml) for 6 hours. G6PD-deficient anti-tumor Mϕ exhibited higher mRNA levels of *TNF* as an anti-tumor marker and lower mRNA levels of *CSF1R* as a pro-tumor marker (Figure 4-30H). Similarly, CM of G6PD-deficient anti-tumor Mϕ resulted in reduced proliferation rates of A549 cancer cells, although it did not significantly affect apoptosis rates (Figure 4-30I). Taken together, these results confirm that intracellular itaconate and IRG1 play a role in regulating G6PD activity during Mϕ activation, thereby promoting an anti-tumor phenotype in Mϕ.

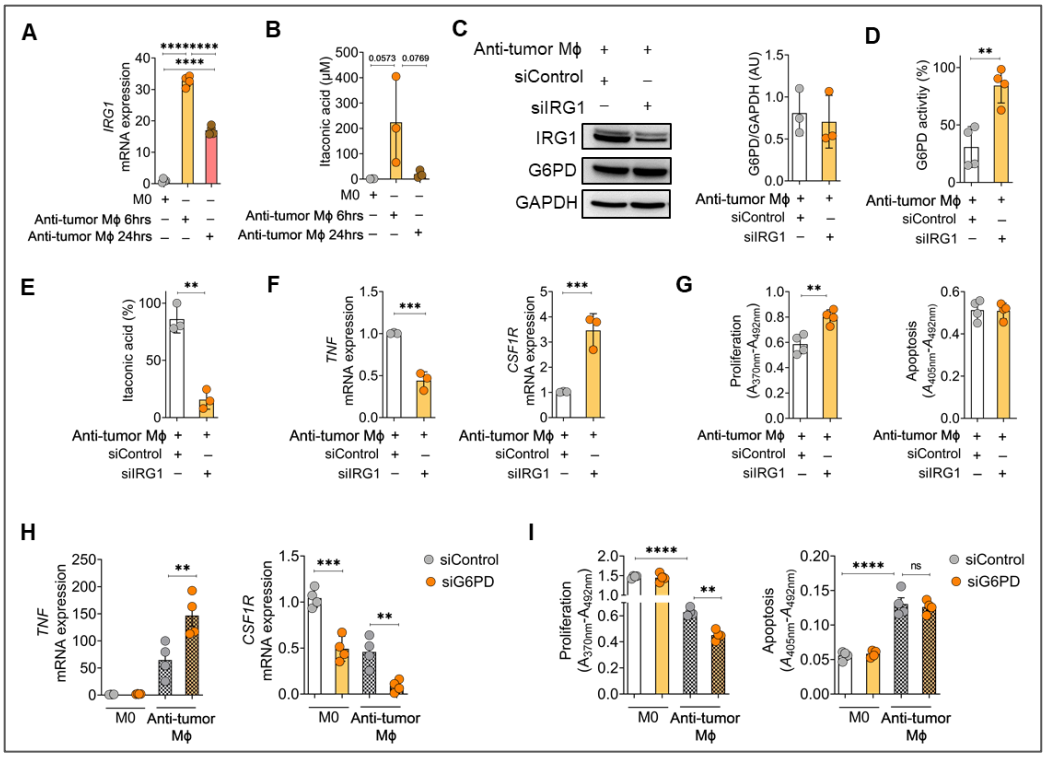

Figure 4-30. IRG1 and G6PD are necessary elements for anti-tumor phenotype in macropahges. (A) mRNA levels of IRG1 in anti-tumor Mϕ (polarized with LPS (100 ng/ml) and IFNγ (100 U/ml) for 6 and 24 hours) (n=4). **(B)** Itaconic acid content (μM) measured by LC-MS in

the supernatant of anti-tumor Mϕ after 6 and 24 hours (n=3). **(C)** Western blot analysis of IRG1 and G6PD in siIRG1- and siControl-transfected anti-tumor Mϕ, followed by densitometric quantification of Western blot analysis for relative G6PD expression. Glyceraldehyde-3-phosphate dehydrogenase (GAPDH) was used as a loading control (n=3). **(D)** Activity of G6PD by photometric detection of intracellular NADPH production in siIRG1 and siControl-transfected anti-tumor Mϕ (n=4). **(E)** Intracellular itaconic acid concentration measured by LC-MS in siIRG1 and siControl-transfected anti-tumor Mϕ (n=3). **(F)** mRNA levels of *TNF* and *CSF1R* in siIRG1- and siControl-transfected anti-tumor Mϕ (n=3). **(G)** Proliferation and apoptosis rate of A549 treated with CM of siIRG1 and siControl-transfected anti-tumor Mϕ (n=4) for 24 hours. **(H)** mRNA levels of *TNF* and *CSF1R* in siG6PD and siControl-transfected anti-tumor Mϕ (n=4). **(I)** Proliferation and apoptosis rate of A549 treated with CM of siG6PD and siControl-transfected anti-tumor Mϕ for 24 hours (n=4). Data represent the mean ± s.e.m. Statistical significance was assessed using a two-tailed, unpaired Student's t-test, one-way and two-way ANOVA Tukey's Multiple Comparison Test. ns=not significant, *p < 0.05, **p < 0.01, ***p < 0.001, ****p < 0.0001.

4.5.3 IRG1/Itaconate affects G6PD activity in human and mouse lung tumors

Next, we examined G6PD activity in lung tumors under two different conditions: Lung tumors from Irg1-deficient mice and lung tumors from mice treated with Octyl Ita. Consistent with our previous in vitro results, the absence of Irg1 resulted in an increase in G6PD activity in situ as observed in lung tumors compared to WT control mice. This pattern was consistent in various lung tumor models, including tumors induced by Kras mutation, orthotopic implantation, and bone marrow transplantation (Figure 4-31, A-C). These results underscored the critical role of Irg1 in regulating G6PD activity in the tumor.

On the other hand, when Octyl Ita was administered to mice with orthotopically localized lung tumors, we observed a decrease in G6PD activity in the tumors compared to the placebo-treated group (Figure 4-31D). This result indicates that treatment with Octyl Ita has an inhibitory effect on G6PD activity in the tumor microenvironment. Next, we investigated whether the antitumor properties of IRG1-expressing Mϕ ($IRG1^+$ Mϕ) correlate with lower G6PD activity in human lung tumors. We found that in lung TME, $CD68^+$ Mϕ expressing IRG1 ($CD68^+/IRG1^+$) had significantly lower G6PD activity than $CD68^+$ Mϕ without IRG1 expression ($CD68^+/IRG1^-$) (Figure 4-31E). These results provided further evidence for the inhibitory effect of IRG1 and itaconate on G6PD activity and emphasize their potential as therapeutic targets for lung cancer.

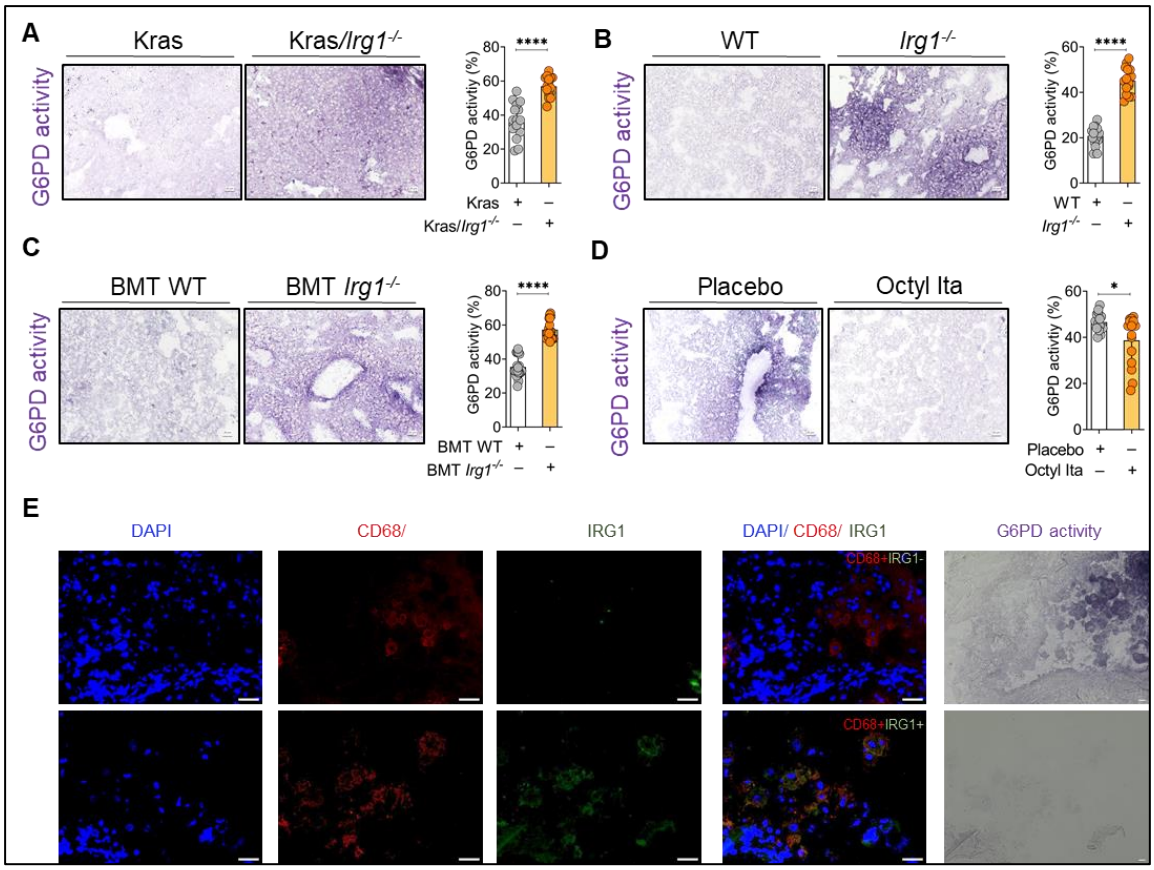

Figure 4-31. IRG1 regulates G6PD activity in lung tumors. (A-D) Representative images of in situ G6PD activity in the lungs of (**A**) Kras and Kras/*Irg1*$^{-/-}$ mice (n=15), (**B**) WT and *Irg1*$^{-/-}$ mice injected with LLC1 via the tail (n=15), **(C)** BMT WT and *Irg1*$^{-/-}$ mice injected with LLC1 via the tail (n=15), and **(D)** WT mice initially injected with LLC1 cells via the tail and then treated intraperitoneally with Octyl Ita (100mg/kg) every other day for 2 weeks (n=15) (scale bar= 20μm). **(E)** Immunofluorescence images for CD68 (red), IRG1 (green) and cell nuclei (blue) in CD68^{+}/IRG1^{+} and CD68^{+}/IRG1^{-} Mϕ in human lung cancer tissue with the corresponding in situ G6PD activity on the same slide (scale bar=100μm). Data represent the mean ± s.e.m. Statistical significance was determined using a two-tailed unpaired Student's t-test. *p < 0.05, **p < > 0.01, ***p < 0.001.

In support of the tumor-promoting function of G6PD, we observed increased activity and mRNA expression of G6PD in human lung adenocarcinomas, which was correlated with poorer survival rates in lung cancer patients (hazard ratio=1.22 and p value=0.039) (Figure 4-32, A-C).

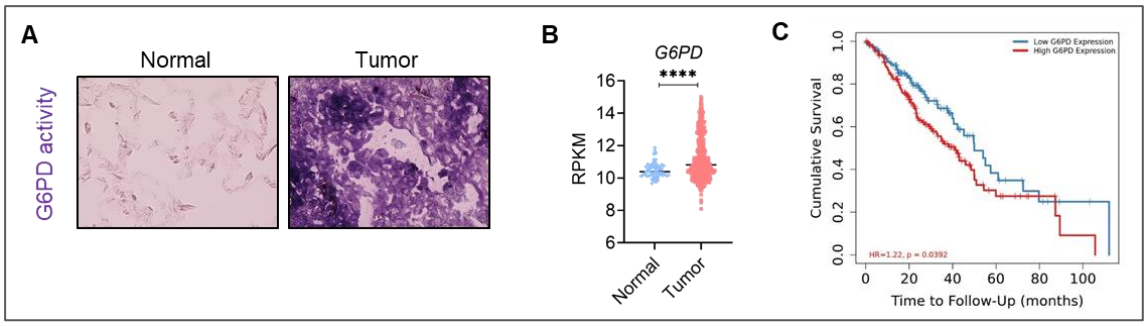

Figure 4-32. G6PD activity and gene profiles in human lung tumors (A) Representative images of in situ G6PD activity in human normal and tumor lung tissue (n=3). **(B-C)** G6PD mRNA levels in human lung tumors (RPKM: reads per kilobase of transcript per million reads mapped) and Kaplan-Meier survival analysis of lung adenocarcinoma patients stratified by G6PD expression. HR, hazard ratio. Data represent the mean ± s.e.m. Statistical significance was determined by a two-tailed unpaired Student's t-test. ****p < 0.0001.

5 Discussion

My thesis focused on the role of IRG1 and itaconate in the development of lung tumors. The results emphasize the protective function of IRG1 in the development of lung cancer. In addition, our study has shown that Octyl Ita effectively inhibits the growth of lung tumors. This inhibitory effect is primarily due to its ability to reduce the activity of the G6PD enzyme, which affects PPP metabolism and its products, mainly ribuolose and ribose-5-phosphate as precursors of nucleotide synthesis. These results open a path for a new therapeutic strategy aimed at slowing the development of lung tumors. Our key findings supporting the potential anti-tumor implications of IRG1/itaconate in lung cancer are summarized in Figure 6H: i) We observed that depletion of Irg1 resulted in acceleration of lung tumor development in mice, particularly in Kras-driven models, orthotopic models and BM transplantation models. ii) In mouse models of lung tumors, including orthotopic and SC models, Octyl Ita demonstrated the ability to reduce the progression of lung tumors. (iii) In addition, we could establish tPCLS as an *ex vivo* human platform to use for preclinical drug screening including immunotherapy agents and understanding lung TME complexity and phenotype. Interestingly, Octyl Ita application in tPCLS not only reduce cancer proliferation but also induce anti-tumor phenotype to TAMs within tPCLS. This data not only confirm tPCLS as dynamic and viable ecosystem but also confirm anti-tumor feature of Octyl Ita. Furthermore, Octyl Ita/itaconate effectively inhibited the proliferation of lung cancer cells *in vitro* human lung cancer cell lines. iv) Our research revealed that IRG1-deficient Mϕ exhibited tumor-promoting properties. Conversely, Octyl Ita had the ability to reprogram these pro-tumor Mϕ into an anti-tumor phenotype. v) We identified IRG1/Itaconate and Octyl Ita as inhibitors of G6PD activity, a crucial enzyme in cancer cell proliferation. This inhibition not only curbed cancer cell growth but also induced an anti-tumor phenotype in Mϕ. In summary, our study sheds light on the protective role of IRG1 and itaconate in lung tumor development while highlighting the potential of Octyl Ita as a therapeutic agent that can prevent lung tumor progression through its unique mechanisms involving the regulation of G6PD and PPP metabolism (Figure 4-33).

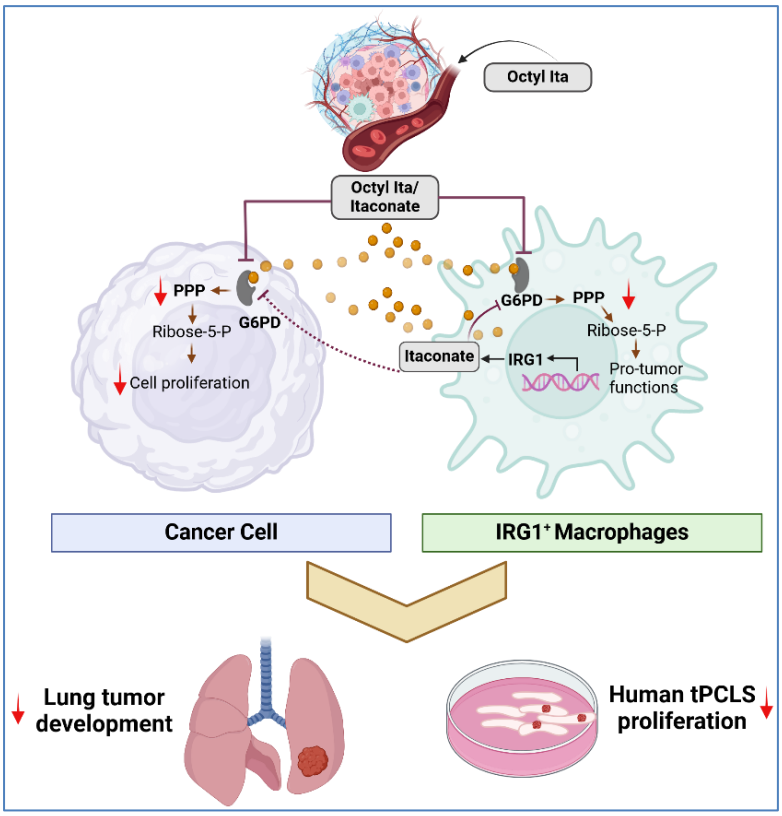

Figure 4-33. IRG1/Itaconate and exogenous Octyl Ita reduce cancer cell proliferation and induce an anti-tumor phenotype in Mϕ mainly through pentose phosphate metabolism. Exogenous Octyl Ita and endogenous itaconate regulate PPP metabolism by binding to G6PD and inhibiting its activity. Consequently, cancer cell proliferation is suppressed by reducing downstream PPP metabolites including R5P as a precursor of DNA/RNA synthesis. In the same line, G6PD inhibition by Octyl Ita reprograms pro-tumor Mϕ into anti-tumor Mϕ. The figure was prepared in www.Biorender.com with this agreement number: *CO26EKYJHQ.*

5.1 Anti-tumor properties of IRG1-expressing macrophages in lung cancer

Previous research has consistently indicated that Mϕ and myeloid cells are the main culprits for IRG1 expression (Peace and O'Neill 2022), especially in the context of proinflammatory responses, which are one of the main features of anti-tumor Mϕ in lung (Sarode, Zheng et al. 2020, Zheng, Weigert et al. 2020, Zheng, Sarode et al. 2023). Considering the lack of information about IRG1 level and function in lung cancer, we asked which cell types can be responsible for IRG1 expression in lung tumors and whether there is any difference for IRG1 expression in normal lung and tumor tissues. Here, we could provide further evidence to support the assumption that IRG1 is primarily expressed by Mϕ populations in both human and mouse tumors. To support this claim, we analyzed both our own and publicly available scRNA-seq datasets from mouse and human lung tumors. Our results not only confirmed that Mϕ are the primary cells responsible for *IRG1* expression, but also showed a more pronounced anti-tumor gene signature in IRG1-expressing Mϕ compared to Mϕ without *IRG1* expression. It is noteworthy that our analysis did not detect *IRG1* gene expression in lung cancer data from The Cancer Genome Atlas (TCGA) (Goldman, Craft et al. 2020).

The absence of *IRG1* gene expression in lung cancer data can be attributed to several factors. One possible explanation is the limited sequencing depth and dropout, where the technology may not accurately capture all gene expression. In addition, the complicated composition of the lung TME plays an important role. It is known that the lung TME comprises distinct pro-tumor compartments, and it is plausible that these compartments contain subsets of pro-tumor Mϕ that do not express *IRG1*. The latter explanation may be more valid, especially in light of research conducted by Casanova-Acebes et al (Casanova-Acebes, Dalla et al. 2021), that documented a gradual decrease in *Irg1* gene expression in Mϕ within lung tumors during the progression of mouse lung tumors. This observation is consistent with our *in vitro* results and with Michelucci et al. (Michelucci, Cordes et al. 2013), who suggest that *IRG1* gene expression follows a bell-shaped kinetic pattern during the course of Mϕ inflammatory responses. Specifically, *IRG1* and itaconate levels are elevated during the initial inflammatory phase, from the first 2 to 4 hours after LPS stimulation up to 8 to 10 hours, before gradually decreasing during the resolution phase, when Mϕ tend to adopt tumor-friendly phenotypes (Michelucci, Cordes et al. 2013)**.** Along the same lines, our *in vitro* results from IRG1-deficient human and mouse Mϕ exhibit properties that promote tumor growth while showing an anti-inflammatory profile. These observations strongly suggest that the absence of IRG1 in Mϕ supports a tumor-friendly TME. Furthermore, the increased tumor burden in *Irg1*$^{-/-}$, Kras/*Irg1*$^{-/-}$ mice and especially in the orthotopic lung tumor model in WT mice with transplanted Irg1-deficient bone marrow cells underscores the anti-tumor role of Irg1-expressing cells, particularly Mϕ, which play an important role in lung tumorigenesis (Schmall, Al-Tamari et al. 2015). Overall, the anti-tumor phenotype of IRG1-expressing Mϕ in conjunction with the relatively low expression of *IRG1* in lung tumors and its decreasing expression during inflammatory responses and lung tumor progression suggest that IRG1 expression and itaconate production increase during the initial stages of tumor development, a period in which TAMs exhibit anti-tumor phenotypes (Singhal, Stadanlick et al. 2019). However, as the tumor progresses and goes through its various stages, there is a clear shift. IRG1 expression and itaconate production begin to decline. This decline correlates with a change in the phenotype of TAMs, which transition from predominantly antitumor properties to tumor-friendly Mϕ with anti-inflammatory phenotypes.

While these observations provide valuable insights into the tumor-inhibitory effects of IRG1/itaconate in lung cancer, the precise mechanisms responsible for the downregulation of IRG1 during inflammatory responses and tumor progression remain to be further investigated. However, two recent studies shed light on how the production

of IRG1 and itaconate can be inhibited in Mϕ during an immune response. Azzimato et. al. have shown that IRG1 mRNA levels are reduced in the liver of Mϕ in obese humans and in mouse models of obesity-induced insulin resistance. In addition, itaconate levels were also lower in the liver of obese humans and mice compared to healthy groups (Azzimato, Chen et al. 2021). Transcriptome and *in silico* analysis revealed that microRNA(miR)-144 is responsible for the downregulation of IRG1 expression in Mϕ. Further experiments showed that miR-144 is the key factor that modulates TCA metabolism and antioxidant defense in Mϕ mainly by downregulating IRG1 and itaconate, which in turn affects the activity of fumarate hydratase and NRF2 protein as a master regulator of antioxidant defense (Azzimato, Chen et al. 2021).

These data suggest that miR-144 or similar mechanisms may be involved in the downregulation of IRG1 and itaconate in TAMs during lung cancer progression. In another study by Chen et al, it was found that among the numerous compounds that share similarities with cis-aconitate, the substrate of cis-aconitase, the enzyme encoded by the *IRG1* gene, citraconate is the only endogenous inhibitor of IRG1/cis-aconitase activity, with no effect on IRG1 mRNA levels. They found that citraconate can bind directly to cis-aconitase and acts as a substrate analog (Chen, Elgaher et al. 2022). As far as the distribution of endogenous citraconate in the tissue is concerned, the lymph nodes in the mice had the highest citraconate content, followed by the kidney and spleen (Winterhoff, Chen et al. 2021) (Duran, Bruinvis et al. 1978). Interestingly, lung tumors showed a higher uptake and metabolism of branched-chain amino acid (BCAA) than normal tissue (Mayers, Torrence et al. 2016). Therefore, it could be plausible that BCAA-derived citraconate inhibits itaconate production in lung tumors to prevent its antitumor functions. This hypothesis needs further investigation as there are no comprehensive data on citraconate levels in lung tumors and its tumor-promoting functions (Duran, Bruinvis et al. 1978)**.** Interestingly, lung tumors showed higher uptake and metabolism of BCAA than normal tissues (Mayers, Torrence et al. 2016). Therefore, it may be plausible that citraconate from BCAA inhibits itaconate production in lung tumors to prevent its antitumor functions. This hypothesis needs further investigation as there are no comprehensive data on citraconate levels in lung tumors, nor on its pro-tumor functions.

Our findings regarding the higher lung tumor development under Irg1 ablation in mice alongside with the anti-tumor and antiproliferative functions of itaconate which emphasizing the anti-tumor role of Irg1 in the context of lung cancer may seem surprising when compared to recent studies indicating pro-tumor functions of Irg1 in ovarian, melanoma, colorectal and pancreatic cancer (Weiss, Davies et al. 2018, Zhao, Teng et

al. 2022, Chen, Li et al. 2023). However, it is important to point out that our findings regarding anti-tumor functions of IRG1/itaconate axis are consistent with recent studies that have focused specifically on lung disease. These studies have provided fascinating insights into the role of Irg1 in lung health. Specifically, Irg1-deficient mice have been shown to exhibit an increased presence of anti-inflammatory Mϕ and an immunosuppressive phenotype in lung tissue that resembles the phenotype of pro-tumor Mϕ. This suggests that the function of Irg1 in the context of lung disease may differ from its role in other cancers. In addition, these lung-focused studies have revealed the susceptibility of Irg1-deficient mice to lung cancer-associated complications such as pulmonary fibrosis and impaired mucociliary clearance, which may ultimately contribute to the development of chronic obstructive pulmonary disease (COPD) (Ogger, Albers et al. 2020, Zeng, Song et al. 2023). Accordingly, Ogger et al. demonstrated a reduction of itaconate in bronchoalveolar lavage and a downregulation of Irg1 expression in alveolar macrophages in patients with idiopathic pulmonary fibrosis (IPF) compared to control subjects (Ogger, Albers et al. 2020). In support of this, they also showed that itaconate was not only able to reduce pulmonary fibrosis in mice, but also reduced the proliferation of lung fibroblasts and wound healing *in vitro*. In addition, they found a pro-fibrotic and anti-inflammatory phenotype in Irg1-deficient Mϕ isolated from mouse lungs after bleomycin-induced pulmonary fibrosis (Ogger, Albers et al. 2020). This may support the antitumor functions of IRG1/itaconate based on the association of lung cancer and IPF as evidenced by the higher incidence of lung cancer in pulmonary fibrosis patients and the poorer prognosis and shorter survival of lung cancer patients with IPF (Abu Qubo, Numan et al. 2022)**.** In another study by Zeng et al. Itaconate was introduced as a signaling molecule that can bind 2-Oxoglutarate receptor 1 (OXGR1 also called GPR99) to induce Ca2+ mobilization and ERK phosphorylation, leading to mucus secretion and transport in the airway epithelium. Accordingly, they showed that itaconate/OXGR1 enhances mucociliary clearance as the primary innate barrier mechanism of the airway epithelium (Zeng, Song et al. 2023). Impaired mucociliary clearance makes the lungs more susceptible to damage, while either excessive mucus production or impaired mucus clearance plays a role in the development of various respiratory diseases, including asthma, COPD and cystic fibrosis (CF), which are associated with lung cancer (Zeng, Song et al. 2023), particularly in COPD (Durham and Adcock 2015). This discovery is significant because, similar to our own findings, it has shown that itaconate is not only released into the extracellular environment but also triggers signaling pathways that facilitate the interplay between immune cells responsible for itaconate secretion and epithelial cells that take up itaconate. In this context, Jaiswal et al. also reported that Irg1-deficient mice are more susceptible to allergic asthma, which is

associated with increased production of Th2 cytokines, including IL4 and IL13, culminating in an anti-inflammatory, pro-tumor Mϕ phenotype (Jaiswal, Yadav et al. 2022). Overall, Irg1-deficient mice showed a more tumor-friendly and anti-inflammatory Mϕ phenotype in lung tissue under various pathological conditions. However, this complex scenario highlights the distinct biological functions of IRG1 in different organs that need to be further explored, especially in light of recent evidence pointing to mitochondrial oxidative phosphorylation-related pathways as the primary differentiating factor between Mϕ from different organs (Wculek, Heras-Murillo et al. 2023).

5.2 Anti-tumor functions of itaconate/Octyl Ita in lung cancer

Itaconate and its derivatives, such as Octyl Ita, have been used primarily to investigate the underlying mechanisms of the biological functions of IRG1 (O'Neill and Artyomov 2019). However, recent studies emphasizing the tumor-promoting aspects of Irg1 raise the crucial questions: Does supplementation or injection of itaconate or Octyl Ita actually accelerate tumor progression in mouse models using WT mice? Furthermore, can the addition of itaconate promote tumor growth in mice lacking Irg1? In our study, we were able to validate the anti-tumor functions of Irg1 by demonstrating the anti-tumor properties of itaconate and Octyl Ita in human and mouse lung tumor models. Our results are consistent with previous research showing that dimethyl itaconate and Octyl Ita also exhibit antitumor effects in colorectal and ovarian cancers, respectively (Wang, Li et al. 2020, Zhan, Wang et al. 2022), contradicting other studies indicating pro-tumor functions of Irg1 in ovarian and colon cancers (Weiss, Davies et al. 2018, Chen, Li et al. 2023). This may be related to the different properties of itaconate derivative and natural itaconate produced by Irg1, in particular their immunomodulatory functions, as itaconate is reported as an enhancing factor for IFNβ production, while Octyl Ita reduces its level (Swain, Bambouskova et al. 2020). Furthermore, the exact endogenous itaconate level in all cancers is unknown, which may differ from the exogenous itaconate concentration used as a therapeutic approach. Finally, it may be plausible that IRG1 has another function independent of itaconate production. We found that the anti-tumor functions of itaconate and Octyl Ita are not only related to their potential functions to reprogram pro-tumor Mϕ to anti-tumor Mϕ, but also to their direct anti-proliferative effects on lung cancer cells. Interestingly, in agreement with our results, Runtsch et al. have shown that itaconate and Octyl Ita suppress anti-inflammatory Mϕ *in vitro* and in the *in vivo* asthma mouse model, thereby reducing the severity of asthma in mice (Runtsch, Angiari et al. 2022). They attributed the downregulation of anti-inflammatory markers in Mϕ to the inhibition of JAK/STAT1 signaling by Octyl Ita/itaconate through inhibition of JAK kinase activity via direct modification of cysteine residues (Runtsch, Angiari et al. 2022). This

finding not only supports Jaiswal et al. who demonstrated a higher susceptibility of Irg1-deficient mice to allergic asthma (Jaiswal, Yadav et al. 2022), but also our finding that Octyl Ita and itaconate can reprogram anti-inflammatory M2-like Mϕ into a pro-inflammatory M1-like phenotype. Furthermore, our results complement those of the investigators by identifying G6PD as responsible for the upregulation of pro-inflammatory markers upon treatment with Octyl Ita in anti-inflammatory (pro-tumor) Mϕ.

5.3 Anti-proliferative effects of itaconate/Octyl Ita

Regarding the antiproliferative effect of itaconate, Ogger et al. pointed out the antiproliferative effect of itaconate on fibroblasts in the context of pulmonary fibrosis (Ogger, Albers et al. 2020). Interestingly, although Zhao et al. reported the tumor-promoting effect of Irg1 in melanoma, they also noted the proliferation-inhibitory effect of itaconate on both $CD4^+$ and $CD8^+$ T cells, suggesting a general proliferation-inhibitory property of itaconate, as we observed in lung tumors (Zhao, Teng et al. 2022). The direct antiproliferative effect of itaconate and Octyl Ita on cancer cells in conjunction with the lack of IRG1 and itaconate expression in epithelial cells underscores the importance of extracellular/secreted itaconate in the metabolic interplay between Mϕ and cancer cells (Zheng, Mansouri et al. 2020). Although most studies have focused on the cell-autonomous functions of intracellular itaconate, particularly within immune cells, our and other data suggest that Mϕ may also secrete itaconate into the extracellular environment (Strelko, Lu et al. 2011, Lampropoulou, Sergushichev et al. 2016, Zeng, Song et al. 2023). To support this notion, very recently, it has been discovered that itaconate can be exported in Mϕ from cytosol to extracellular environment by ATP-binding cassette transporter G2 (ABCG2) in an ATPase-dependent manner. Interestingly, depletion of ABCG2 can lead to enhancement of lysosomal biogenesis and antibacterial innate immunity response in Mϕ (Chen, Zhang et al. 2024).

Although the Octyl Ita concentration used in this study (250 µM) falls within the range detected in CM of human anti-tumor Mϕ (66 µM - 400 µM), we did not observe the antiproliferative effect of itaconic acid at concentrations below 2 mM. This discrepancy could be due to the relationship between the functions of itaconic acid, its cellular transport and the extracellular acidity of the environment. The pH adjustment normally applied to itaconic acid prior to in vitro and in vivo experiments may interfere with these interactions (Hersch and Navarre 2020, Duncan, Lupien et al. 2021). Accordingly, Duncan et al. have indicated that an acidic environment corresponding to the conditions typically found in Mϕ, including in TME (Kato, Ozawa et al. 2013), significantly increases the antibacterial efficacy of itaconate. One theory for the synergy between the antibacterial function of itaconate and the acidic environment could be related to the

increased activity of dicarboxylate and/or monobasic dicarboxylate transporters at lower pH (Sa-Pessoa, Paiva et al. 2013). For example, the transporter for acetate and succinate, which has a similar structure to itaconate, is most functional at lower pH values. This may also explain the discrepancy between the functions of Irg1 in lung cancer and other tumors, as the TME acid rate may be different in different tumors, which needs to be investigated in further studies. Furthermore, we cannot exclude the possibility that itaconate/OXGR1 signaling may play a role in cancer cells and Mϕ. However, our current results regarding the direct inhibitory effect of itaconate on G6PD activity emphasize the importance of its intracellular entry, where it can directly bind to G6PD independently of receptor-ligand interaction, including OXGR1. Nevertheless, the mechanisms controlling the transport of itaconate from the extracellular to the intracellular environment and vice versa remain important unanswered questions in the biology of itaconate.

5.4 Inhibition of G6PD activity by itaconate/Octyl Ita

Mechanistically, we have shown for the first time that the antiproliferative and immunomodulatory functions of IRG1/Itaconate and Octyl Ita are associated with the inhibitory effect on G6PD activity and the subsequent modulation of PPP metabolism as a major factor of oxidative stress response and DNA/RNA synthesis (Stincone, Prigione et al. 2015). We were able to confirm the essential role of G6PD in mediating the proliferation-inhibiting effect of itaconate. This was evidenced by the observation that cancer cells lacking G6PD showed a similar proliferation rate before and after treatment with Octyl Ita. Furthermore, we were able to attenuate the proliferation-inhibiting effect of Octyl Ita by adding downstream metabolites of G6PD in PPP metabolism to the cancer cells. The proliferation inhibitory effect of G6PD inhibition is mainly related to the direct G6PD products, 6-phosphogluconate (6GP) and NADPH (Stanton 2012). Accordingly, 6PG is an intermediate in PPP metabolism, where it is catalyzed by 6-phosphogluconate dehydrogenase (6PGD) to form ribulose-5-phosphate, which serves as a crucial building block for DNA/RNA synthesis (Patra and Hay 2014). NADPH has a key function as a primary intracellular reducing agent in the reduction of biomolecules, including the formation of reduced glutathione, de novo nucleotide synthesis and the production of fatty acids (Tian, Braunstein et al. 1998). Therefore, G6PD is essential for cell growth and proliferation by modulating ROS levels and maintaining ribose 5-phosphate levels as a downstream product of PPP and precursor of ribonucleotides involved in DNA/RNA synthesis. Higher expression of G6PD was associated with advanced stage of lung tumor, lymph node metastasis, less tumor differentiation, pleural invasion, vascular invasion and lymphatic invasion. In addition, lung cancer patients who tested positive for

G6PD in tumor tissue had significantly poorer overall survival than patients who were G6PD-negative (Nagashio, Oikawa et al. 2019). In addition to the regulation of G6PD at the mRNA and protein level, mutations in the G6PD gene are the most common enzymatic abnormalities in humans. G6PD mutations lead to fragile RBCs, but also provide some protection against malaria (Luzzatto, Ally et al. 2020). The highest population incidence of G6PD deficiency is reported mainly from Africa and some parts of Asia (Luzzatto, Ally et al. 2020). This is interesting because the most common missense polymorphism of human IRG1 has an allele frequency of 19.7% in genomes of African and African-American ancestry and is not detected in other populations. This mutation replaces Asn152, a residue near the active site of CAD, with serine, resulting in a 50% increase in CAD enzyme and itaconate production (Chen, Lukat et al. 2019). It is therefore plausible that people with this IRG1 mutation have low G6PD activity and protection against cancer and malaria. This is all the more likely as these two phenomena have been observed in the same human ethnic group as Africans. However, further studies are needed to investigate cancer and other immune-related diseases in African people with IRG1 mutations. Our in silico analysis shows that itaconate can bind directly to the G6PD binding pocket, effectively suppressing its maximal activity. Chemoproteomic profiling has shown that the itaconate derivative known as Itaconate-alkyne (ITalk) can alter the G6PD protein through a cysteine modification at residue 385, mutation of which leads to a loss of function (Lee, Park et al. 2017) (Qin, Zhang et al. 2020). The same group also pointed out that the cysteine modification of G6PD can be influenced by electrophilic ligands, including itaconate. They also demonstrated that itaconate-associated cysteine modifications on glycolytic enzymes inhibit their activity and rate of glycolysis in (Qin, Qin et al. 2019). Therefore, the inhibitory effects of IRG1/itaconate and Octyl Ita on G6PD activity can be attributed to post-translation modification at cysteine residues of the G6PD protein. In the same direction. It has been shown that G6PD activity can be regulated by the NAD-dependent deacetylase sirtuin 2 (SIRT2), which deacetylates lysine 403 (K403), leading to a rapid increase in G6PD activity and stimulating PPP in response to oxidative stress. After the disappearance of oxidative stress, G6PD K403 is again acetylated, leading to a decrease in its activity to the normal baseline level (Wang, Zhou et al. 2014). In addition, Rao et. al. found O-linked β-N-acetylglucosamine (O-GlcNAc) as a posttranslational modification on the G6PD protein in cancer cells. They showed that O-GlcNAcylation of G6PD increases its enzymatic activity and promotes increased glucose flux through PPP metabolism (Rao, Duan et al. 2015). This in turn generates important precursors for nucleotide and lipid biosynthesis and at the same time provides the necessary reducing equivalents for antioxidant defense mechanisms. They were able to show that glycosylation of G6PD

not only induces cancer cell proliferation in vitro, but also accelerates tumor growth in vivo, primarily by orchestrating anabolic biosynthesis and maintaining the redox balance of cancer cells. Of particular note, they were able to demonstrate the increase in G6PD glycosylation observed in human lung cancer (Rao, Duan et al. 2015). Together with our results, these data indicate that post-translational modification of G6PD, which is faster than a transcription-based regulatory mechanism, may be more functional for the acute immune response, including for plastic cells, including Mϕ, which should rapidly change their phenotype based on extracellular stimuli. In addition, Octyl Ita is known for its ability to activate NRF2 through cysteine modification of KEAP1 in activated Mϕ (Mills, Ryan et al. 2018). NRF2 in turn regulates the transcription of genes, including G6PD, which play a crucial role in pentose PPP metabolism and in the cellular response to oxidative stress (Mitsuishi, Taguchi et al. 2012). Interestingly, in our study, we did not observe activation of NRF2 or upregulation of genes related to PPP metabolism when examining cancer cells both after overexpression of IRG1 and after treatment with Octyl Ita. Sun et al. have also shown that endogenous itaconate produced by Irg1 is not necessary for NRF2 activation (Sun, Li et al. 2020). However, we observed an increase in the expression of genes related to the cellular response to oxidative stress. This finding suggests the presence of an NRF2-independent mechanism driving the upregulation of oxidative stress-responsive genes in this context.

Notably, G6PD-deficient cancer cells displayed an elevation in the expression of HMOX1, a marker of the oxidative stress response (Gozzelino, Jeney et al. 2010). Surprisingly, Octyl Ita did not induce the expression of HMOX1 in G6PD-deficient cancer cells. This suggests that the ability of Octyl Ita to modulate the response to oxidative stress in cancer cells is dependent on its modification of G6PD, which consequently modulates HMOX1 expression. However, this could be a compensatory mechanism by which the cells attempt to compensate for the oxidative stress induced by the lack of G6PD through HMOX1. Further studies can explore whether this is directly linked to the ROS level or if there is a direct interaction between G6PD and HMOX1. Thus, the influence of Octyl Ita on NRF2 activation and oxidative stress response appears to be context-specific, with an NRF2-independent mechanism operating in cancer cells. This mechanism probably involves the modification of G6PD, which highlights the complex interplay between Octyl Ita, G6PD and the regulation of oxidative stress in cancer cells. A remarkable result of our study is the different response of cancer cells and pro-tumor Mϕ to treatment with Octyl Ita. In pro-tumor Mϕ, Octyl Ita treatment leads to activation of NRF2, accompanied by an increase in the expression of genes involved in PPP metabolism and cellular response to oxidative stress. In contrast, cancer cells under

Octyl Ita treatment show neither NRF2 activation nor upregulation of genes related to PPP metabolism and oxidative stress response. Interestingly, the induction of HMOX1 heme oxygenase 1 by Octyl Ita in Mϕ appears to be independent of G6PD, as shown in a study by Millis et al. (Mills, Ryan et al. 2018). One possible explanation for this discrepancy lies in the different inflammatory and oxidative states of these cell types; the microenvironments within cancer cells and pro-tumor Mϕ may have a significant impact on how Octyl Ita influences cellular oxidative responses. Accordingly, Swain et al. demonstrated that the presence of inflammatory and oxidative conditions is a critical factor for significant NRF2 induction by IRG1/itaconate and its various derivatives (Swain, Bambouskova et al. 2020). Our results highlight the complex interactions between itaconate, NRF2 activation, G6PD and the cellular response to oxidative stress in different cell types, with different inflammatory and oxidative conditions and reveal that how Octyl Ita and related signaling pathways influence the cellular oxidative response.

Overall, these novel inhibitory effects of IRG1/itaconate and Octyl Ita on G6PD activity and PPP metabolism have important implications. They not only suppress cancer cell proliferation in a non-cell-autonomous manner, but also reprogram pro-tumor Mϕ into an anti-tumor phenotype in a cell-autonomous manner. Our results demonstrate the critical role of G6PD in promoting the polarization of pro-tumor Mϕ. This is consistent with recent research showing that inhibition of PPP in Mϕ not only induces a pro-inflammatory Mϕ state, but also enhances anti-tumor treatment in lymphoma mouse models (Beielstein, Izquierdo et al. 2023). With regard to the tumor-promoting functions of G6PD, promising data from preclinical animal models are available. These data show that the use of different and novel G6PD inhibitors not only reduces the primary tumor growth and the metastasis rate in various types of cancer (Mele, Paino et al. 2018, Bose, Huang et al. 2022, Koperniku, Garcia et al. 2022).

6. Outlook

While there have been promising novel therapeutic approaches in lung cancer treatment, it remains the leading cause of cancer-related deaths. Consequently, there is an urgent imperative to not only discover new therapeutic strategies but also enhance existing treatments, particularly immunotherapy regimens. This study highlights the significant anti-tumor potential of the IRG1/itaconate axis in lung cancer and suggests its applicability as an innovative therapeutic option. However, it also prompts the emergence of new inquiries that demand deeper exploration, aiming not only to understand the role of TAMs metabolism in lung cancer development but also to identify potential directions for future research.

Given the observed changes in the phenotype of TAMs resulting from depletion of Irg1 and treatment with Octyl Ita in preclinical lung cancer models, it is imperative that future studies investigate the effects of the IRG1/Itaconate axis on other cellular components within the lung TME, with particular focus on the T cell population. Consistent with this line of research and with the goal of improving the efficacy of immunotherapy regimens for lung cancer patients, exploration of combination therapies with octyl-Ita and immunologic ICI drugs such as nivolumab, a PD-1 inhibitor, deserves attention, considering the metabolic regulatory functions of ICI regimens in the context of lung cancer patients.

To elucidate the role of itaconate as a metabolite messenger involved in crosstalk between Mϕ and cancer cells and other components of the TME, it is valuable to investigate the development of lung tumors under ablation of ABCG1, the only known and novel itaconate transporter, specifically in the Mϕ population in lung cancer mouse models.

While IRG1 gene expression in human lung cancer is not detected in the TCGA dataset, comprehensive studies on potential IRG1 mutations are lacking. This represents an interesting area of research, particularly given the relatively high frequency of gain-of-function IRG1 mutations in African populations. Therefore, it is worthwhile to conduct follow-up studies in individuals of African descent carrying IRG1 mutations to determine the incidence rate of lung cancer and other cancers. In addition, examining G6PD activity status in individuals with higher IRG1 activity and the presence of G6PD-associated diseases, including malaria and favism, could provide interesting insights. Finally, future studies could look for IRG1 mutations not only in cancer cells, but also in immune cell populations that are the major contributors to IRG1 expression.

Considering the important functional role of G6PD in the spread of lung cancer, future studies should investigate the role of G6PD in lung tumors with different genetic landscapes, especially in cases where metabolism-associated genes are mutated, such as Liver Kinase B1 (LKB1) and KEAP1. This research should include not only cancer cells but also immune cells, as G6PD plays an immunomodulatory role.

Finally, it is worthwhile to investigate the role of the IRG1/itaconate axis and downstream targets, including G6PD, in lung cancer-associated diseases such as pulmonary fibrosis, pulmonary hypertension and COPD, considering the inflammatory nature of some of these diseases.

7. Summary

TAMs use different nutrients in different metabolic pathways to support their function during tumor development. Although there has been some progress in understanding TAM metabolism, the involvement of TAM metabolism in tumor growth and especially in the immune response to the tumor remains unexplored. A recent discovery is the metabolite itaconate, which plays an important role in immune regulation during inflammatory responses. Itaconate is mainly produced by anti-tumor M1-like Mϕ. However, its role in lung cancer development is still largely unexplored. In this study, we have shown that mice lacking Irg1 as source of itaconate are more susceptible to lung cancer development. The proliferation rate was significantly increased in Irg1-deficient lung tumors. Our scRNA-seq analysis of human and mouse lung tumors identified Mϕ as the primary immune cells responsible for Irg1 expression. Accordingly, transplantation of Irg1-deficient bone marrow cells into wild-type mice supported the anti-tumor function of Irg1 findings, as recipient mice of Irg1-deficient bone marrow cells exhibited a higher incidence of lung tumors. The absence of Irg1 in the bone marrow cells not only led to a higher proliferation rate, but also to an increased presence of pro-tumor Mϕ in the lung tumors. Considering itaconate as the main product of IRG1, we showed that Octyl Ita, a permeable form of itaconate, reduced lung tumor formation in various lung cancer mouse models in vivo by decreasing tumor proliferation rates and inducing an anti-tumor phenotype in TAMs. Interestingly, application of Octyl Ita in human tPCLS, a novel human ex vivo system, also resulted in decreased cancer cell proliferation and a shift of TAMs towards an anti-tumor phenotype. We have also shown that the proliferation inhibitory effect of Octyl Ita/itaconate can be recapitulated in various lung cancer cell lines in vitro.

To uncover the underlying mechanisms of the antiproliferative properties of octyl-Ita, metabolomic analysis of A549 lung cancer cells revealed a significant down-regulation of PPP metabolism upon Octyl Ita treatment. Further transcriptomic and proteome analysis revealed dysregulation of metabolic pathways related to PPP metabolism, including oxidative stress response. In addition, we identified G6PD as the major target of Octyl Ita/itaconate in PPP metabolism. Octyl Ita/Itaconate can directly bind to G6PD and inhibit its activity without affecting its mRNA and protein levels. Interestingly, Octyl Ita loses its antiproliferative functions in G6PD-deficient cancer cells. Conversely, the antiproliferative function of Octyl Ita is restored when cancer cells are supplemented with downstream G6PD metabolites. We found that Octyl Ita can reprogram pro-tumoral Mϕ into anti-tumoral Mϕ by downregulating PPP metabolism and reducing G6PD activity. Transcriptomic and proteomic analysis have also demonstrated the effects of Octyl Ita

treatment on signaling pathways associated with PPP metabolism in pro-tumor Mϕ. However, our analysis suggests that G6PD is only partially involved in the anti-tumor function of Octyl Ita in pro-tumor Mϕ. We also showed that IRG1 is essential for the anti-tumor function of Mϕ, as depletion of IRG1 enhances the pro-tumor phenotype and functions in anti-tumor Mϕ.

Finally, our study showed that ablation of Irg1 leads to increased G6PD activity in mouse lung tumors, while treatment with Octyl Ita reduces G6PD activity in mice with lung tumors. Higher G6PD activity was found in human lung tumors compared to normal tissue. Similarly, increased G6PD mRNA expression has shown a negative correlation with survival of lung cancer patients. In conclusion, our findings suggest that Octyl Ita possesses significant potential as an antitumor metabolite with potential therapeutic applications in the treatment of lung cancer. It not only inhibits the proliferation of cancer cells, but also induces an anti-tumor phenotype within tumor microenvironment, providing a promising avenue for further research and development of lung cancer treatment.

8. Zusammenfassung

Tumor- assoziierte Makrophagen (TAMs) nutzen verschiedene Nährstoffe in unterschiedlichen Stoffwechselwegen, um ihre Funktion während der Tumorentwicklung zu unterstützen. Obwohl es einige Fortschritte im Verständnis des TAM-Stoffwechsels gibt, ist dessen Beteiligung am Tumorwachstum und insbesondere der Immunantwort auf den Tumor noch weitestgehend unerforscht. Eine neuere Entdeckung diesbezüglich ist Itaconat (Ita), ein Metabolit, der eine wichtige Rolle bei der Immunregulierung während Entzündungsreaktionen spielt. Itaconat wird hauptsächlich von pro-inflammatorischen M1-ähnlichen Makrophagen (Mϕ) produziert, die gegen den Tumor gerichtet sind. Die Rolle von Itaconat bei der Entwicklung von Lungenkrebs ist jedoch noch weitgehend unerforscht. In dieser Studie haben wir gezeigt, dass Mäuse, denen das Immunoresponsive gene 1 (Irg1) und somit auch dessen Produkt Itaconat fehlt, anfälliger für die Entwicklung von Lungenkrebs sind. Die Proliferationsrate war in Irg1-defizienten Lungentumoren deutlich erhöht. Unsere scRNAseq-Analyse von Humanen - und Maus-Lungentumoren identifizierte Mϕ als die primären Immunzellen, die für die Irg1-Expression verantwortlich sind. Dementsprechend unterstützte die Transplantation von Irg1-defizienten Knochenmarkzellen in Wildtyp-Mäuse die Irg1 vermittelte Anti-Tumorfunktion, da Empfänger-Mäuse mit Irg1-defizienten Knochenmarkzellen eine höhere Inzidenz von Lungentumoren aufwiesen. Das Fehlen von Irg1 in den Knochenmarkzellen führte nicht nur zu einer höheren Proliferationsrate, sondern auch zu einer erhöhten Präsenz von protumoralen Mϕ in den Lungentumoren. In Anbetracht von Itaconat als Hauptprodukt von IRG1 konnten wir zeigen, dass Octyl-Ita, eine durchlässige Form von Itaconat, die Bildung von Lungentumoren in verschiedenen Lungenkrebs-Mausmodellen *in vivo* reduzierte, indem es die Tumorproliferationsraten verringerte und einen antitumoralen Phänotyp in TAMs induzierte. Interessanterweise führte die Anwendung von Octyl-Ita in menschlichen Tumor-Gewebeschnitten „Precision-Cut Lung Slices“ (TPCLS), einem neuartigen menschlichen Ex-vivo-System, ebenfalls zu einer verringerten Proliferation von Krebszellen und zu einer Verschiebung der TAMs in Richtung eines antitumoralen Phänotyps. Zusätzlich konnten wir die proliferationshemmende Wirkung von Octyl-Ita/Itaconat in verschiedenen Lungenkrebszelllinien *in vitro* zeigen.

Um die den antiproliferativen Eigenschaften von Octyl-Ita zugrundeliegenden Mechanismen aufzudecken, ergab die Metabolomanalyse von A549-Lungenkrebszellen eine signifikante Herabregulierung des PPP-Stoffwechsels bei der Behandlung mit Octyl-Ita. Weitere Transkriptom- und Proteomanalysen zeigten eine Dysregulation von Stoffwechselwegen, die mit dem Pentosephosphatweg (PPP) zusammenhängen,

einschließlich der Reaktion auf oxidativen Stress. Darüber hinaus identifizierten wir G6PD als das Hauptziel von Octyl-Ita/Itaconat im PPP-Stoffwechsel. Octyl-Ita/Itaconat kann direkt an G6PD binden und dessen Aktivität hemmen, ohne dessen mRNA- und Proteingehalt zu beeinflussen. Interessanterweise verliert Octyl-Ita seine antiproliferativen Funktionen in G6PD-defizienten Krebszellen. Umgekehrt wird die antiproliferative Funktion von Octyl-Ita wiederhergestellt, wenn die Krebszellen mit nachgeschalteten G6PD-Metaboliten ergänzt werden. Wir konnten zeigen, dass Octyl-Ita protumorale Mϕ in antitumorale Mϕ umprogrammieren konnte, indem der PPP-Stoffwechsel herunterreguliert und die G6PD-Aktivität reduziert wurde. Transkriptom- und Proteomanalysen haben auch die Auswirkungen der Octyl-Ita-Behandlung auf Signalwege gezeigt, die mit dem PPP-Stoffwechsel in protumoralen Mϕ verbunden sind. Unsere Analyse legt jedoch nahe, dass G6PD nur teilweise an der Antitumorfunktion von Octyl-Ita in protumoralen Mϕ beteiligt ist. Wir haben zudem gezeigt, dass IRG1 für die Antitumorfunktion von Mϕ essentiell ist, da die von IRG1 den protumoralen Phänotyp und die Funktionen in antitumoralen Mϕ verstärkt.

Wir konnten mit dieser Studie zeigen, dass die Ablation von Irg1 zu einer erhöhten G6PD-Aktivität in Lungentumoren der Maus führte, während die Behandlung mit Octyl-Ita die G6PD-Aktivität in Mäusen mit Lungentumoren reduzierte. In menschlichen Lungentumoren wurde im Vergleich zu normalem Gewebe eine höhere G6PD-Aktivität festgestellt. Darüber hinaus zeigte eine erhöhte G6PD-mRNA-Expression eine negative Korrelation mit der Überlebensrate von Lungenkrebspatienten. Zusammenfassend deuten unsere Ergebnisse darauf hin, dass Octyl-Ita ein erhebliches Potenzial als Antitumor-Metabolit mit möglichen therapeutischen Anwendungen bei Lungenkrebs hat. Es hemmt nicht nur die Proliferation von Krebszellen, sondern induziert auch einen antitumoralen Phänotyp in der Tumormikroumgebung, was einen vielversprechenden Weg für die weitere Forschung und Entwicklung der Lungenkrebsbehandlung darstellt.

9. List of abbreviation

DIPNECH	Diffuse idiopathic pulmonary neuroendocrine cell hyperplasia
AAH	Atypical adenomatous hyperplasia
BAC	Non-mucinous bronchiole alveolar carcinoma
SCLC	Small cell lung carcinoma
NSCLC	Non-small cell lung carcinoma
LUAD	Lung adenocarcinoma
LUSC	Lung squamous cell carcinoma
KRAS	Kirsten rat sarcoma
TP53	Tumor suppressor p53
EGFR	Epidermal growth factor receptor
RTKs	Receptor tyrosine kinases
EML4	Echinoderm microtubule-associated protein-like 4
ALK	Anaplastic lymphoma kinase
SBRT	Stereotactic body radiotherapy
ICI	Immune checkpoint inhibitors
PD-L1	Programmed death ligand 1
PD-1	Programmed cell death protein 1
CTLA-4	Cytotoxic T lymphocyte-associated protein 4
Tregs	Regulatory T cells
IL	Interleukin
TME	Tumor microenvironment
MDSCs	Myeloid-derived suppressor cells
CAF	Cancer-associated fibroblast
DCs	Dendritic cells
TAMs	Tumor-associated macrophages
TANs	Tumor-associated neutrophils
ECM	Extracellular matrix
FASL	FAS ligand

SDF1	Stromal-derived growth factor
CXCL	CXC motif chemokine ligand
ROS	Reactive oxygen species
HIF-1α	Hypoxia-inducible factor 1α
CXCR	CXC chemokine receptors
RNS	Reactive nitrogen species
PGE2	Proteases and prostaglandin E2
MMP9	Matrix metalloproteinase 9
IFN	Interferon
APCs	Antigen-presenting cells
TGF	Tumor growth factor
CCL	C-C motif chemokine ligand
NK	Natural killer
Th1	T helper 1
TNF	Tumor necrosis factor
TRMs	Tissue-derived macrophages
Mϕ	Macrophages
LPS	Lipopolysaccharide
STAT	Signal transducer and activator of transcription
IRF3	Interferon regulatory factor 3
scRNA-seq	Single-cell RNA sequencing
CyTOF	Cytometry by time-of-flight
TCA	Tricarboxylic acid
FAO	Fatty acid oxidation
Itaconate	Itaconic acid
NO	Nitric oxide
ARG	Arginase
GS	Glutamine synthase
MHCII	Major histocompatibility complex class II

ATP	Adenosine triphosphate
TAM-EVs	Extracellular vesicles of TAMs
TXB2	Thromboxane B2
OXPHOS	Oxidative phosphorylation
FDG	18F-fluorodeoxyglucose
CSF1R	Colony stimulating factor 1 receptor
VEGF	Vascular endothelial growth factor
PDGF	Platelet-derived growth factor
mTOR	Mammalian target of rapamycin
REDD1	Regulated in development and DNA damage responses 1
IRG1	Immune responsive gene 1
SDHA	Succinate dehydrogenase A
GAPDH	Glyceraldehyde-3-phosphate dehydrogenase
NRF2	Nuclear factor erythroid 2-related factor 2
ATF3	Activating transcription factor 3
PPARγ	Peroxisome proliferator-activated receptor γ
Octyl Ita	4-octyl-itaconate
JAK1	Janus Kinase 1
ATCC	American Type Culture Collection
FCS	Fetal calf serum
P/S	penicillin/streptomycin
PBMCs	Peripheral blood mononuclear cells
RBCs	Red blood cells
PBS	Phosphate-buffered saline
CM	Conditioned medium
qPCR	Quantitative PCR
LC-MS/MS	Liquid chromatography coupled to tandem mass spectrometry
G6P	D-glucose 6-phosphate
G6PD	Glucose-6-phosphate dehydrogenase

$NADP^+$	β-nicotinamide adenine dinucleotide phosphate hydrate
DHEA	trans-dehydroandrosterone
GSH	Glutathione
GSSG	Oxidized glutathione
tPCLS	tumor precision cut lung slices
H&E	Hematoxylin and Eosin
DEGs	Differentially expressed genes
BM	Bone marrow
BMT	Bone marrow transplantation
SC	Subcutaneous
KEAP1	Kelch-like ECH-associated protein 1
BMDMs	BM derived-macrophages
PPP	Pentose phosphate pathway
NADPH	Nicotinamide adenine dinucleotide phosphate
HMOX1	Heme oxygenase 1
V_{max}	Maximum velocity
K_m	Michaelis constant
BCAA	Branched-chain amino acid
COPD	Chronic obstructive pulmonary disease
IPF	Idiopathic pulmonary fibrosis
OXGR1	2-Oxoglutarate receptor 1
CF	Cystic fibrosis
ABCG2	ATP-binding cassette transporter G2
ITalk	Itaconate-alkyne
SIRT2	NAD-dependent deacetylase sirtuin 2

10. List of figures

11. List of tables

12. References

Abu Qubo, A., J. Numan, J. Snijder, M. Padilla, J. H. M. Austin, K. M. Capaccione, M. Pernia, J. Bustamante, T. O'Connor and M. M. Salvatore (2022). "Idiopathic pulmonary fibrosis and lung cancer: future directions and challenges." Breathe (Sheff) **18**(4): 220147.

Amjad, M. T., A. Chidharla and A. Kasi (2023). Cancer Chemotherapy. StatPearls. Treasure Island (FL) ineligible companies. Disclosure: Anusha Chidharla declares no relevant financial relationships with ineligible companies. Disclosure: Anup Kasi declares no relevant financial relationships with ineligible companies.

Azzimato, V., P. Chen, E. Barreby, C. Morgantini, L. Levi, A. Vankova, J. Jager, A. Sulen, M. Diotallevi, J. X. Shen, A. Miller, E. Ellis, M. Ryden, E. Naslund, A. Thorell, V. M. Lauschke, K. M. Channon, M. J. Crabtree, A. Haschemi, S. M. Craige, M. Mori, F. Spallotta and M. Aouadi (2021). "Hepatic miR-144 Drives Fumarase Activity Preventing NRF2 Activation During Obesity." Gastroenterology **161**(6): 1982-1997 e1911.

Babamohamadi, M., N. Mohammadi, E. Faryadi, M. Haddadi, A. Merati, F. Ghobadinezhad, R. Amirian, Z. Izadi and J. Hadjati (2024). "Anti-CTLA-4 nanobody as a promising approach in cancer immunotherapy." Cell Death Dis **15**(1): 17.

Baghban, R., L. Roshangar, R. Jahanban-Esfahlan, K. Seidi, A. Ebrahimi-Kalan, M. Jaymand, S. Kolahian, T. Javaheri and P. Zare (2020). "Tumor microenvironment complexity and therapeutic implications at a glance." Cell Commun Signal **18**(1): 59.

Beielstein, A. C., E. Izquierdo, S. Blakemore, N. Nickel, M. Michalik, S. Chawan, R. Brinker, H.-H. Bartel, D. Vorholt, J. L. Nolte, R. Linke, C. R. C. Picossi, J. Sáiz, F. Picard, A. Florin, J. Meinel, R. Büttner, A. Villaseñor, H. Winkels, M. Hallek, M. Krüger, C. Barbas and C. P. Pallasch (2023). "Pentose Phosphate Pathway Inhibition activates Macrophages towards phagocytic Lymphoma Cell Clearance." bioRxiv: 2023.2006.2009.543574.

Biswas, S. K. and A. Mantovani (2010). "Macrophage plasticity and interaction with lymphocyte subsets: cancer as a paradigm." Nat Immunol **11**(10): 889-896.

Bolger, A. M., M. Lohse and B. Usadel (2014). "Trimmomatic: a flexible trimmer for Illumina sequence data." Bioinformatics **30**(15): 2114-2120.

Bose, S., Q. Huang, Y. Ma, L. Wang, G. O. Rivera, Y. Ouyang, R. Whitaker, R. A. Gibson, C. D. Kontos, A. Berchuck, R. A. Previs and X. Shen (2022). "G6PD inhibition sensitizes ovarian cancer cells to oxidative stress in the metastatic omental microenvironment." Cell Rep **39**(13): 111012.

Brambilla, E. and A. Gazdar (2009). "Pathogenesis of lung cancer signalling pathways: roadmap for therapies." Eur Respir J **33**(6): 1485-1497.

Cancer Genome Atlas Research, N. (2014). "Comprehensive molecular profiling of lung adenocarcinoma." Nature **511**(7511): 543-550.

Casanova-Acebes, M., E. Dalla, A. M. Leader, J. LeBerichel, J. Nikolic, B. M. Morales, M. Brown, C. Chang, L. Troncoso, S. T. Chen, A. Sastre-Perona, M. D. Park, A. Tabachnikova, M. Dhainaut, P. Hamon, B. Maier, C. M. Sawai, E. Agullo-Pascual, M. Schober, B. D. Brown, B. Reizis, T. Marron, E. Kenigsberg, C. Moussion, P. Benaroch, J. A. Aguirre-Ghiso and M. Merad (2021). "Tissue-resident macrophages provide a pro-tumorigenic niche to early NSCLC cells." Nature **595**(7868): 578-584.

Cassetta, L. and T. Kitamura (2018). "Targeting Tumor-Associated Macrophages as a Potential Strategy to Enhance the Response to Immune Checkpoint Inhibitors." Front Cell Dev Biol **6**: 38.

Chang, C. I., J. C. Liao and L. Kuo (2001). "Macrophage arginase promotes tumor cell growth and suppresses nitric oxide-mediated tumor cytotoxicity." Cancer Res **61**(3): 1100-1106.

Chen, C., Z. Zhang, C. Liu, P. Sun, P. Liu and X. Li (2024). "ABCG2 is an itaconate exporter that limits antibacterial innate immunity by alleviating TFEB-dependent lysosomal biogenesis." Cell Metab.

Chen, E. Y., C. M. Tan, Y. Kou, Q. Duan, Z. Wang, G. V. Meirelles, N. R. Clark and A. Ma'ayan (2013). "Enrichr: interactive and collaborative HTML5 gene list enrichment analysis tool." BMC Bioinformatics **14**: 128.

Chen, F., W. A. M. Elgaher, M. Winterhoff, K. Bussow, F. H. Waqas, E. Graner, Y. Pires-Afonso, L. Casares Perez, L. de la Vega, N. Sahini, L. Czichon, W. Zobl, T. Zillinger, M. Shehata, S. Pleschka, H. Bahre, C. Falk, A. Michelucci, S. Schuchardt, W. Blankenfeldt, A. K. H. Hirsch and F. Pessler (2022). "Citraconate inhibits ACOD1 (IRG1) catalysis, reduces interferon responses and oxidative stress, and modulates inflammation and cell metabolism." Nat Metab **4**(5): 534-546.

Chen, F., P. Lukat, A. A. Iqbal, K. Saile, V. Kaever, J. van den Heuvel, W. Blankenfeldt, K. Bussow and F. Pessler (2019). "Crystal structure of cis-aconitate decarboxylase reveals the impact of naturally occurring human mutations on itaconate synthesis." Proc Natl Acad Sci U S A **116**(41): 20644-20654.

Chen, L. L., C. Morcelle, Z. L. Cheng, X. Chen, Y. Xu, Y. Gao, J. Song, Z. Li, M. D. Smith, M. Shi, Y. Zhu, N. Zhou, M. Cheng, C. He, K. Y. Liu, G. Lu, L. Zhang, C. Zhang, J. Zhang, Y. Sun, T. Qi, Y. Lyu, Z. Z. Ren, X. M. Tan, J. Yin, F. Lan, Y. Liu, H. Yang, M. Qian, C. Duan, X. Chang, Y. Zhou, L. Shen, A. S. Baldwin, K. L. Guan, Y. Xiong and D. Ye (2022). "Itaconate inhibits TET DNA dioxygenases to dampen inflammatory responses." Nat Cell Biol **24**(3): 353-363.

Chen, Y. J., G. N. Li, X. J. Li, L. X. Wei, M. J. Fu, Z. L. Cheng, Z. Yang, G. Q. Zhu, X. D. Wang, C. Zhang, J. Y. Zhang, Y. P. Sun, H. Saiyin, J. Zhang, W. R. Liu, W. W. Zhu, K. L. Guan, Y. Xiong, Y. Yang, D. Ye and L. L. Chen (2023). "Targeting IRG1 reverses the immunosuppressive function of tumor-associated macrophages and enhances cancer immunotherapy." Sci Adv **9**(17): eadg0654.

Chirieac, L. R. and S. Dacic (2010). "Targeted Therapies in Lung Cancer." Surg Pathol Clin **3**(1): 71-82.

Cho, K. R. and B. Vogelstein (1992). "Genetic alterations in the adenoma--carcinoma sequence." Cancer **70**(6 Suppl): 1727-1731.

Cianciaruso, C., T. Beltraminelli, F. Duval, S. Nassiri, R. Hamelin, A. Mozes, H. Gallart-Ayala, G. Ceada Torres, B. Torchia, C. H. Ries, J. Ivanisevic and M. De Palma (2019). "Molecular Profiling and Functional Analysis of Macrophage-Derived Tumor Extracellular Vesicles." Cell Rep **27**(10): 3062-3080 e3011.

Coffelt, S. B., M. D. Wellenstein and K. E. de Visser (2016). "Neutrophils in cancer: neutral no more." Nat Rev Cancer **16**(7): 431-446.

Coley, W. B. (1991). "The treatment of malignant tumors by repeated inoculations of erysipelas. With a report of ten original cases. 1893." Clin Orthop Relat Res(262): 3-11.

Cruzat, V., M. Macedo Rogero, K. Noel Keane, R. Curi and P. Newsholme (2018). "Glutamine: Metabolism and Immune Function, Supplementation and Clinical Translation." Nutrients **10**(11).

Crystal, R. G., S. H. Randell, J. F. Engelhardt, J. Voynow and M. E. Sunday (2008). "Airway epithelial cells: current concepts and challenges." Proc Am Thorac Soc **5**(7): 772-777.

Denissenko, M. F., A. Pao, M. Tang and G. P. Pfeifer (1996). "Preferential formation of benzo[a]pyrene adducts at lung cancer mutational hotspots in P53." Science **274**(5286): 430-432.

Deryugina, E. I., E. Zajac, A. Juncker-Jensen, T. A. Kupriyanova, L. Welter and J. P. Quigley (2014). "Tissue-infiltrating neutrophils constitute the major in vivo source of angiogenesis-inducing MMP-9 in the tumor microenvironment." Neoplasia **16**(10): 771-788.

Dobin, A., C. A. Davis, F. Schlesinger, J. Drenkow, C. Zaleski, S. Jha, P. Batut, M. Chaisson and T. R. Gingeras (2013). "STAR: ultrafast universal RNA-seq aligner." Bioinformatics **29**(1): 15-21.

Duan, Q., H. Zhang, J. Zheng and L. Zhang (2020). "Turning Cold into Hot: Firing up the Tumor Microenvironment." Trends Cancer **6**(7): 605-618.

Dumitriu, I. E., D. R. Dunbar, S. E. Howie, T. Sethi and C. D. Gregory (2009). "Human dendritic cells produce TGF-beta 1 under the influence of lung carcinoma cells and prime

the differentiation of CD4+CD25+Foxp3+ regulatory T cells." J Immunol **182**(5): 2795-2807.

Duncan, D., A. Lupien, M. A. Behr and K. Auclair (2021). "Effect of pH on the antimicrobial activity of the macrophage metabolite itaconate." Microbiology (Reading) **167**(5).

Duran, M., L. Bruinvis, D. Ketting and S. K. Wadman (1978). "Deranged isoleucine metabolism during ketotic attacks in patients with methylmalonic acidaemia." J Inherit Metab Dis **1**(3): 105-107.

Durham, A. L. and I. M. Adcock (2015). "The relationship between COPD and lung cancer." Lung Cancer **90**(2): 121-127.

Eruslanov, E. B., P. S. Bhojnagarwala, J. G. Quatromoni, T. L. Stephen, A. Ranganathan, C. Deshpande, T. Akimova, A. Vachani, L. Litzky, W. W. Hancock, J. R. Conejo-Garcia, M. Feldman, S. M. Albelda and S. Singhal (2014). "Tumor-associated neutrophils stimulate T cell responses in early-stage human lung cancer." J Clin Invest **124**(12): 5466-5480.

Feng, Y., S. Renshaw and P. Martin (2012). "Live imaging of tumor initiation in zebrafish larvae reveals a trophic role for leukocyte-derived PGE(2)." Curr Biol **22**(13): 1253-1259.

Ferrer, I., J. Zugazagoitia, S. Herbertz, W. John, L. Paz-Ares and G. Schmid-Bindert (2018). "KRAS-Mutant non-small cell lung cancer: From biology to therapy." Lung Cancer **124**: 53-64.

Fridman, W. H., F. Pages, C. Sautes-Fridman and J. Galon (2012). "The immune contexture in human tumours: impact on clinical outcome." Nat Rev Cancer **12**(4): 298-306.

Fukumura, D., R. Xavier, T. Sugiura, Y. Chen, E. C. Park, N. Lu, M. Selig, G. Nielsen, T. Taksir, R. K. Jain and B. Seed (1998). "Tumor induction of VEGF promoter activity in stromal cells." Cell **94**(6): 715-725.

Ganesan, A. P., M. Johansson, B. Ruffell, A. Yagui-Beltran, J. Lau, D. M. Jablons and L. M. Coussens (2013). "Tumor-infiltrating regulatory T cells inhibit endogenous cytotoxic T cell responses to lung adenocarcinoma." J Immunol **191**(4): 2009-2017.

Ganta, V. C., M. H. Choi, A. Kutateladze, T. E. Fox, C. R. Farber and B. H. Annex (2017). "A MicroRNA93-Interferon Regulatory Factor-9-Immunoresponsive Gene-1-Itaconic Acid Pathway Modulates M2-Like Macrophage Polarization to Revascularize Ischemic Muscle." Circulation **135**(24): 2403-2425.

Geacintov, N. E., M. Cosman, B. E. Hingerty, S. Amin, S. Broyde and D. J. Patel (1997). "NMR solution structures of stereoisometric covalent polycyclic aromatic carcinogen-DNA adduct: principles, patterns, and diversity." Chem Res Toxicol **10**(2): 111-146.

Geeraerts, X., J. Fernandez-Garcia, F. J. Hartmann, K. E. de Goede, L. Martens, Y. Elkrim, A. Debraekeleer, B. Stijlemans, A. Vandekeere, G. Rinaldi, R. De Rycke, M. Planque, D. Broekaert, E. Meinster, E. Clappaert, P. Bardet, A. Murgaski, C. Gysemans, F. A. Nana, Y. Saeys, S. C. Bendall, D. Laoui, J. Van den Bossche, S. M. Fendt and J. A. Van Ginderachter (2021). "Macrophages are metabolically heterogeneous within the tumor microenvironment." Cell Rep **37**(13): 110171.

Geiger, R., J. C. Rieckmann, T. Wolf, C. Basso, Y. Feng, T. Fuhrer, M. Kogadeeva, P. Picotti, F. Meissner, M. Mann, N. Zamboni, F. Sallusto and A. Lanzavecchia (2016). "L-Arginine Modulates T Cell Metabolism and Enhances Survival and Anti-tumor Activity." Cell **167**(3): 829-842 e813.

Georgoudaki, A. M., K. E. Prokopec, V. F. Boura, E. Hellqvist, S. Sohn, J. Ostling, R. Dahan, R. A. Harris, M. Rantalainen, D. Klevebring, M. Sund, S. E. Brage, J. Fuxe, C. Rolny, F. Li, J. V. Ravetch and M. C. Karlsson (2016). "Reprogramming Tumor-Associated Macrophages by Antibody Targeting Inhibits Cancer Progression and Metastasis." Cell Rep **15**(9): 2000-2011.

Gocheva, V., H. W. Wang, B. B. Gadea, T. Shree, K. E. Hunter, A. L. Garfall, T. Berman and J. A. Joyce (2010). "IL-4 induces cathepsin protease activity in tumor-associated macrophages to promote cancer growth and invasion." Genes Dev **24**(3): 241-255.

Goldman, M. J., B. Craft, M. Hastie, K. Repecka, F. McDade, A. Kamath, A. Banerjee, Y. Luo, D. Rogers, A. N. Brooks, J. Zhu and D. Haussler (2020). "Visualizing and interpreting cancer genomics data via the Xena platform." Nat Biotechnol **38**(6): 675-678.

Gozzelino, R., V. Jeney and M. P. Soares (2010). "Mechanisms of cell protection by heme oxygenase-1." Annu Rev Pharmacol Toxicol **50**: 323-354.

Gu, Z., R. Eils and M. Schlesner (2016). "Complex heatmaps reveal patterns and correlations in multidimensional genomic data." Bioinformatics **32**(18): 2847-2849.

Gunaydin, G. (2021). "CAFs Interacting With TAMs in Tumor Microenvironment to Enhance Tumorigenesis and Immune Evasion." Front Oncol **11**: 668349.

Hanahan, D. and R. A. Weinberg (2011). "Hallmarks of cancer: the next generation." Cell **144**(5): 646-674.

He, X. and C. Xu (2020). "Immune checkpoint signaling and cancer immunotherapy." Cell Res **30**(8): 660-669.

Hecht, S. S. (1999). "Tobacco smoke carcinogens and lung cancer." J Natl Cancer Inst **91**(14): 1194-1210.

Hellmann, M. D., J. E. Chaft, W. N. William, Jr., V. Rusch, K. M. Pisters, N. Kalhor, A. Pataer, W. D. Travis, S. G. Swisher, M. G. Kris and M. D. A. L. C. C. G. University of Texas (2014). "Pathological response after neoadjuvant chemotherapy in resectable

non-small-cell lung cancers: proposal for the use of major pathological response as a surrogate endpoint." Lancet Oncol **15**(1): e42-50.

Henze, A. T. and M. Mazzone (2016). "The impact of hypoxia on tumor-associated macrophages." J Clin Invest **126**(10): 3672-3679.

Hersch, S. J. and W. W. Navarre (2020). "The Salmonella LysR Family Regulator RipR Activates the SPI-13-Encoded Itaconate Degradation Cluster." Infect Immun **88**(10).

Hooftman, A. and L. A. J. O'Neill (2019). "The Immunomodulatory Potential of the Metabolite Itaconate." Trends Immunol **40**(8): 687-698.

Hossain, F., A. A. Al-Khami, D. Wyczechowska, C. Hernandez, L. Zheng, K. Reiss, L. D. Valle, J. Trillo-Tinoco, T. Maj, W. Zou, P. C. Rodriguez and A. C. Ochoa (2015). "Inhibition of Fatty Acid Oxidation Modulates Immunosuppressive Functions of Myeloid-Derived Suppressor Cells and Enhances Cancer Therapies." Cancer Immunol Res **3**(11): 1236-1247.

Hwa Yun, B., J. Guo, M. Bellamri and R. J. Turesky (2020). "DNA adducts: Formation, biological effects, and new biospecimens for mass spectrometric measurements in humans." Mass Spectrom Rev **39**(1-2): 55-82.

Inamura, K., K. Takeuchi, Y. Togashi, K. Nomura, H. Ninomiya, M. Okui, Y. Satoh, S. Okumura, K. Nakagawa, M. Soda, Y. L. Choi, T. Niki, H. Mano and Y. Ishikawa (2008). "EML4-ALK fusion is linked to histological characteristics in a subset of lung cancers." J Thorac Oncol **3**(1): 13-17.

Islami, F., A. Goding Sauer, K. D. Miller, R. L. Siegel, S. A. Fedewa, E. J. Jacobs, M. L. McCullough, A. V. Patel, J. Ma, I. Soerjomataram, W. D. Flanders, O. W. Brawley, S. M. Gapstur and A. Jemal (2018). "Proportion and number of cancer cases and deaths attributable to potentially modifiable risk factors in the United States." CA Cancer J Clin **68**(1): 31-54.

Ito, M., G. Ishii, K. Nagai, R. Maeda, Y. Nakano and A. Ochiai (2012). "Prognostic impact of cancer-associated stromal cells in patients with stage I lung adenocarcinoma." Chest **142**(1): 151-158.

Iwai, Y., J. Hamanishi, K. Chamoto and T. Honjo (2017). "Cancer immunotherapies targeting the PD-1 signaling pathway." J Biomed Sci **24**(1): 26.

Jackute, J., M. Zemaitis, D. Pranys, B. Sitkauskiene, S. Miliauskas, S. Vaitkiene and R. Sakalauskas (2018). "Distribution of M1 and M2 macrophages in tumor islets and stroma in relation to prognosis of non-small cell lung cancer." BMC Immunol **19**(1): 3.

Jaiswal, A. K., J. Yadav, S. Makhija, S. Mazumder, A. K. Mitra, A. Suryawanshi, M. Sandey and A. Mishra (2022). "Irg1/itaconate metabolic pathway is a crucial determinant of dendritic cells immune-priming function and contributes to resolute allergen-induced airway inflammation." Mucosal Immunol **15**(2): 301-313.

Jamieson, T., M. Clarke, C. W. Steele, M. S. Samuel, J. Neumann, A. Jung, D. Huels, M. F. Olson, S. Das, R. J. Nibbs and O. J. Sansom (2012). "Inhibition of CXCR2 profoundly suppresses inflammation-driven and spontaneous tumorigenesis." J Clin Invest **122**(9): 3127-3144.

Jayasingam, S. D., M. Citartan, T. H. Thang, A. A. Mat Zin, K. C. Ang and E. S. Ch'ng (2019). "Evaluating the Polarization of Tumor-Associated Macrophages Into M1 and M2 Phenotypes in Human Cancer Tissue: Technicalities and Challenges in Routine Clinical Practice." Front Oncol **9**: 1512.

Jemal, A., F. Bray, M. M. Center, J. Ferlay, E. Ward and D. Forman (2011). "Global cancer statistics." CA Cancer J Clin **61**(2): 69-90.

Johnson, L., K. Mercer, D. Greenbaum, R. T. Bronson, D. Crowley, D. A. Tuveson and T. Jacks (2001). "Somatic activation of the K-ras oncogene causes early onset lung cancer in mice." Nature **410**(6832): 1111-1116.

Kalluri, R. (2016). "The biology and function of fibroblasts in cancer." Nat Rev Cancer **16**(9): 582-598.

Karger, A., S. Mansouri, M. S. Leisegang, A. Weigert, S. Gunther, C. Kuenne, I. Wittig, S. Zukunft, S. Klatt, B. Aliraj, L. V. Klotz, H. Winter, P. Mahavadi, I. Fleming, C. Ruppert, B. Witte, I. Alkoudmani, S. Gattenlohner, F. Grimminger, W. Seeger, S. S. Pullamsetti and R. Savai (2023). "ADPGK-AS1 long noncoding RNA switches macrophage metabolic and phenotypic state to promote lung cancer growth." EMBO J **42**(18): e111620.

Kato, Y., S. Ozawa, C. Miyamoto, Y. Maehata, A. Suzuki, T. Maeda and Y. Baba (2013). "Acidic extracellular microenvironment and cancer." Cancer Cell Int **13**(1): 89.

Kawano, R., Y. Takeshima and K. Inai (1996). "Effects of K-ras gene mutations in the development of lung lesions induced by 4-(N-methyl-n-nitrosamino)-1-(3-pyridyl)-1-butanone in A/J mice." Jpn J Cancer Res **87**(1): 44-50.

Kelly, B. and L. A. O'Neill (2015). "Metabolic reprogramming in macrophages and dendritic cells in innate immunity." Cell Res **25**(7): 771-784.

Kim, N., H. K. Kim, K. Lee, Y. Hong, J. H. Cho, J. W. Choi, J. I. Lee, Y. L. Suh, B. M. Ku, H. H. Eum, S. Choi, Y. L. Choi, J. G. Joung, W. Y. Park, H. A. Jung, J. M. Sun, S. H. Lee, J. S. Ahn, K. Park, M. J. Ahn and H. O. Lee (2020). "Single-cell RNA sequencing demonstrates the molecular and cellular reprogramming of metastatic lung adenocarcinoma." Nat Commun **11**(1): 2285.

Kirthi Koushik, A. S., K. Harish and H. U. Avinash (2013). "Principles of radiation oncology: a beams eye view for a surgeon." Indian J Surg Oncol **4**(3): 255-262.

Koebel, C. M., W. Vermi, J. B. Swann, N. Zerafa, S. J. Rodig, L. J. Old, M. J. Smyth and R. D. Schreiber (2007). "Adaptive immunity maintains occult cancer in an equilibrium state." Nature **450**(7171): 903-907.

Koperniku, A., A. A. Garcia and D. Mochly-Rosen (2022). "Boosting the Discovery of Small Molecule Inhibitors of Glucose-6-Phosphate Dehydrogenase for the Treatment of Cancer, Infectious Diseases, and Inflammation." J Med Chem **65**(6): 4403-4423.

Koundouros, N. and G. Poulogiannis (2020). "Reprogramming of fatty acid metabolism in cancer." Br J Cancer **122**(1): 4-22.

Kumar, V., S. Patel, E. Tcyganov and D. I. Gabrilovich (2016). "The Nature of Myeloid-Derived Suppressor Cells in the Tumor Microenvironment." Trends Immunol **37**(3): 208-220.

Kung, J. T., S. B. Brooks, J. P. Jakway, L. L. Leonard and D. W. Talmage (1977). "Suppression of in vitro cytotoxic response by macrophages due to induced arginase." J Exp Med **146**(3): 665-672.

Kusmartsev, S., Y. Nefedova, D. Yoder and D. I. Gabrilovich (2004). "Antigen-specific inhibition of CD8+ T cell response by immature myeloid cells in cancer is mediated by reactive oxygen species." J Immunol **172**(2): 989-999.

Kwak, E. L., Y. J. Bang, D. R. Camidge, A. T. Shaw, B. Solomon, R. G. Maki, S. H. Ou, B. J. Dezube, P. A. Janne, D. B. Costa, M. Varella-Garcia, W. H. Kim, T. J. Lynch, P. Fidias, H. Stubbs, J. A. Engelman, L. V. Sequist, W. Tan, L. Gandhi, M. Mino-Kenudson, G. C. Wei, S. M. Shreeve, M. J. Ratain, J. Settleman, J. G. Christensen, D. A. Haber, K. Wilner, R. Salgia, G. I. Shapiro, J. W. Clark and A. J. Iafrate (2010). "Anaplastic lymphoma kinase inhibition in non-small-cell lung cancer." N Engl J Med **363**(18): 1693-1703.

Lakins, M. A., E. Ghorani, H. Munir, C. P. Martins and J. D. Shields (2018). "Cancer-associated fibroblasts induce antigen-specific deletion of CD8 (+) T Cells to protect tumour cells." Nat Commun **9**(1): 948.

Lampropoulou, V., A. Sergushichev, M. Bambouskova, S. Nair, E. E. Vincent, E. Loginicheva, L. Cervantes-Barragan, X. Ma, S. C. Huang, T. Griss, C. J. Weinheimer, S. Khader, G. J. Randolph, E. J. Pearce, R. G. Jones, A. Diwan, M. S. Diamond and M. N. Artyomov (2016). "Itaconate Links Inhibition of Succinate Dehydrogenase with Macrophage Metabolic Remodeling and Regulation of Inflammation." Cell Metab **24**(1): 158-166.

Lee, C. G., N. A. Jenkins, D. J. Gilbert, N. G. Copeland and W. E. O'Brien (1995). "Cloning and analysis of gene regulation of a novel LPS-inducible cDNA." Immunogenetics **41**(5): 263-270.

Lee, J., J. Park, H. Choi, J. Kim, A. Kwon, W. Jang, H. Chae, M. Kim, Y. Kim, J. W. Lee, N. G. Chung and B. Cho (2017). "Genetic Profiles of Korean Patients With Glucose-6-Phosphate Dehydrogenase Deficiency." Ann Lab Med **37**(2): 108-116.

Lee, J. M., M. H. Lee, E. Garon, J. W. Goldman, R. Salehi-Rad, F. E. Baratelli, D. Schaue, G. Wang, F. Rosen, J. Yanagawa, T. C. Walser, Y. Lin, S. J. Park, S. Adams, F. M. Marincola, P. C. Tumeh, F. Abtin, R. Suh, K. L. Reckamp, G. Lee, W. D. Wallace, S. Lee, G. Zeng, D. A. Elashoff, S. Sharma and S. M. Dubinett (2017). "Phase I Trial of Intratumoral Injection of CCL21 Gene-Modified Dendritic Cells in Lung Cancer Elicits Tumor-Specific Immune Responses and CD8(+) T-cell Infiltration." Clin Cancer Res **23**(16): 4556-4568.

Lemjabbar-Alaoui, H., O. U. Hassan, Y. W. Yang and P. Buchanan (2015). "Lung cancer: Biology and treatment options." Biochim Biophys Acta **1856**(2): 189-210.

Liang, Y. and H. A. Wakelee (2013). "Adjuvant chemotherapy of completely resected early stage non-small cell lung cancer (NSCLC)." Transl Lung Cancer Res **2**(5): 403-410.

Liao, S. T., C. Han, D. Q. Xu, X. W. Fu, J. S. Wang and L. Y. Kong (2019). "4-Octyl Itaconate inhibits aerobic glycolysis by targeting GAPDH to exert anti-inflammatory effects." Nat Commun **10**(1): 5091.

Liao, Y., G. K. Smyth and W. Shi (2014). "featureCounts: an efficient general purpose program for assigning sequence reads to genomic features." Bioinformatics **30**(7): 923-930.

Lin, E. Y., V. Gouon-Evans, A. V. Nguyen and J. W. Pollard (2002). "The macrophage growth factor CSF-1 in mammary gland development and tumor progression." J Mammary Gland Biol Neoplasia **7**(2): 147-162.

Liu, X., P. Wang, C. Zhang and Z. Ma (2017). "Epidermal growth factor receptor (EGFR): A rising star in the era of precision medicine of lung cancer." Oncotarget **8**(30): 50209-50220.

LoPiccolo, J., A. Gusev, D. C. Christiani and P. A. Janne (2024). "Lung cancer in patients who have never smoked - an emerging disease." Nat Rev Clin Oncol.

Love, M. I., W. Huber and S. Anders (2014). "Moderated estimation of fold change and dispersion for RNA-seq data with DESeq2." Genome Biol **15**(12): 550.

Lynch, T. J., D. W. Bell, R. Sordella, S. Gurubhagavatula, R. A. Okimoto, B. W. Brannigan, P. L. Harris, S. M. Haserlat, J. G. Supko, F. G. Haluska, D. N. Louis, D. C. Christiani, J. Settleman and D. A. Haber (2004). "Activating mutations in the epidermal growth factor receptor underlying responsiveness of non-small-cell lung cancer to gefitinib." N Engl J Med **350**(21): 2129-2139.

MacKie, R. M., R. Reid and B. Junor (2003). "Fatal melanoma transferred in a donated kidney 16 years after melanoma surgery." N Engl J Med **348**(6): 567-568.

Mantovani, A., F. Marchesi, A. Malesci, L. Laghi and P. Allavena (2017). "Tumour-associated macrophages as treatment targets in oncology." Nat Rev Clin Oncol **14**(7): 399-416.

Mantovani, A., S. Sozzani, M. Locati, P. Allavena and A. Sica (2002). "Macrophage polarization: tumor-associated macrophages as a paradigm for polarized M2 mononuclear phagocytes." Trends Immunol **23**(11): 549-555.

Mascaux, C., N. Iannino, B. Martin, M. Paesmans, T. Berghmans, M. Dusart, A. Haller, P. Lothaire, A. P. Meert, S. Noel, J. J. Lafitte and J. P. Sculier (2005). "The role of RAS oncogene in survival of patients with lung cancer: a systematic review of the literature with meta-analysis." Br J Cancer **92**(1): 131-139.

Mayers, J. R., M. E. Torrence, L. V. Danai, T. Papagiannakopoulos, S. M. Davidson, M. R. Bauer, A. N. Lau, B. W. Ji, P. D. Dixit, A. M. Hosios, A. Muir, C. R. Chin, E. Freinkman, T. Jacks, B. M. Wolpin, D. Vitkup and M. G. Vander Heiden (2016). "Tissue of origin dictates branched-chain amino acid metabolism in mutant Kras-driven cancers." Science **353**(6304): 1161-1165.

Mazzone, M., A. Menga and A. Castegna (2018). "Metabolism and TAM functions-it takes two to tango." FEBS J **285**(4): 700-716.

Mele, L., F. Paino, F. Papaccio, T. Regad, D. Boocock, P. Stiuso, A. Lombardi, D. Liccardo, G. Aquino, A. Barbieri, C. Arra, C. Coveney, M. La Noce, G. Papaccio, M. Caraglia, V. Tirino and V. Desiderio (2018). "A new inhibitor of glucose-6-phosphate dehydrogenase blocks pentose phosphate pathway and suppresses malignant proliferation and metastasis in vivo." Cell Death Dis **9**(5): 572.

Michelucci, A., T. Cordes, J. Ghelfi, A. Pailot, N. Reiling, O. Goldmann, T. Binz, A. Wegner, A. Tallam, A. Rausell, M. Buttini, C. L. Linster, E. Medina, R. Balling and K. Hiller (2013). "Immune-responsive gene 1 protein links metabolism to immunity by catalyzing itaconic acid production." Proc Natl Acad Sci U S A **110**(19): 7820-7825.

Miller, A., C. Nagy, B. Knapp, J. Laengle, E. Ponweiser, M. Groeger, P. Starkl, M. Bergmann, O. Wagner and A. Haschemi (2017). "Exploring Metabolic Configurations of Single Cells within Complex Tissue Microenvironments." Cell Metab **26**(5): 788-800 e786.

Mills, E. L., D. G. Ryan, H. A. Prag, D. Dikovskaya, D. Menon, Z. Zaslona, M. P. Jedrychowski, A. S. H. Costa, M. Higgins, E. Hams, J. Szpyt, M. C. Runtsch, M. S. King, J. F. McGouran, R. Fischer, B. M. Kessler, A. F. McGettrick, M. M. Hughes, R. G. Carroll, L. M. Booty, E. V. Knatko, P. J. Meakin, M. L. J. Ashford, L. K. Modis, G. Brunori, D. C. Sevin, P. G. Fallon, S. T. Caldwell, E. R. S. Kunji, E. T. Chouchani, C. Frezza, A. T.

Dinkova-Kostova, R. C. Hartley, M. P. Murphy and L. A. O'Neill (2018). "Itaconate is an anti-inflammatory metabolite that activates Nrf2 via alkylation of KEAP1." Nature **556**(7699): 113-117.

Mitsuishi, Y., K. Taguchi, Y. Kawatani, T. Shibata, T. Nukiwa, H. Aburatani, M. Yamamoto and H. Motohashi (2012). "Nrf2 redirects glucose and glutamine into anabolic pathways in metabolic reprogramming." Cancer Cell **22**(1): 66-79.

Nagashio, R., S. Oikawa, K. Yanagita, D. Hagiuda, Y. Kuchitsu, S. Igawa, K. Naoki, Y. Satoh, M. Ichinoe, Y. Murakumo, M. Saegusa and Y. Sato (2019). "Prognostic significance of G6PD expression and localization in lung adenocarcinoma." Biochim Biophys Acta Proteins Proteom **1867**(1): 38-46.

Nelson, V. L., H. C. B. Nguyen, J. C. Garcia-Canaveras, E. R. Briggs, W. Y. Ho, J. R. DiSpirito, J. M. Marinis, D. A. Hill and M. A. Lazar (2018). "PPARgamma is a nexus controlling alternative activation of macrophages via glutamine metabolism." Genes Dev **32**(15-16): 1035-1044.

Nishimura, T., K. Iwakabe, M. Sekimoto, Y. Ohmi, T. Yahata, M. Nakui, T. Sato, S. Habu, H. Tashiro, M. Sato and A. Ohta (1999). "Distinct role of antigen-specific T helper type 1 (Th1) and Th2 cells in tumor eradication in vivo." J Exp Med **190**(5): 617-627.

Noman, M. Z., G. Desantis, B. Janji, M. Hasmim, S. Karray, P. Dessen, V. Bronte and S. Chouaib (2014). "PD-L1 is a novel direct target of HIF-1alpha, and its blockade under hypoxia enhanced MDSC-mediated T cell activation." J Exp Med **211**(5): 781-790.

O'Neill, L. A. J. and M. N. Artyomov (2019). "Itaconate: the poster child of metabolic reprogramming in macrophage function." Nat Rev Immunol **19**(5): 273-281.

Ogger, P. P., G. J. Albers, R. J. Hewitt, B. J. O'Sullivan, J. E. Powell, E. Calamita, P. Ghai, S. A. Walker, P. McErlean, P. Saunders, S. Kingston, P. L. Molyneaux, J. M. Halket, R. Gray, D. C. Chambers, T. M. Maher, C. M. Lloyd and A. J. Byrne (2020). "Itaconate controls the severity of pulmonary fibrosis." Sci Immunol **5**(52).

Orillion, A., N. P. Damayanti, L. Shen, R. Adelaiye-Ogala, H. Affronti, M. Elbanna, S. Chintala, M. Ciesielski, L. Fontana, C. Kao, B. D. Elzey, T. L. Ratliff, D. E. Nelson, D. Smiraglia, S. I. Abrams and R. Pili (2018). "Dietary Protein Restriction Reprograms Tumor-Associated Macrophages and Enhances Immunotherapy." Clin Cancer Res **24**(24): 6383-6395.

Paez, J. G., P. A. Janne, J. C. Lee, S. Tracy, H. Greulich, S. Gabriel, P. Herman, F. J. Kaye, N. Lindeman, T. J. Boggon, K. Naoki, H. Sasaki, Y. Fujii, M. J. Eck, W. R. Sellers, B. E. Johnson and M. Meyerson (2004). "EGFR mutations in lung cancer: correlation with clinical response to gefitinib therapy." Science **304**(5676): 1497-1500.

Palmieri, E. M., A. Menga, R. Martin-Perez, A. Quinto, C. Riera-Domingo, G. De Tullio, D. C. Hooper, W. H. Lamers, B. Ghesquiere, D. W. McVicar, A. Guarini, M. Mazzone

and A. Castegna (2017). "Pharmacologic or Genetic Targeting of Glutamine Synthetase Skews Macrophages toward an M1-like Phenotype and Inhibits Tumor Metastasis." Cell Rep **20**(7): 1654-1666.

Pantaloni, D., C. Le Clainche and M. F. Carlier (2001). "Mechanism of actin-based motility." Science **292**(5521): 1502-1506.

Parashar, B., S. Arora and A. G. Wernicke (2013). "Radiation therapy for early stage lung cancer." Semin Intervent Radiol **30**(2): 185-190.

Pardoll, D. M. (2012). "The blockade of immune checkpoints in cancer immunotherapy." Nat Rev Cancer **12**(4): 252-264.

Patra, K. C. and N. Hay (2014). "The pentose phosphate pathway and cancer." Trends Biochem Sci **39**(8): 347-354.

Peace, C. G. and L. A. O'Neill (2022). "The role of itaconate in host defense and inflammation." J Clin Invest **132**(2).

Qin, W., K. Qin, Y. Zhang, W. Jia, Y. Chen, B. Cheng, L. Peng, N. Chen, Y. Liu, W. Zhou, Y. L. Wang, X. Chen and C. Wang (2019). "S-glycosylation-based cysteine profiling reveals regulation of glycolysis by itaconate." Nat Chem Biol **15**(10): 983-991.

Qin, W., Y. Zhang, H. Tang, D. Liu, Y. Chen, Y. Liu and C. Wang (2020). "Chemoproteomic Profiling of Itaconation by Bioorthogonal Probes in Inflammatory Macrophages." J Am Chem Soc **142**(25): 10894-10898.

Rao, X., X. Duan, W. Mao, X. Li, Z. Li, Q. Li, Z. Zheng, H. Xu, M. Chen, P. G. Wang, Y. Wang, B. Shen and W. Yi (2015). "O-GlcNAcylation of G6PD promotes the pentose phosphate pathway and tumor growth." Nat Commun **6**: 8468.

Reinfeld, B. I., M. Z. Madden, M. M. Wolf, A. Chytil, J. E. Bader, A. R. Patterson, A. Sugiura, A. S. Cohen, A. Ali, B. T. Do, A. Muir, C. A. Lewis, R. A. Hongo, K. L. Young, R. E. Brown, V. M. Todd, T. Huffstater, A. Abraham, R. T. O'Neil, M. H. Wilson, F. Xin, M. N. Tantawy, W. D. Merryman, R. W. Johnson, C. S. Williams, E. F. Mason, F. M. Mason, K. E. Beckermann, M. G. Vander Heiden, H. C. Manning, J. C. Rathmell and W. K. Rathmell (2021). "Cell-programmed nutrient partitioning in the tumour microenvironment." Nature **593**(7858): 282-288.

Ritchie, M. E., B. Phipson, D. Wu, Y. Hu, C. W. Law, W. Shi and G. K. Smyth (2015). "limma powers differential expression analyses for RNA-sequencing and microarray studies." Nucleic Acids Res **43**(7): e47.

Robert, C. (2020). "A decade of immune-checkpoint inhibitors in cancer therapy." Nat Commun **11**(1): 3801.

Rodriguez, P. C. and A. C. Ochoa (2008). "Arginine regulation by myeloid derived suppressor cells and tolerance in cancer: mechanisms and therapeutic perspectives." Immunol Rev **222**: 180-191.

Rodriguez, P. C., D. G. Quiceno, J. Zabaleta, B. Ortiz, A. H. Zea, M. B. Piazuelo, A. Delgado, P. Correa, J. Brayer, E. M. Sotomayor, S. Antonia, J. B. Ochoa and A. C. Ochoa (2004). "Arginase I production in the tumor microenvironment by mature myeloid cells inhibits T-cell receptor expression and antigen-specific T-cell responses." Cancer Res **64**(16): 5839-5849.

Rossi, A. and M. Di Maio (2016). "Platinum-based chemotherapy in advanced non-small-cell lung cancer: optimal number of treatment cycles." Expert Rev Anticancer Ther **16**(6): 653-660.

Runtsch, M. C., S. Angiari, A. Hooftman, R. Wadhwa, Y. Zhang, Y. Zheng, J. S. Spina, M. C. Ruzek, M. A. Argiriadi, A. F. McGettrick, R. S. Mendez, A. Zotta, C. G. Peace, A. Walsh, R. Chirillo, E. Hams, P. G. Fallon, R. Jayamaran, K. Dua, A. C. Brown, R. Y. Kim, J. C. Horvat, P. M. Hansbro, C. Wang and L. A. J. O'Neill (2022). "Itaconate and itaconate derivatives target JAK1 to suppress alternative activation of macrophages." Cell Metab **34**(3): 487-501 e488.

Russell, D. G., L. Huang and B. C. VanderVen (2019). "Immunometabolism at the interface between macrophages and pathogens." Nat Rev Immunol **19**(5): 291-304.

Sa-Pessoa, J., S. Paiva, D. Ribas, I. J. Silva, S. C. Viegas, C. M. Arraiano and M. Casal (2013). "SATP (YaaH), a succinate-acetate transporter protein in Escherichia coli." Biochem J **454**(3): 585-595.

Sarode, P., S. Mansouri, A. Karger, M. B. Schaefer, F. Grimminger, W. Seeger and R. Savai (2020). "Epithelial cell plasticity defines heterogeneity in lung cancer." Cell Signal **65**: 109463.

Sarode, P., X. Zheng, G. A. Giotopoulou, A. Weigert, C. Kuenne, S. Gunther, A. Friedrich, S. Gattenlohner, T. Stiewe, B. Brune, F. Grimminger, G. T. Stathopoulos, S. S. Pullamsetti, W. Seeger and R. Savai (2020). "Reprogramming of tumor-associated macrophages by targeting beta-catenin/FOSL2/ARID5A signaling: A potential treatment of lung cancer." Sci Adv **6**(23): eaaz6105.

Schmall, A., H. M. Al-Tamari, S. Herold, M. Kampschulte, A. Weigert, A. Wietelmann, N. Vipotnik, F. Grimminger, W. Seeger, S. S. Pullamsetti and R. Savai (2015). "Macrophage and cancer cell cross-talk via CCR2 and CX3CR1 is a fundamental mechanism driving lung cancer." Am J Respir Crit Care Med **191**(4): 437-447.

Schneider, T., H. Hoffmann, H. Dienemann, P. A. Schnabel, A. H. Enk, S. Ring and K. Mahnke (2011). "Non-small cell lung cancer induces an immunosuppressive phenotype of dendritic cells in tumor microenvironment by upregulating B7-H3." J Thorac Oncol **6**(7): 1162-1168.

Semba, H., N. Takeda, T. Isagawa, Y. Sugiura, K. Honda, M. Wake, H. Miyazawa, Y. Yamaguchi, M. Miura, D. M. Jenkins, H. Choi, J. W. Kim, M. Asagiri, A. S. Cowburn, H.

Abe, K. Soma, K. Koyama, M. Katoh, K. Sayama, N. Goda, R. S. Johnson, I. Manabe, R. Nagai and I. Komuro (2016). "HIF-1alpha-PDK1 axis-induced active glycolysis plays an essential role in macrophage migratory capacity." Nat Commun **7**: 11635.

Shalapour, S. and M. Karin (2015). "Immunity, inflammation, and cancer: an eternal fight between good and evil." J Clin Invest **125**(9): 3347-3355.

Siegel, R., D. Naishadham and A. Jemal (2013). "Cancer statistics, 2013." CA Cancer J Clin **63**(1): 11-30.

Siegel, R. L., K. D. Miller, H. E. Fuchs and A. Jemal (2021). "Cancer Statistics, 2021." CA Cancer J Clin **71**(1): 7-33.

Siegel, R. L., K. D. Miller and A. Jemal (2019). "Cancer statistics, 2019." CA Cancer J Clin **69**(1): 7-34.

Siegel, R. L., K. D. Miller, N. S. Wagle and A. Jemal (2023). "Cancer statistics, 2023." CA Cancer J Clin **73**(1): 17-48.

Singhal, S., J. Stadanlick, M. J. Annunziata, A. S. Rao, P. S. Bhojnagarwala, S. O'Brien, E. K. Moon, E. Cantu, G. Danet-Desnoyers, H. J. Ra, L. Litzky, T. Akimova, U. H. Beier, W. W. Hancock, S. M. Albelda and E. B. Eruslanov (2019). "Human tumor-associated monocytes/macrophages and their regulation of T cell responses in early-stage lung cancer." Sci Transl Med **11**(479).

Skoulidis, F. and J. V. Heymach (2019). "Co-occurring genomic alterations in non-small-cell lung cancer biology and therapy." Nat Rev Cancer **19**(9): 495-509.

Sorin, M., M. Rezanejad, E. Karimi, B. Fiset, L. Desharnais, L. J. M. Perus, S. Milette, M. W. Yu, S. M. Maritan, S. Dore, E. Pichette, W. Enlow, A. Gagne, Y. Wei, M. Orain, V. S. K. Manem, R. Rayes, P. M. Siegel, S. Camilleri-Broet, P. O. Fiset, P. Desmeules, J. D. Spicer, D. F. Quail, P. Joubert and L. A. Walsh (2023). "Single-cell spatial landscapes of the lung tumour immune microenvironment." Nature **614**(7948): 548-554.

Stanton, R. C. (2012). "Glucose-6-phosphate dehydrogenase, NADPH, and cell survival." IUBMB Life **64**(5): 362-369.

Stincone, A., A. Prigione, T. Cramer, M. M. Wamelink, K. Campbell, E. Cheung, V. Olin-Sandoval, N. M. Gruning, A. Kruger, M. Tauqeer Alam, M. A. Keller, M. Breitenbach, K. M. Brindle, J. D. Rabinowitz and M. Ralser (2015). "The return of metabolism: biochemistry and physiology of the pentose phosphate pathway." Biol Rev Camb Philos Soc **90**(3): 927-963.

Strelko, C. L., W. Lu, F. J. Dufort, T. N. Seyfried, T. C. Chiles, J. D. Rabinowitz and M. F. Roberts (2011). "Itaconic acid is a mammalian metabolite induced during macrophage activation." J Am Chem Soc **133**(41): 16386-16389.

Su, P., Q. Wang, E. Bi, X. Ma, L. Liu, M. Yang, J. Qian and Q. Yi (2020). "Enhanced Lipid Accumulation and Metabolism Are Required for the Differentiation and Activation of Tumor-Associated Macrophages." Cancer Res **80**(7): 1438-1450.

Subramanian, A., P. Tamayo, V. K. Mootha, S. Mukherjee, B. L. Ebert, M. A. Gillette, A. Paulovich, S. L. Pomeroy, T. R. Golub, E. S. Lander and J. P. Mesirov (2005). "Gene set enrichment analysis: a knowledge-based approach for interpreting genome-wide expression profiles." Proc Natl Acad Sci U S A **102**(43): 15545-15550.

Sun, K. A., Y. Li, A. Y. Meliton, P. S. Woods, L. M. Kimmig, R. Cetin-Atalay, R. B. Hamanaka and G. M. Mutlu (2020). "Endogenous itaconate is not required for particulate matter-induced NRF2 expression or inflammatory response." Elife **9**.

Sun, S., J. H. Schiller and A. F. Gazdar (2007). "Lung cancer in never smokers--a different disease." Nat Rev Cancer **7**(10): 778-790.

Swain, A., M. Bambouskova, H. Kim, P. S. Andhey, D. Duncan, K. Auclair, V. Chubukov, D. M. Simons, T. P. Roddy, K. M. Stewart and M. N. Artyomov (2020). "Comparative evaluation of itaconate and its derivatives reveals divergent inflammasome and type I interferon regulation in macrophages." Nat Metab **2**(7): 594-602.

Tate, J. G., S. Bamford, H. C. Jubb, Z. Sondka, D. M. Beare, N. Bindal, H. Boutselakis, C. G. Cole, C. Creatore, E. Dawson, P. Fish, B. Harsha, C. Hathaway, S. C. Jupe, C. Y. Kok, K. Noble, L. Ponting, C. C. Ramshaw, C. E. Rye, H. E. Speedy, R. Stefancsik, S. L. Thompson, S. Wang, S. Ward, P. J. Campbell and S. A. Forbes (2019). "COSMIC: the Catalogue Of Somatic Mutations In Cancer." Nucleic Acids Res **47**(D1): D941-D947.

Taylor, M. D., A. S. Nagji, C. M. Bhamidipati, N. Theodosakis, B. D. Kozower, C. L. Lau and D. R. Jones (2012). "Tumor recurrence after complete resection for non-small cell lung cancer." Ann Thorac Surg **93**(6): 1813-1820; discussion 1820-1811.

Thirusangu, P. and V. Vigneshwaran (2020). Lung Cancer: Pathophysiology and Current Advancements in Therapeutics. Chronic Lung Diseases: Pathophysiology and Therapeutics. S. Rayees, I. Din, G. Singh and F. A. Malik. Singapore, Springer Singapore**:** 129-141.

Tian, W. N., L. D. Braunstein, J. Pang, K. M. Stuhlmeier, Q. C. Xi, X. Tian and R. C. Stanton (1998). "Importance of glucose-6-phosphate dehydrogenase activity for cell growth." J Biol Chem **273**(17): 10609-10617.

Traag, V. A., L. Waltman and N. J. van Eck (2019). "From Louvain to Leiden: guaranteeing well-connected communities." Sci Rep **9**(1): 5233.

Travis, W. D. (2012). "Update on small cell carcinoma and its differentiation from squamous cell carcinoma and other non-small cell carcinomas." Mod Pathol **25 Suppl 1**: S18-30.

Uribe-Querol, E. and C. Rosales (2015). "Neutrophils in Cancer: Two Sides of the Same Coin." J Immunol Res **2015**: 983698.

Vogelstein, B. and K. W. Kinzler (1993). "The multistep nature of cancer." Trends Genet **9**(4): 138-141.

Wang, L., L. Cao, H. Wang, B. Liu, Q. Zhang, Z. Meng, X. Wu, Q. Zhou and K. Xu (2017). "Cancer-associated fibroblasts enhance metastatic potential of lung cancer cells through IL-6/STAT3 signaling pathway." Oncotarget **8**(44): 76116-76128.

Wang, Q., X. L. Li, Y. Mei, J. C. Ye, W. Fan, G. H. Cheng, M. S. Zeng and G. K. Feng (2020). "The anti-inflammatory drug dimethyl itaconate protects against colitis-associated colorectal cancer." J Mol Med (Berl) **98**(10): 1457-1466.

Wang, Y., A. M. Armando, O. Quehenberger, C. Yan and E. A. Dennis (2014). "Comprehensive ultra-performance liquid chromatographic separation and mass spectrometric analysis of eicosanoid metabolites in human samples." J Chromatogr A **1359**: 60-69.

Wang, Y. P., L. S. Zhou, Y. Z. Zhao, S. W. Wang, L. L. Chen, L. X. Liu, Z. Q. Ling, F. J. Hu, Y. P. Sun, J. Y. Zhang, C. Yang, Y. Yang, Y. Xiong, K. L. Guan and D. Ye (2014). "Regulation of G6PD acetylation by SIRT2 and KAT9 modulates NADPH homeostasis and cell survival during oxidative stress." EMBO J **33**(12): 1304-1320.

Wculek, S. K., I. Heras-Murillo, A. Mastrangelo, D. Mananes, M. Galan, V. Miguel, A. Curtabbi, C. Barbas, N. S. Chandel, J. A. Enriquez, S. Lamas and D. Sancho (2023). "Oxidative phosphorylation selectively orchestrates tissue macrophage homeostasis." Immunity **56**(3): 516-530 e519.

Weigert, A., X. Zheng, A. Nenzel, K. Turkowski, S. Gunther, E. Strack, E. Sirait-Fischer, E. Elwakeel, I. M. Kur, V. S. Nikam, C. Valasarajan, H. Winter, A. Wissgott, R. Voswinkel, F. Grimminger, B. Brune, W. Seeger, S. S. Pullamsetti and R. Savai (2022). "Fibrocytes boost tumor-supportive phenotypic switches in the lung cancer niche via the endothelin system." Nat Commun **13**(1): 6078.

Weiss, J. M., L. C. Davies, M. Karwan, L. Ileva, M. K. Ozaki, R. Y. Cheng, L. A. Ridnour, C. M. Annunziata, D. A. Wink and D. W. McVicar (2018). "Itaconic acid mediates crosstalk between macrophage metabolism and peritoneal tumors." J Clin Invest **128**(9): 3794-3805.

Wenes, M., M. Shang, M. Di Matteo, J. Goveia, R. Martin-Perez, J. Serneels, H. Prenen, B. Ghesquiere, P. Carmeliet and M. Mazzone (2016). "Macrophage Metabolism Controls Tumor Blood Vessel Morphogenesis and Metastasis." Cell Metab **24**(5): 701-715.

Willforss, J., A. Chawade and F. Levander (2019). "NormalyzerDE: Online Tool for Improved Normalization of Omics Expression Data and High-Sensitivity Differential Expression Analysis." J Proteome Res **18**(2): 732-740.

Winterhoff, M., F. Chen, N. Sahini, T. Ebensen, M. Kuhn, V. Kaever, H. Bahre and F. Pessler (2021). "Establishment, Validation, and Initial Application of a Sensitive LC-MS/MS Assay for Quantification of the Naturally Occurring Isomers Itaconate, Mesaconate, and Citraconate." Metabolites **11**(5).

Wolf, F. A., P. Angerer and F. J. Theis (2018). "SCANPY: large-scale single-cell gene expression data analysis." Genome Biol **19**(1): 15.

Xiao, H., Y. Guo, B. Li, X. Li, Y. Wang, S. Han, D. Cheng and X. Shuai (2020). "M2-Like Tumor-Associated Macrophage-Targeted Codelivery of STAT6 Inhibitor and IKKbeta siRNA Induces M2-to-M1 Repolarization for Cancer Immunotherapy with Low Immune Side Effects." ACS Cent Sci **6**(7): 1208-1222.

Xue, J., S. V. Schmidt, J. Sander, A. Draffehn, W. Krebs, I. Quester, D. De Nardo, T. D. Gohel, M. Emde, L. Schmidleithner, H. Ganesan, A. Nino-Castro, M. R. Mallmann, L. Labzin, H. Theis, M. Kraut, M. Beyer, E. Latz, T. C. Freeman, T. Ulas and J. L. Schultze (2014). "Transcriptome-based network analysis reveals a spectrum model of human macrophage activation." Immunity **40**(2): 274-288.

Yang, S. C., R. K. Batra, S. Hillinger, K. L. Reckamp, R. M. Strieter, S. M. Dubinett and S. Sharma (2006). "Intrapulmonary administration of CCL21 gene-modified dendritic cells reduces tumor burden in spontaneous murine bronchoalveolar cell carcinoma." Cancer Res **66**(6): 3205-3213.

Zappa, C. and S. A. Mousa (2016). "Non-small cell lung cancer: current treatment and future advances." Transl Lung Cancer Res **5**(3): 288-300.

Zeng, Y. R., J. B. Song, D. Wang, Z. X. Huang, C. Zhang, Y. P. Sun, G. Shu, Y. Xiong, K. L. Guan, D. Ye and P. Wang (2023). "The immunometabolite itaconate stimulates OXGR1 to promote mucociliary clearance during the pulmonary innate immune response." J Clin Invest **133**(6).

Zhan, Z., Z. Wang, Y. Bao, W. Liu and L. Hong (2022). "OI inhibits development of ovarian cancer by blocking crosstalk between cancer cells and macrophages via HIF-1alpha pathway." Biochem Biophys Res Commun **606**: 142-148.

Zhang, Q., J. Wang, D. K. Yadav, X. Bai and T. Liang (2021). "Glucose Metabolism: The Metabolic Signature of Tumor Associated Macrophage." Front Immunol **12**: 702580.

Zhang, Y. L., J. Q. Yuan, K. F. Wang, X. H. Fu, X. R. Han, D. Threapleton, Z. Y. Yang, C. Mao and J. L. Tang (2016). "The prevalence of EGFR mutation in patients with non-small cell lung cancer: a systematic review and meta-analysis." Oncotarget **7**(48): 78985-78993.

Zhao, H., D. Teng, L. Yang, X. Xu, J. Chen, T. Jiang, A. Y. Feng, Y. Zhang, D. T. Frederick, L. Gu, L. Cai, J. M. Asara, M. Pasca di Magliano, G. M. Boland, K. T. Flaherty, K. D. Swanson, D. Liu, J. D. Rabinowitz and B. Zheng (2022). "Myeloid-derived itaconate

suppresses cytotoxic CD8(+) T cells and promotes tumour growth." Nat Metab **4**(12): 1660-1673.

Zheng, X., S. Mansouri, A. Krager, F. Grimminger, W. Seeger, S. S. Pullamsetti, C. E. Wheelock and R. Savai (2020). "Metabolism in tumour-associated macrophages: a quid pro quo with the tumour microenvironment." Eur Respir Rev **29**(157).

Zheng, X., P. Sarode, A. Weigert, K. Turkowski, P. Chelladurai, S. Gunther, C. Kuenne, H. Winter, A. Stenzinger, S. Reu, F. Grimminger, T. Stiewe, W. Seeger, S. S. Pullamsetti and R. Savai (2023). "The HDAC2-SP1 Axis Orchestrates Protumor Macrophage Polarization." Cancer Res **83**(14): 2345-2357.

Zheng, X., K. Turkowski, J. Mora, B. Brune, W. Seeger, A. Weigert and R. Savai (2017). "Redirecting tumor-associated macrophages to become tumoricidal effectors as a novel strategy for cancer therapy." Oncotarget **8**(29): 48436-48452.

Zheng, X., A. Weigert, S. Reu, S. Guenther, S. Mansouri, B. Bassaly, S. Gattenlohner, F. Grimminger, S. Pullamsetti, W. Seeger, H. Winter and R. Savai (2020). "Spatial Density and Distribution of Tumor-Associated Macrophages Predict Survival in Non-Small Cell Lung Carcinoma." Cancer Res **80**(20): 4414-4425.

Zilionis, R., C. Engblom, C. Pfirschke, V. Savova, D. Zemmour, H. D. Saatcioglu, I. Krishnan, G. Maroni, C. V. Meyerovitz, C. M. Kerwin, S. Choi, W. G. Richards, A. De Rienzo, D. G. Tenen, R. Bueno, E. Levantini, M. J. Pittet and A. M. Klein (2019). "Single-Cell Transcriptomics of Human and Mouse Lung Cancers Reveals Conserved Myeloid Populations across Individuals and Species." Immunity **50**(5): 1317-1334 e1310.

13. Ehrenwörtliche Erklärung

„Hiermit erkläre ich, dass ich die vorliegende Arbeit selbständig und ohne unzulässige Hilfe oder Benutzung anderer als der angegebenen Hilfsmittel angefertigt habe. Alle Textstellen, die wörtlich oder sinngemäß aus veröffentlichten oder nichtveröffentlichten Schriften entnommen sind, und alle Angaben, die auf mündlichen Auskünften beruhen, sind als solche kenntlich gemacht. Bei den von mir durchgeführten und in der Dissertation erwähnten Untersuchungen habe ich die Grundsätze guter wissenschaftlicher Praxis, wie sie in der „Satzung der Justus-Liebig-Universität Gießen zur Sicherung guter wissenschaftlicher Praxis“ niedergelegt sind, eingehalten sowie ethische, datenschutzrechtliche und tierschutzrechtliche Grundsätze befolgt. Ich versichere, dass Dritte von mir weder unmittelbar noch mittelbar geldwerte Leistungen für Arbeiten erhalten haben, die im Zusammenhang mit dem Inhalt der vorgelegten Dissertation stehen, und dass die vorgelegte Arbeit weder im Inland noch im Ausland in gleicher oder ähnlicher Form einer anderen Prüfungsbehörde zum Zweck einer Promotion oder eines anderen Prüfungsverfahrens vorgelegt wurde. Alles aus anderen Quellen und von anderen Personen übernommene Material, das in der Arbeit verwendet wurde oder auf das direkt Bezug genommen wird, wurde als solches kenntlich gemacht. Insbesondere wurden alle Personen genannt, die direkt und indirekt an der Entstehung der vorliegenden Arbeit beteiligt waren. Mit der Überprüfung meiner Arbeit durch eine Plagiatserkennungssoftware bzw. ein internetbasiertes Softwareprogramm erkläre ich mich einverstanden.“

_____ _____

Ort/Datum Unterschrift

14. Acknowledgments

I would like to begin by expressing my profound gratitude to my advisor, Prof. Dr. Rajkumar Savai, for his unwavering support throughout my Ph.D. journey and related research endeavors. His patience, motivation, and extensive knowledge have been invaluable to me not only about the science but also about the life and being a good human. His guidance and significant support played a pivotal role in shaping my research and in the preparation of this thesis. I feel incredibly fortunate to have had such an exceptional advisor and mentor during my Ph.D. studies.

In addition to my advisor, I extend my heartfelt thanks to Prof. Dr. Soni Savai Pullamsetti for her valuable inputs and thoughtfulness since starting this project. I also really appreciate to Prof. Dr. Werner Seeger, Prof. Dr. Andreas Weigert for their insightful comments, encouragement, and thought-provoking questions. Their input challenged me to broaden the horizons of my research from various angles.

I would like to extend my sincere appreciation to all those who contributed to and collaborated on this project, their collective efforts and expertise were instrumental in its success; Dr. Stefan Guenther for transcriptomic analysis, Dr. Ujjwal Neogi and Dr. Anoop Ambikan for proteomic and integrative analysis, Dr. Stephan Klatt and Dr. Sven Zukunft for metabolome analysis and Dr. Konda Babu Kurakula for in silico analysis.

I want to extend my heartfelt gratitude to my wonderful fellow labmates, including Poonam, Rajender, Shahriar, Javad, Parisa, Spyridoula, Yanina, Annika, Oeznur, Kati, Philip, Josh, Xiang and all previous colleagues. Our engaging discussions about science and life have been a true highlight of the past six years. I feel fortunate to have shared this journey with each of them. Thank you all for your invaluable contributions and companionship. I am grateful to Monika Haselbauer for helping in all administration work.

Finally, I express my deepest gratitude to my family, Fatemeh, Keyghobad, Abouzar, Mitra and Siamak, who have been a constant source of support and encouragement throughout my academic journey. Their unwavering belief in me has been a driving force behind my accomplishments.

Above all, I want to extend an extra special acknowledgment to my wife-my love Golnaz. Her unwavering support, understanding, and sacrifices have played an indispensable role in my success. She has been providing endless encouragement and love during both the challenging and rewarding phases of my studies. Her belief in my dreams and Thank you, Golnaz, for being my partner, confidante, and the driving force behind my achievements

15. Publications

Annika Karger, **Siavash Mansouri**, Matthias S. Leisegang, Andreas Weigert, Stefan Günther, Carsten Kuenne, Ilka Wittig, Sven Zukunft, Stephan Klatt, Blerina Aliraj, Laura Klotz, Hauke Winter, Poornima Mahavadi, Ingrid Fleming, Clemens Ruppert, Biruta Witte, Ibrahim Alkoudmani, Stefan Gattenlöhner, Friedrich Grimminger, Werner Seeger, Soni Savai Pullamsetti, Rajkumar Savai. Long non-coding RNA ADPGK-AS1 regulates macrophage mitochondrial and phenotypic state – impact on lung cancer biology**.** *EMBO* 2023, DOI: 10.15252/embj.2022111620.

Dharmesh V. Hirani*, Florian Thielen*, **Siavash Mansouri**, Soula Danopoulos, Christina Vohlen, Pinar Haznedar-Karakaya, Jasmine Mohr, Rebecca Wilke, Jaco Selle, Ivana Mizikova, Margarete Odenthal, Cristina M. Alvira, Celien Kuiper-Makris, Gloria S. Pryhuber, Christian Pallasch, S. Koningsbruggen-Rietschel, Denise Al-Alam, Werner Seeger, Rajkumar Savai, Jörg Dötsch, Miguel A. Alejandre Alcazar. CXCL10 deficiency limits macrophage infiltration, preserves lung matrix, and enables lung growth in experimental bronchopulmonary dysplasia. *Inflammation and Regeneration* 2023, DOI: 10.1186/s41232-023-00301-6 .

Dharmesh Hirani, Cristina M Alvira, Soula Danopoulos, Carlos Milla, Michele Donato, Lu Tian, Jasmine Mohr, Katharina Dinger, Christina Vohlen, Jaco Selle, Silke v Koningsbruggen-Rietschel, Verena Barbarino, Christian Pallasch, Stefan Rose-John, Margarete Odenthal, Gloria S Pryhuber, **Siavash Mansouri**, Rajkumar Savai, Werner Seeger, Purvesh Khatri, Denise Al Alam, Jörg Dötsch, Miguel A Alejandre Alcazar. Macrophage-derived IL-6 trans-signalling as a novel target in the pathogenesis of bronchopulmonary dysplasia. *European Respiratory Journal* 2022, DOI: 10.1183/13993003.02248-2020.

Stefan Kuhnert, **Siavash Mansouri**, Michael A Rieger, Rajkumar Savai, Edibe Avci, Gabriela Díaz-Piña, Manju Padmasekar, Mario Looso, Stefan Hadzic, Till Acker, Stephan Klatt, Jochen Wilhelm, Ingrid Fleming, Natascha Sommer, Norbert Weissmann, Claus Vogelmeier, Robert Bals, Andreas Zeiher, Stefanie Dimmeler, Werner Seeger, Soni S Pullamsetti. Association of Clonal Hematopoiesis of Indeterminate Potential with Inflammatory Gene Expression in Patients with COPD. *Cells* 2022. DOI: 10.3390/cells11132121.

Siavash Mansouri, Rajkumar Savai. Tumor-Associated Macrophages: Biological Understanding and Therapeutic Opportunities. The Tumor Stroma (book chapter). *Jenny Stanford Publishing* 2022*.*

Siavash Mansouri, Daniel Heylmann, Thorsten Stiewe, Michael Kracht, Rajkumar Savai. Cancer genome and tumor microenvironment: Reciprocal crosstalk shapes lung cancer plasticity. *eLife* 2022, DOI: 10.7554/eLife.79895.

Xiang Zheng, Andreas Weigert, Simone Reu, Stefan Guenther, **Siavash Mansouri**, Birgit Bassaly, Stefan Gattenlöhner, Friedrich Grimminger, Soni Savai Pullamsetti, Werner Seeger, Hauke Winter, Rajkumar Savai. Spatial Density and Distribution of Tumor-Associated Macrophages Predict Survival in Non–Small Cell Lung Carcinoma. *Cancer Research* 2020, DOI: 10.1158/0008-5472.CAN-20-0069.

Xiang Zheng, **Siavash Mansouri**, Annika Krager, Friedrich Grimminger, Werner Seeger, Soni S Pullamsetti, Craig E Wheelock, Rajkumar Savai. (co-first author). Metabolism in tumour-associated macrophages: A quid pro quo with the tumour microenvironment. *European Respiratory Review* 2020, DOI: 10.1183/16000617.0134-2020.

Poonam Sarode, **Siavash Mansouri**, Annika Karger, Martina Barbara Schaefer, Friedrich Grimminger, Werner Seeger, Rajkumar Savai. Epithelial cell plasticity defines heterogeneity in lung cancer. *Cellular Signaling* 2020*, DOI:* 10.1016/j.cellsig.2019.109463.

Abdolhassan Talaiezadeh, Ali Shahriari, Mohammad Reza Tabandeh, Payam Fathizadeh, **Siavash Mansouri.** (Correspondence). Kinetic characterization of lactate dehydrogenase in normal and malignant human breast tissues. *Cancer cell international* 2015*, DOI:* 10.1186/s12935-015-0171-7